Assessment of aerodynamic characteristics of sub-scale aircraft model

A multi-fidelity approach

A.U.M. Baliga

Delft University of Technology

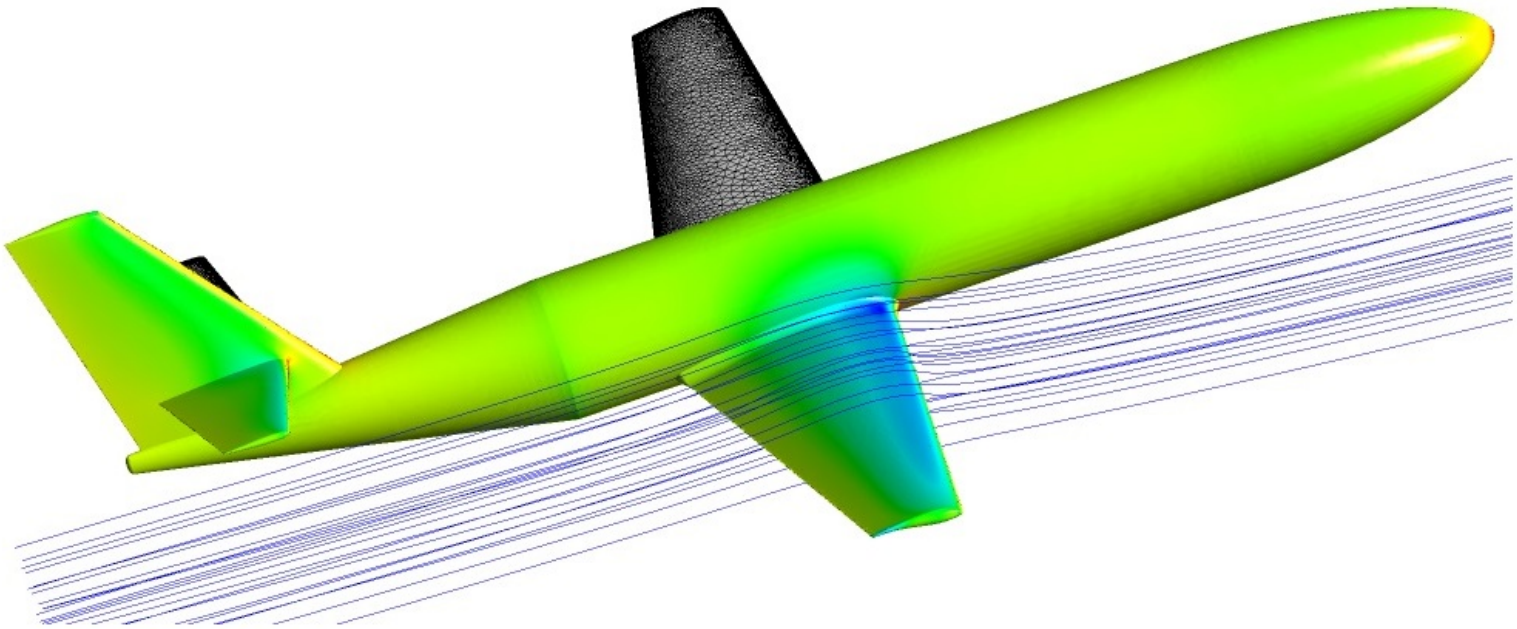

TU Delft Delft University of Technology

Challenge the future

ASSESSMENT OF AERODYNAMIC CHARACTERISTICS OF SUB-SCALE AIRCRAFT MODEL

A MULTI-FIDELITY APPROACH

by

A.U.M. Baliga

in partial fulfillment of the requirements for the degree of

Master of Science
in Aerospace Engineering

at the Delft University of Technology,
To be defended publicly on Friday 30 September, 2022 at 13:30.

Student number:	4726405
Track:	Flight Performance and Propulsion
Supervisor:	dr. ir. G. La Rocca
Daily Supervisor:	ir. A. Raju Kulkarni
Thesis Committee:	dr. ir. G. La Rocca
	dr. ir. T. Sinnige
	dr. ir. A. H. van Zuijlen

TU Delft Delft University of Technology

ABSTRACT

The demand for air travel keeps growing at an exponential rate and this leads the aviation industry to have even more of an adverse impact on the global climate and environment. The conventional tube and wing design of an aircraft, despite experiencing steady improvement in its fuel economy over the last few decades, can no longer keep up with this rise in demand. Novel aircraft designs like the Flying V, Prandtl Plane and the Blended Wing Body show promise towards supporting sustainable aviation.

To gain insight into the flight mechanics behaviour of both conventional and unconventional aircraft, Sub-scale Flight Test (SFT) is an effective method of testing during the preliminary stages of design. The recent advancement in technology related to miniaturization of electronics and manufacturing techniques, lead to building a more accessible SFT model. However, the effectiveness and the value of SFT is determined by the similitude between the SFT model and the corresponding full-scale aircraft. To maximize the similitude between the SFT model and the full-scale aircraft, the method of computational scaling is state-of-the-art for SFT model design. Since this approach uses iterative computer-based disciplinary analyses, it is time consuming and labor intensive. Given the limited time for SFT, the method of computational scaling for designing a SFT model is often infeasible. Among the various analyses, the aerodynamic analysis takes the most amount of time. Therefore, this thesis supports the computational scaling approach by speeding up the aerodynamic analyses necessary to predict the flight dynamics behaviour.

In the past, the 3D-Panel Method was used for the aerodynamic analyses for the design of SFT model. This surface-based method is computationally inexpensive, compared to other volume based Computational Fluid Dynamics (CFD) methods. The method does not consider the effects of viscosity and it also employs quasi-steady flow approximation for the analysis of dynamic behaviour. Although these engineering approximations reduce the computational load, it also brings in a number of errors. This method has poor drag predictions, fails to capture the effects of separation and shows insensitivity to changes in reduced frequency.

The limitations of the 3DPM can be overcome by using a CFD approach like Reynolds Averaged Naiver Stokes (RANS) method that can both capture the effects of viscosity, and use a fully unsteady approach in analyzing the dynamic behaviour. But this would be a very expensive computational approach, and therefore, it was previously deemed to be an infeasible method to generate the aerodynamic database. Thus, in this thesis, a multi-fidelity approach to generate the aerodynamic database for the SFT model design is developed. This multi-fidelity surrogate model uses the RANS method as the high-fidelity method and 3DPM as the low-fidelity method. A fusion-based Model Management Strategy is employed using co-kriging.

The multi-fidelity approach developed in this research, provides considerable value into generating the required aerodynamic database. Compared to using a single-fidelity RANS method, this multi-fidelity surrogate model will be capable of generating the required aerodynamic database for one-fifth the computational cost. This will help the computational scaling approach remain a feasible method for the design of SFT models. With the right SFT models, we will be able to gain insights into the flight behaviour of full-scale novel aircraft designs, thereby getting a step closer towards more sustainable aviation.

ACKNOWLEDGEMENT

The academic years at TU Delft have been a long journey, especially having to live through the Covid period. I would like to take this opportunity, to thank all the people who helped me along the way.

First and foremost, I thank my daily supervisor Akshay Raju Kulkarni for all his support and motivation provided during my Master thesis. I really appreciate all the valuable feedback I received. Being able to reach out easily, helped me get through my tough times. I am very grateful for the time provided for helping me out. I also thank my supervisor Gianfranco La Rocca for his support and feedback provided. His understanding of my situation and suggestion of ways to work, really helped me minimize my stress. I was very glad to have two very supportive supervisors.

I want to thank my mother Prathima Baliga and my father Udaya Baliga, who gave me all the love and support to complete my research work. I am also thankful for all my friends that motivated me and helped me push through, during very stressful times.

Adithya Baliga
September 2022

CONTENTS

NOMENCLATURE

α	=	Angle of attack [deg]
α_A	=	Amplitude of angle of attack [deg]
α_0	=	Mean angle of attack [deg]
ρ	=	Density of air $[kg/m^3]$
μ	=	Dynamic Viscosity of air $[Pa.s]$
θ	=	Pitch angle $[rad]$
ζ	=	Scaling factor for multi-fidelity method
c	=	Reference chord length $[m]$
C_L	=	Lift Coefficient
C_D	=	Drag Coefficient
C_m	=	Moment Coefficient
C_x	=	Force Coefficient in x direction
C_z	=	Force Coefficient in z direction
C_{z_α}	=	$\frac{\partial C_z}{\partial \alpha}$
C_{m_α}	=	$\frac{\partial C_m}{\partial \alpha}$
C_z	=	$\frac{\partial C_z}{\partial}$
C_m	=	$\frac{\partial C_m}{\partial}$
$C_{z_{\dot{\alpha}}}$	=	$\frac{\partial C_z}{\partial \dot{\alpha}}$
$C_{m_{\dot{\alpha}}}$	=	$\frac{\partial C_m}{\partial \dot{\alpha}}$
M	=	Mach number
k	=	Reduced frequency
q	=	Pitch rate $\frac{\partial \theta}{\partial t}$ $[rad/s]$
Re	=	Reynolds Number
S	=	Reference Area $[m^2]$
T	=	Time period of oscillation $[s]$
V_∞	=	Free stream velocity $[m/s]$
$3DPM$	=	3D Panel Method
CFD	=	Computational Fluid Dynamics
DNS	=	Direct Numeric Solution
KBE	=	Knowledge Based Engineering
LES	=	Large Eddy Simulation
MAE	=	Mean Absolute Error
$MDAO$	=	Multi-disciplinary Design Optimization
MMG	=	Multi Model Generator
$RANS$	=	Reynolds Averaged Navier Stokes
$RMSE$	=	Root Mean Square Error
SFT	=	Sub-scale Flight Test

UDF	=	User Defined Function
VGM	=	Variable Geometry Model
VLM	=	Vortex Lattice Method

1

INTRODUCTION

1.1. CHALLENGES IN THE AVIATION INDUSTRY

The civil aviation industry has been growing exponentially with annual number of passengers nearing from one billion in 1987 to two billion in 2005 and to over four billion in 2017[1]. As seen in figure 1.1, the industry is expected to see an annual traffic growth of 4% over the next 20 years[2]. This growth will also have adverse effects on the global climate and the environment. Civil aviation as a whole in 2019, was responsible for emission of around 915 million tonnes of CO_2, which accounts for global man-made emission of around 2.1% [3]. Global aviation is attributed with roughly 4% of the current anthropogenic climate change[4]. The noise around airports also negatively impacts health [5, 6].

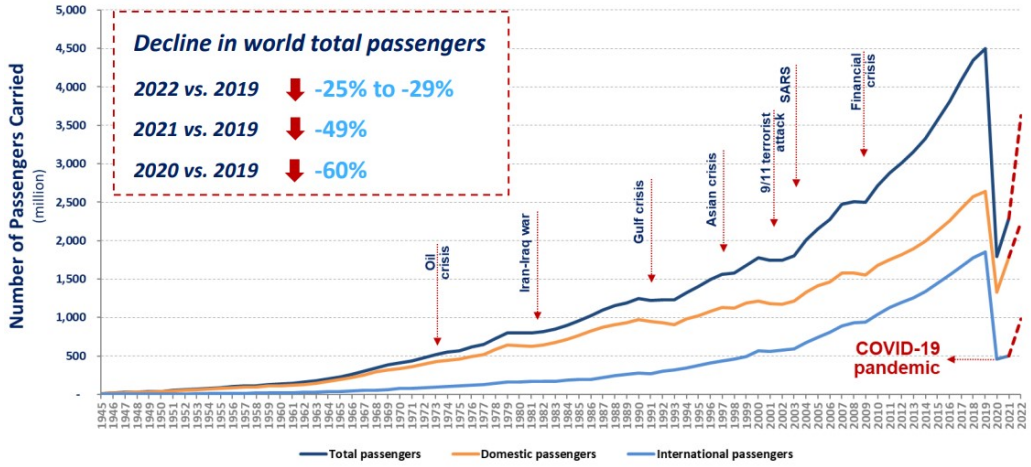

Figure 1.1: World passenger traffic evolution [1]

In order to mitigate the environmental and climate impact from the aviation industry, several strategies are followed. These can mainly be categorized into three - the changes brought about by technology, changes in operational methods and enforcing policies[7]. The technological changes relate to the improvement in engines and air frame that result in lower drag and better fuel efficiency. There is also a focus on developing alternative fuel that can reduce the impact on climate change[8]. Operational changes are those that are achieved by optimizing the air traffic of aircraft on ground and in the air. Such changes can lead from 8% to 18% reduction in fuel burn[9]. Policies or regulations are set in place for certification of aircraft and engines, that are enforced by global bodies like the International Civil Aviation Organization (ICAO). The adverse effect that the aviation industry has, can be kept in check by having stricter policies in place. One such change, is the Carbon Offsetting and Reduction Scheme for International Aviation(CORSIA) adopted by the ICAO, which has regulations in place, in order to achieve carbon neutrality by 2050[10].

If the aircraft and the engines have to be certifiable in the future, they need to keep up with the stringent regulations that are set in place, and technological changes will have a major role to play. The conventional

tube-and-wing design of the commercial aircraft has seen a lot of improvement in fuel efficiency over the last few decades. The Specific Fuel Consumption(SFC) of engines have improved by 40% from 1959 to 1995 while aerodynamic efficiency was improved by roughly 15%[11]. The major improvement in engines came with the introduction of high bypass engines. While the the steady growth in aerodynamic efficiency, can be attributed to the minor changes to the air frame, which is also a consequence of better materials that improve structural efficiencies[11]. Figure 1.2 shows a qualitative graph depicting the progress in commercial aircraft as compiled by Bravo-Mosquera *et al.*. The progress over the last four decades, is already approaching asymptotic behaviour and to keep up with the demands, there is a need for radical changes in technology.

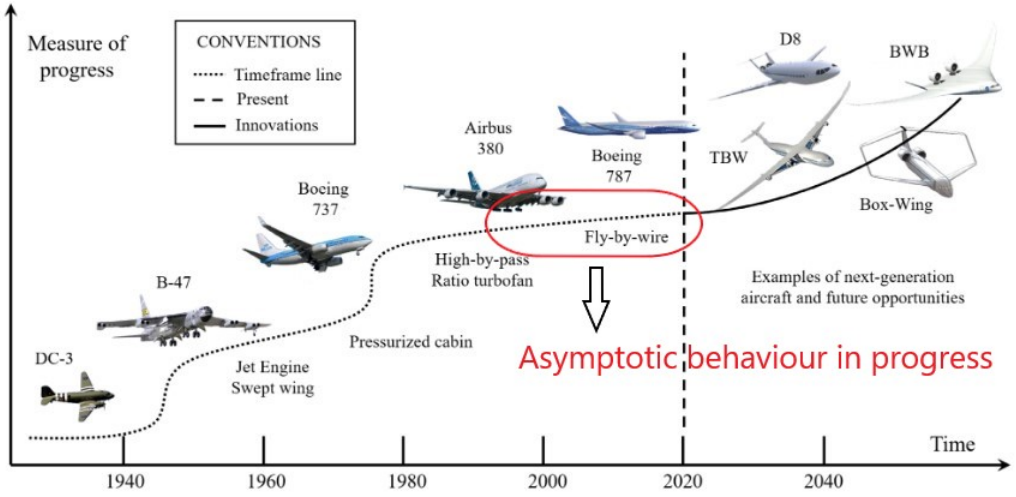

Figure 1.2: Compilation of progress in commercial aircraft [12]

Minor improvements to the conventional design will no longer be able to meet the economic, social and environmental needs of the future. Therefore, there is a need to explore unconventional configurations [7, 8, 11, 12]. Novel aircraft designs like the Flying-V , the Blended Wing Body Aircraft, Multi-Fuel Blended Wing Body and the Prandtl Plane (figure 1.3), show promise towards sustainable aviation[13].

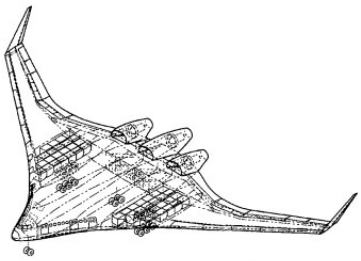

(a) Blended wing body[14]

(b) Prandtl plane[15]

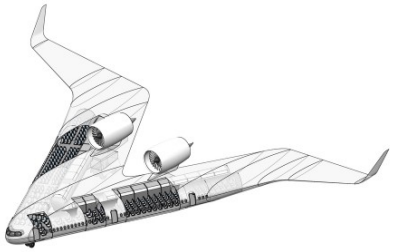

(c) Flying V [16]

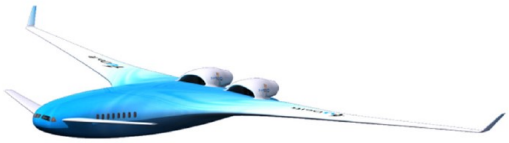

(d) Multi-Fuel Blended wing body[17]

Figure 1.3: Unconventional aircraft designs

1.2. ASSESSING THE FLIGHT BEHAVIOUR OF NOVEL AIRCRAFT DESIGNS

The novel aircraft designs need to meet the required safety standards, therefore, it is essential to know their flight behaviour under various conditions. Manufacturing a prototype for flight testing, is both economically unviable and risky during the initial stages of design [18]. Therefore, computer based simulation and physical experiments on sub-scaled models are performed during preliminary stages.

With the current level of advancement in computer technology, engineers today, rely heavily on computer simulation for analysing their design. This computational method involves iteratively solving the theoretical model, that describes a particular phenomenon. Since the methodology avoids creation of a physical model, it is usually the cheaper and sustainable alternative to physical tests[19]. The time required to perform a computational simulation depends on the computational complexity of the theoretical model that needs solving. An aircraft design involves designing with respect to multiple disciplines. These include the aerodynamics, propulsion, noise and emissions, weights, structure, flight controls and manufacturing [20]. Consequently, the behaviour of the aircraft is multi-disciplinary in nature. A theoretical model that captures the effects of multiple disciplines is computationally very complex. The computations can be so complex that the cost of the computational infrastructure required can even exceed those that of manufacturing a full-scale prototype. Even using the best of the computational facilities, the computational time required can far exceed the life-cycle of an aircraft [21]. Therefore, engineers often need to make simplifications and approximations in their computational approach which gives rise to errors called computational errors.

The experimental simulation often employs sub-scale models of prototypes to gain insights into the behaviour of the full-scale prototype[18]. Wind tunnel tests have been historically used to study the static behaviour. A complex experimental setup is required to study the dynamic behaviour using wind tunnel, which usually makes it a less preferable method. The effects of horizontal buoyancy, solid blockage, wake blockage and streamline curvature, that are often experienced in wind tunnels, lead to errors in the measured behaviour of the test specimen [22]. Sub-scale Flight Test(SFT), involves testing a sub-scaled model of the prototype with an onboard propulsion system. Building such a sub-scaled model has become more accessible with the recent advancement in technology, related to miniaturization of electronics and manufacturing techniques [23]. This method of testing is very effective to study both the static and dynamic flight behaviour of the sub-scaled model [24].

If the behaviour exhibited by the sub-scaled model is to be representative of that of the prototype, there needs to be similitude between the sub-scaled model and the full-scale prototype. This is a necessity in order to upscale the results. If we cannot establish similitude between the two, then the experimental approaches that employ sub-scaled models, provide no value towards learning the behaviour of the novel aircraft design. Two bodies in a flow are said to have Geometrical similarity if the ratio of geometrical dimensions are the same everywhere. When the quantities associated with motion are the same everywhere, this is referred as Kinematic similarity. Dynamic similarity is when the ratio of forces are same everywhere. For the flow to be called similar it is required that all the Geometric , Kinematic and Dynamic similarity are satisfied simultaneously [25]. In practice, controlling the physical variables in order to maintain the same set of similarity parameters is very difficult or impractical, and we end up not establishing perfect similitude between the prototype and its scaled model[24]. Therefore these tests always contain scaling errors.

In order for SFT to be effective and provide value into learning the flight behaviour of the novel aircraft, the SFT model requires careful designing, so as to ensure similitude. Historically, the classical similitude theory was used in the design of SFT models. But this is a very simplistic approach that often fails to establish similitude. The method of computational scaling is a state-of-the-art approach towards designing SFT models. It uses computational methods to maximise the similitude between the prototype and SFT model design [18]. In the early stages, we do not know the behaviour of the full-scale prototype and therefore, we have no means to validate the computational method used in the assessment of flight behaviour of the full-scale model. The methodology of computational scaling would use computational methods to also assess the flight behaviour of the sub-scale model. Although this is an additional step, the computational models that are utilized, can always be validated in the early stages. The computational approach into establishing similitude means it is a time-intensive process that often limits the use of this methodology into SFT model design. Therefore, a big challenge in design of SFT model is having a time efficient computational scaling method.

1.3. PREVIOUS RESEARCH INTO SFT MODEL DESIGN

Raju Kulkarni *et al.* introduces a novel approach towards SFT model design, using the state-of-the-art computational scaling approach [24]. The methodology employs the use of computational methods in a Multidis-

ciplinary Analysis and Optimization (MDAO) framework, to maximize the similarity between the sub-scale model design and the prototype of full-scale aircraft. A novel figure of merit called the Degree of Similitude (DoS) was introduced, to quantify the similarity between the sub-scale design and the full-scale aircraft.

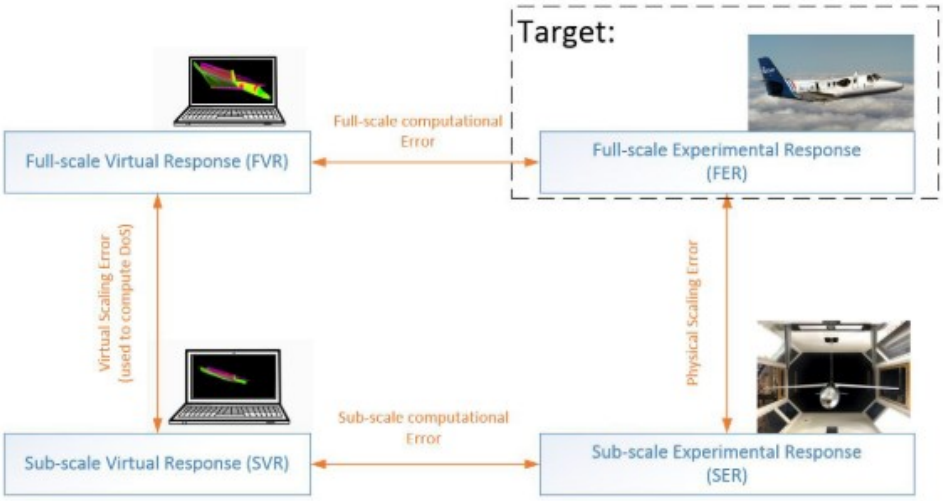

Figure 1.4: Method of testing and associated errors[24]

The figure 1.4 depicts the errors incurred with the various means of testing [24]. We are ideally interested in the behaviour of the prototype which in this case is regarded as the Full-scale Experimental Response (FER). Performing computational analyses on the computational model of the full-scale aircraft, results in the Full-scale Virtual Response (FVR). The computational errors that result in this process are termed as Full-scale computational error. Performing experimental simulation with a sub-scaled model of the prototype, results in the Sub-scale Experimental response(SER). The errors that arise due to insufficient similitude are called physical scaling errors. The computational scaling approach employs an additional step of performing computational analyses on computational model of the sub-scale model. The behaviour exhibited is termed as the Sub-Scale Virtual Response (SVR). The difference between the FVR and the SVR is called the Virtual Scaling Error. The DoS is defined as the weighted sum of normalized virtual scaling errors and mathematically represented as follows [24] :

$$DoS = 1 - \frac{1}{n}\sum_{i=1}^{n} w_i \times \frac{\left|C_{i_{FVR}} - C_{i_{SVR}}\right|}{\left|C_{i_{FVR}}\right|} \quad ; \quad \sum_{i=1}^{n} w_i = 1 \tag{1.1}$$

where, n is the number of selected aerodynamic coefficients, $C_{i_{FVR}}$ is the i^{th} relevant aerodynamic coefficient obtained by computational analysis of the full-scale model, $C_{i_{SVR}}$ is the i^{th} relevant aerodynamic coefficient obtained by computational analysis of the sub-scale model and w is the degree of influence of given aerodynamic coefficient [24].

The similitude is maximized by maximization of DoS. This maximization process is iterative and does not come cheap. The aerodynamic analyses that are required in order to quantify DOS, are also iterative processes. In order to analyze the large range of motions, the design space that needs exploration, is also large. If the computational time of the aerodynamic analyses is large, then this methodology would be rendered infeasible.

The input test parameters for obtaining the aerodynamic database for the aircraft of given SFT design are - angle of attack, side slip angle, Mach number, roll rate, pitch rate, yaw rate and control surface deflection. Considering the lower end, for a clean configuration we would have to consider 3 angles of attack, 3 side slip angles , 2 Mach numbers, 2 roll rates, 2 pitch rates and 2 yaw rates which would result in 144 cases. And the control surface deflected configuration needs to be simulated for at least 3 angles of attack, 3 side slip angles , 2 Mach numbers and 2 control surface deflections which is a total of 36 cases per control surface. Practically, when we take more than the bare minimum number of arguments for each variable, the number of evaluations to be made are over 1000 as can be seen in the work of [26].

Since there are a large number of cases to solve in order to obtain the database, there is a need for a method that can make fast evaluations. The 3DPM was found out to be the optimal method for this application[27]. In the field of Computational Fluid Dynamics (CFD), this is a fairly low-fidelity method. Using this method for the aerodynamic analyses, the computational time required for the generation of aerodynamic database is roughly around 50 hours [26]. For similar set of evaluations, if higher fidelity method like RANS were to be used, it would roughly take 250 days of computational time with similar computational power.

1.4. RESEARCH OBJECTIVE AND RESEARCH QUESTION

The 3DPM that was used in the previous research was able to generate the aerodynamic database at affordable cost. This ensured the process of computational scaling approach to still be a feasible method into designing SFT model. The reduced computational cost also results in reduced accuracy of the computational method. The 3DPM method ignores the effects of viscosity which leads to poor prediction of drag characteristics and an inability to predict effects of stall. Furthermore, the dynamic derivatives of the aerodynamic coefficients, which are essential into learning the dynamic behaviour, are obtained by means of a quasi-steady approach. The quasi-steady approach into the study of fully unsteady phenomenon results in the method showing an insensitivity towards the changes in reduced frequency, associated with a given dynamic motion. Due to lack of experimental data for dynamic behaviour, the uncertainties associated with the corresponding evaluations made by the 3DPM remain unknown.

Higher fidelity CFD method like RANS has the potential to cover the drawbacks of the 3DPM. The method models the effects of viscosity and turbulence to a decent degree, and is known to give reasonable predictions of viscous drag and effects of separation [21]. This method allows for simulating a fully unsteady flow, in order to capture the dynamic behaviour of the aircraft. Due to the large computational costs associated with this method, the previous research had to settle for the use of 3DPM, for generating the aerodynamic database as required in the SFT model design.

This research will focus on developing a multi-fidelity approach, towards generating the aerodynamic database, for SFT model designs. This will be achieved by using the previously used 3DPM as the low-fidelity method and the RANS methods as the high-fidelity method. A fusion-based model management strategy is employed. The fusion will be brought about by co-kriging and the resulting surrogate model will be referred to as the multi-fidelity, kriging-based surrogate model. The main research question would be,
'What is the impact of utilizing a multi-fidelity approach in the generation of aerodynamic database as compared to the classical single-fidelity methods?'

This could be broken down into the following sub questions:

- What are the costs associated with using the high-fidelity method and can they be minimized?
- How accurate is the low-fidelity method relative to high-fidelity method?
- What are the cost and accuracy of the multi-fidelity surrogate model?
- Does the multi-fidelity surrogate model actually show any value compared to using a surrogate-based high-fidelity approach?

The answers to the above questions would help us assess the overall impact of the proposed methodology and if it is a viable approach in the aerodynamic assessment of SFT model design.

1.5. SCOPE OF THESIS

For any research, it is important to highlight the scope, bounds and the assumptions that are made. This research would mainly focus on improving the aerodynamic analysis part of the methodology laid out by Raju Kulkarni *et al.* for the assessment of sub-scale designs. Due to time restraints the following bounds are set:

- Upon going through the various fidelity levels for aerodynamic analysis, this research will only investigate one method that would seem like the best fit.
- The previous aerodynamic analysis process was already automated and therefore this research will only compare the time it takes to solve the relevant governing equations while assessing the feasibility.

- Only longitudinal direction will be taken into consideration for generating the database.
- Since the research only pertains to sub-scale designs where the Mach number of the flow is low, the simulation will be carried out for a fixed Mach number.
- This research mainly focuses on capturing the dynamic behaviour, the control surface deflected configuration will not be considered.
- The previously used 3DPM could only simulate for pitch in a quasi-steady approach and is incapable of simulating plunge. Therfore only pitching motion is considered for assessment of dynamic behaviour.
- Therefore, the simulation will be carried out for a range of angles of attack and pitch rate. The figure 1.5 shows the inputs and outputs that would be considered in this research.

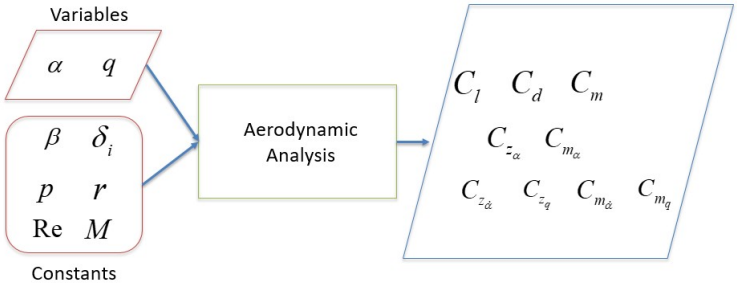

Figure 1.5: Inputs and Outputs

1.6. OUTLINE OF THESIS

The chapter 2 will provide a background into multi-fidelity methods, CFD and computation of dynamic derivatives. It will also discuss the methodology adopted in this research. Chapter 3 will contain the verification and validation of the methods that were followed in this research. The results of the grid dependence studies conducted during this research are discussed in chapter 4. The first research sub-question will be answered here. The main findings of this research, which is the impact of using a multi-fidelity approach are discussed in the chapter 5. The answers to the remaining sub-questions will be found in this chapter. This thesis will end with the chapter 6, which will consist of the conclusion and recommendation for future research.

2

BACKGROUND AND METHODOLOGY

The method of computational scaling for design of SFT models requires a comprehensive aerodynamic database. This database needs to be generated in a reasonable time frame. Otherwise the whole design process becomes infeasible. The 3DPM was previously used to perform the required aerodynamic analysis and generate the database. It was an optimal choice, since methods like RANS are computationally very expensive [27]. The figure 2.1 shows the accuracy and errors related to various methods. We need a method of generating the aerodynamic database, that would be almost as accurate as RANS, while not being being computationally as expensive. Therefore, a multi-fidelity surrogate model using the two methods is developed in this research.

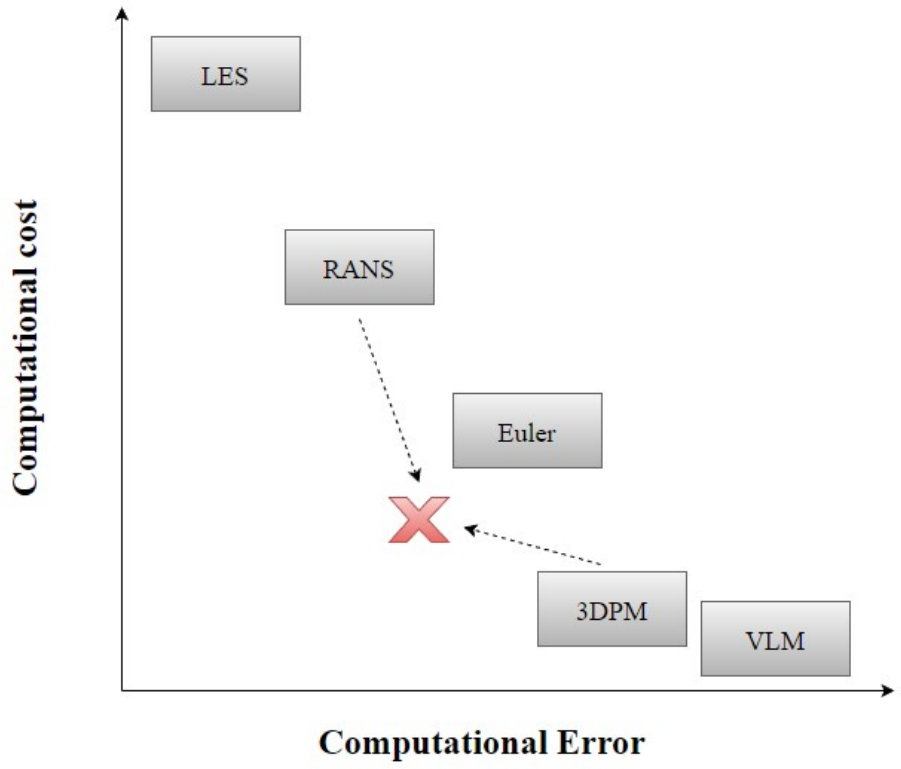

Figure 2.1: Accuracy and error of various CFD methods

The section 2.1 provides a background into multi-fidelity methods. The multi-fidelity methodology adopted in this research, is discussed in section 2.2. A background to the CFD methods shown in figure 2.1, is given in section 2.3. The section 2.4 discusses the methodology of obtaining the dynamic stability derivatives that

make up the aerodynamic database. Finally the section 2.5, summarizes the multi-fidelity approach proposed in this research and discusses the computational setup used.

2.1. MULTI-FIDELITY METHODS

Computational methods involve solving a set of mathematical equations that govern a physical phenomenon. This set is referred to as the mathematical model. Therefore the terms method and model mean the same in this context. Fidelity of a computational method or computational model refers to how accurate the method is into simulating the reality. Multi-fidelity models or multi-fidelity surrogate models are methods that employ two or more computational methods of varying levels of fidelity to generate the data of interest[28]. According to Peherstorfer *et al.*, the two key requirements for creating a multi-fidelity model are low-fidelity model for a given computational model, and a model management strategy. The subsection 2.1.1 will discuss the methods of obtaining low-fidelity models and the following subsection 2.1.2 will discuss the model management strategies that are often employed. The figure 2.2 shows an overview of creating a multi-fidelity surrogate model.

2.1.1. LOW-FIDELITY MODEL

Simplified models are those derived from the the high-fidelity models by exploiting the domain expertise and knowledge of implementation that form the high-fidelity method. In the field of CFD, the Large Eddy Simulation(LES), RANS, Euler methods, Potential flow methods are derived from the Direct Numeric Simulation(DNS) by making certain engineering assumptions, and they consequently lead to models that can be evaluated faster compared to solving the full set of underlying equations. This is an example of using the domain expertise. More details about these will be discussed in section 2.3. Solving the set of equations requires discretization, and discretizing the domain into coarser grid would result in lesser computation time as compared to that of solving on finer grid. This is how the knowledge of implementation can be exploited in order to create a low-fidelity method by simplifying the high-fidelity[28].

Projection-based models are the surrogate models obtained by exploiting the mathematical structure of the problem. Projecting the governing equations onto a low-dimensional subspace that is constructed to retain the characteristics of the system input-output map, yield the surrogate model. Examples include Proper Orthogonal Decomposition, Reduced basis method, Krylov sub spaces , Dynamic mode decomposition etc. [28]

Data fit models are low-fidelity models that are created by curve fitting the given inputs and outputs from the high-fidelity model. These are constructed by fitting the coefficients of the linear combination of the basis function by interpolation or regression to inputs and the corresponding outputs. Examples include the method of least squares, Lagrange polynomials, Piece-wise polynomial interpolation, Radial Basis Method, Kriging etc.

2.1.2. MODEL MANAGEMENT STRATEGY

Adaptation is a model management strategy wherein the the data from the low-fidelity model is continuously enhanced by data from high-fidelity method. In Efficient Global Optimization, a kriging model is adapted in each iteration of the optimization process and high-fidelity evaluations are invoked when the variance predicted by the kriging model is large [29]. Another example is the use of additive or multiplicative updates to the low-fidelity model, based on the difference or ratio of the sampled set of low-fidelity and high-fidelity evaluations. The correction models are usually based on Taylor series expansion or Gaussian process models like kriging [30].

Fusion is model management strategy that deals with evaluation of low-fidelity and high-fidelity outputs and then combining the data from all outputs. Examples for these include the control variate framework and co-kriging [28].

In **Filtering**, the high-fidelity model is invoked when the low-fidelity model is considered to be inaccurate based on a low-fidelity filter or the candidate point meets certain criteria as output from low-fidelity evaluation. Example for these include importance sampling, Multistage Markov chain Monte Carlo algorithm and multi-fidelity stochastic collocation [28].

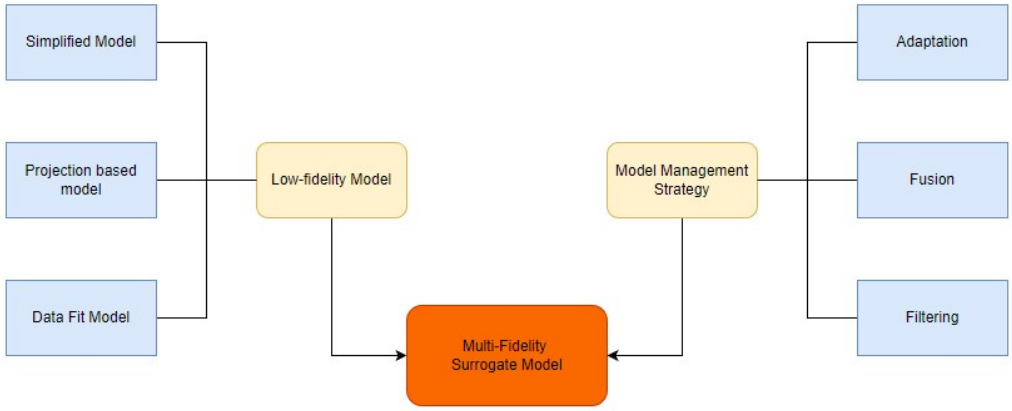

Figure 2.2: Schematic representation of Multi-fidelity Surrogate modelling

2.2. MULTI-FIDELITY SURROGATE MODEL FOR AERODYNAMIC ANALYSIS

This research developed a multi-fidelity surrogate model using RANS as the high-fidelity method and 3DPM as the low-fidelity method. For the model management strategy, co-kriging is a highly suitable choice. The method already shows the benefits of employing such a model management strategy for fusing the Euler and RANS data for static simulation of a 2D airfoil [31, 32].

Kriging is an unbiased data fit model that takes into consideration the closeness, spatial continuity and the redundancy of the available data while predicting the value at an unknown location. The unknown value the random function Z at location X_0, can be constructed as a linear combination of the known values at X_i [33]. This is represented by the equation 2.1.

$$Z(X_0) = \sum_{i=1}^{n} \lambda_i Z(X_i) \tag{2.1}$$

The weights λ are found such that the variance of the prediction is minimized. This leads to solving the following set of equations represented by 2.2. The method followed in this research is called **ordinary kriging**. Here the mean is assumed to be stationary but unknown. The unknown mean is evaluated directly by solving the set of equations with this added constraint. A detailed breakdown of each of the intermediate steps involved in this method can be found in appendix A.

$$\sum_{i=1}^{n} \lambda_j Cov(Z(X_i), Z(X_j)) = Cov(Z(X_j), Z(X_0)) \quad where \quad j = 1, 2....n \tag{2.2}$$

The covariance between two points are obtained as the product of the correlation function ψ and the variance $sigma$ for random variable function. This is shown in equation 2.3.

$$Cov(Z(X_i), Z(X_j)) = \sigma^2 \psi(X_i, X_j) \tag{2.3}$$

Multi-fidelity kriging or co-kriging, predicts the high-fidelity values of the function $Z_h(X)$ as a scaled value of a low-fidelity function $Z_l(X)$ and a discrepancy function $Z_d(X)$ which is a Gaussian random function[34]. This is shown in equation 2.4 where ζ is the scaling factor.

$$Z_h(X) = \zeta Z_l(X) + Z_d(X) \tag{2.4}$$

The covariance matrix evaluation in the case of ordinary kriging only involved a single random function. This time there are three matrices that correlate the two fidelity levels involved. The set of extra covariance matrix definitions are shown in equation 2.5. The subscript 'l' and 'h' refer to the quantities associated with the low-fidelity function and high-fidelity function respectively.

$$
\begin{aligned}
Cov(Z_l(X), Z_l(X)) &= \sigma_l^2 \psi_l(X_l, X_l) \\
Cov(Z_h(X), Z_l(X)) &= \rho \sigma_l^2 \psi_l(X_l, X_h) \\
Cov(Z_h(X), Z_h(X)) &= \rho^2 \sigma_l^2 \psi_l(X_l, X_l) + \sigma_d^2 \psi_d(X_d, X_d)
\end{aligned} \tag{2.5}
$$

By solving the modified matrices, one can obtain the multi-fidelity kriging prediction. This research will use the 3DPM as the low-fidelity model while using RANS to obtain the high-fidelity samples. The scaling factor ζ will be assumed to be a constant. When $\zeta = 0$, the multi-fidelity kriging reduces to ordinary kriging. The multi-fidelity surrogate model is not able to leverage any information from the low-fidelity model. In order to assess if the low-fidelity method is truly impacting the multi-fidelity model, the results of ordinary kriging will be used as a secondary reference. This would serve as a control group for the study. **Mean Absolute Error** and **Root Mean Square Error** will be used as error metrics in this research. The mathematical definitions are shown in equation 2.6 and 2.7 respectively.

$$
MAE = \frac{1}{N} \left| \sum_{i=1}^{n} \left(Z^{ref}(X_i) - Z(X_i) \right) \right| \tag{2.6}
$$

$$
RMSE = \sqrt{\frac{\sum_{i=1}^{n} \left(Z^{ref}(X_i) - Z(X_i) \right)^2}{N}} \tag{2.7}
$$

The figure 2.3 shows the schematic diagram of the multi-fidelity analysis developed in this research. A background to CFD methods used for in this approach, will be provided in the next section.

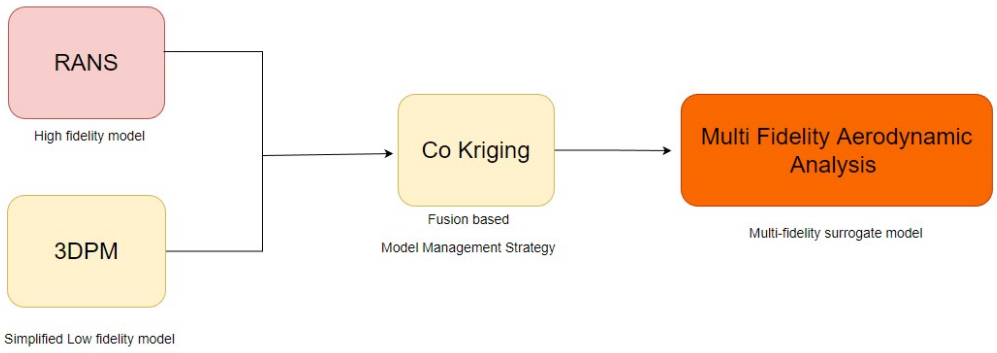

Figure 2.3: Multi-fidelity Aerodynamic Analysis

2.3. COMPUTATIONAL FLUID DYNAMICS

Computational Fluid Dynamics (CFD) as the name suggests is the technique of computationally analysing the fluid flow around/in a body by solving a set of governing equations. There are three main processes to CFD:

- Pre-Process- This is where the geometry of the body is generated and discretized/meshed , the fluid domain, boundary conditions and fluid properties are defined and appropriate governing equations and solver settings are chosen.
- Solving - This is where the system of equations are iteratively solved until the required convergence conditions are satisfied.
- Post-Process - The solution thus obtained are analysed and graphical representation are created.

The fundamental governing equations for the fluid flow, used in CFD analysis are given below [25]:

Using the laws for conservation of mass the following differential equation is obtained as the following is called the continuity equation.

$$\frac{\partial \rho}{\partial t} + \vec{\nabla}.(\rho \vec{v}) = 0 \tag{2.8}$$

where ρ is fluid density and $\vec{v}$ is the velocity vector

Applying the laws of conservation of linear momentum we arrive at the momentum conservation equation more commonly known as the Navier-Stokes Equation.

$$\frac{\partial \vec{v}}{\partial t} + (\vec{v}.\vec{\nabla})\rho \vec{v} = \vec{g} - \frac{\vec{\nabla} p}{\rho} + \frac{\mu \nabla^2 \vec{v}}{\rho} \tag{2.9}$$

where $\vec{g}$ is acceleration due to body forces, p is fluid pressure and μ is the kinematic viscosity.

Ignoring the body forces, the Navier-Stokes Equation is often represented in its multi-index form as[35],

$$\frac{\partial u_i}{\partial t} + \frac{\partial u_i u_j}{\partial x_j} = -\frac{1}{\rho}\frac{\partial p}{\partial x_i} + \frac{\partial}{\partial x_j}\left(\frac{\mu}{\rho}\frac{\partial u_i}{\partial x_j}\right) \tag{2.10}$$

Utilizing the laws of thermodynamic energy balance we can derive the following energy equation.

$$\rho \frac{D\vec{v}}{Dt} + \vec{\nabla}.(\rho \vec{v}\,\vec{v}) = -p\vec{\nabla}\vec{v} + \vec{\nabla}(k\vec{\nabla} T) + \Phi + S \tag{2.11}$$

where k is coefficient of conductivity, T is Temperature, Φ is viscous dissipation term and S is the source term.

The chaotic changes in fluid pressure and velocity which are characteristics of turbulence is a widely observed phenomenon in everyday life and is crucial for analyzing fluid flows. There is still no theory that explains turbulence, however, the effects can be calculated by solving the full set of governing equations prescribed by equations 2.8, 2.9 and 2.11. This method is called the **Direct Numeric Simulation (DNS)**.

To resolve all the turbulent scales in space and time, the number of discretized grid points required is proportional to the cube of Reynolds number. For aerospace applications Reynolds number is around the order of 10^6 which gives the requirement of about 10^{18} grid points. Solving for this entire set is computationally extremely expensive and almost impossible even with today's computational resources. It is impractical for most every-day engineering simulations[21].

Even though DNS can potentially give the exact solution and is of highest fidelity in CFD, it is not suited for engineering applications. Resolving the smallest of the turbulent structures by solving the set of governing equations is what brings in the complexity in DNS and makes it impractical. Since most energy and momentum are carried by the larger turbulent structures/large eddies, the flow can be spatially filtered to separate the small and large scale turbulent structures. The flow is solved for the large eddies while a model is used to resolve the smaller eddies. This is method of solving is called the **Large Eddy Simulation (LES)** and is practically of the highest fidelity employed in engineering CFD applications[25].

Although LES is capable of capturing the turbulence effects very well, it is still computationally very expensive to employ. In **Reynolds Averaged Navier-Stokes (RANS)** method, the Navier-Stokes equation 2.10 is rewritten by statistically averaging the instantaneous components involved and upon solving these set of equations we obtain averaged solution over the whole domain where the turbulence is modelled everywhere; from the smallest to the largest of the scales[21].

We can split an instantaneous component u_i into its mean $\langle u_i \rangle$ and a fluctuation part $u_i{}'$ as follows

$$u_i = \langle u_i \rangle + u_i{}' \qquad where \quad \langle u_i \rangle = \frac{1}{N}\sum_{l=1}^{N} u_i|_l \tag{2.12}$$

Applying the averaging function we rewrite the equation in 2.9 as

$$\frac{\partial \langle u_i \rangle}{\partial t} + \frac{\partial \langle u_i \rangle \langle u_j \rangle}{\partial x_j} = -\frac{1}{\rho}\frac{\partial \langle p \rangle}{\partial x_i} + \frac{\partial}{\partial x_j}\left(\frac{\mu}{\rho}\frac{\partial \langle u_i \rangle}{\partial x_j}\right) - \frac{\partial R_{ij}}{\partial x_j} \tag{2.13}$$

$R_{ij} = \rho \left\langle u_i{}' u_j{}' \right\rangle$ is the Reynolds Stress Tensor and it needs to be modelled by a set of transport equations. Depending on the number of of equations involved in the set of transport equations, the RANS turbulence models in increasing fidelity levels are[36]:

- Prandtl, zero equation model
- Spalart-Allmaras (SA), one equation model
- Standard k-ϵ, two equation model
- Standard k-ω, two equation model
- Shear Stress Transport (SST) k-ω, two equation model
- Reynolds Stress Model, seven equation model

There is no one model that is suitable for all flows and often each model is developed to best capture the turbulence effects for a given flow. In the field of aviation, the SA and the SST RANS models are widely used because they are relatively less expensive methods for capturing the averaged turbulence effects[36]. The SA model is cheaper compared to SST and will be used in this research for the aerodynamic analysis.

In the field of aviation which deals with high Reynolds and Mach number, the contribution from the viscous terms are negligible as long as the flow is not separated [21]. The Euler equations are the inviscid flow equations which can be formulated as the limiting case of Navier-Stokes equation where the viscosity tends to zero. The equation in 2.9 therefore becomes[25]:

$$\frac{\partial \vec{v}}{\partial t} + (\vec{v}.\vec{\nabla})\rho\vec{v} = \vec{g} - \frac{\vec{\nabla} p}{\rho} \tag{2.14}$$

This is the **Euler method**. Solving this set of equations is computationally cheaper than RANS and provides fairly accurate results when the main focus is to find the lift distribution resulting from the pressure and velocity distribution. They still account for compressibility and non-linear effects in the governing equation. This method is the cheapest among methods that utilize volume mesh.

By neglecting the body forces and taking the curl of the Navier-Stokes equation in 2.9, the equation takes the following form

$$\rho\frac{\partial \vec{\zeta}}{\partial t} + \rho(\vec{v}.\vec{\nabla})\vec{\zeta} + \rho\vec{\zeta}.\vec{\nabla}\vec{v} = \mu\nabla^2\vec{\zeta} \tag{2.15}$$

where the $\vec{\zeta} = (\vec{\nabla} \times \vec{v})$ is the vorticity.

If we assume an irrotational flow, then the vorticity $\vec{\zeta} = 0$ and for a scalar function ϕ the following identity holds true.

$$\vec{\nabla} \times (\vec{\nabla}\phi) = 0 \qquad where \quad \vec{v} = \vec{\nabla}\phi \tag{2.16}$$

The scalar function ϕ is called the velocity potential function and we can obtain the velocity field as the gradient of this function and this method is called the **potential flow method**[25]. Often a source or a sink term is used with finite vorticity strength and the solution is obtained by integrating and superimposing the solutions that arise from uniform flow and vortices. The 3DPM and Vortex Lattice Method (VLM) are potential flow based methods.

In **3DPM**, the flow around the airfoil is modelled as the summation of uniform series of vortex panels on the body which forms a closed polygon that approximates the shape of the body. Each panel has a linearly varying vortex strength such that the strength of end of a panel is same as the strength of the next panel. Using this basis the Laplacian shown in equation 2.16 is solved in order to obtain the pressure and velocity distribution. This provides a time effective way to compute lift [25]. Unlike the previous methods, this method only requires a surface mesh for analysis.

VLM utilizes the Lanchester–Prandtl lifting line theory or the Lanchester–Prandtl wing theory to model the aerodynamic lift characteristics. The lifting line theory is a mathematical model which predicts the aerodynamic properties for a wing of finite span. It simulates a finite wing by a number of horseshoe vortices distributed across the span which constitute to the lifting line. The trailing vortices formed induces a downwash which modifies the local angle of attack at that section[37]. Using such a method the Laplacian shown in equation 2.16 is solved to compute the pressure and velocity distribution. This method is faster than the vortex panel method since it does not consider the actual thickness of the body and only considers the lifting surfaces for solving but it also results in loss of accuracy.

Utilizing the methods discussed in this section, one can obtain the pressure/velocity distribution around the body in the flow. The forces and moments on the body can be computed from this distribution. The method of computing the dynamic stability derivatives will be discussed in the next section.

2.4. DYNAMIC STABILITY DERIVATIVES OF AN AIRCRAFT

The evaluation of dynamic stability derivatives are important in the assessment of stability, control and handling characteristics of an aircraft[38]. These dynamic derivatives in this research will be obtained from the classical forced oscillation method. This research restricts the dynamic motion of the aircraft in the longitudinal direction only. The dynamic motion of the aircraft in the longitudinal direction concerns the pitch and the heave motion of the aircraft. The forces and moments experienced by an aircraft are a function of angle of attack and the freestream velocity. The dynamic motion results in a change of these quantities, which change the forces and moments experienced by the aircraft. The equation 2.17 shows the Taylor series expansion for the normal force coefficient of the aircraft.

$$C_z = C_{z_0} + C_{z_\alpha}\alpha + C_{z_{\dot\alpha}}\dot\alpha\frac{c}{2V_\infty} + C_{z_q}q\frac{c}{2V_\infty} + C_{z_{\dot q}}\dot q\left(\frac{c}{2V_\infty}\right)^2 \tag{2.17}$$

When the aircraft purely pitches/rotates about a reference point, the angle of attack is also changed by the same amount. In the case of plunging motion (also called heaving motion), the vertical velocity that the aircraft experiences results in change of angle of attack. These are illustrated in figures 2.4 and 2.5 respectively. A combination of pitching and plunging is called a flapping motion[39]. In this case, the effective change in angle of attack is the superimposition of the two.

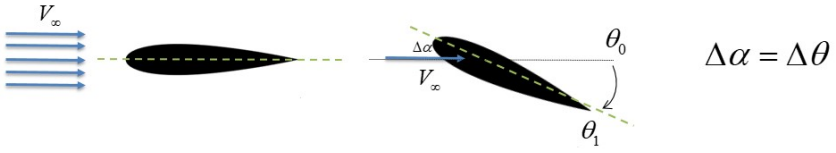

Figure 2.4: Change in angle of attack with change in pitch

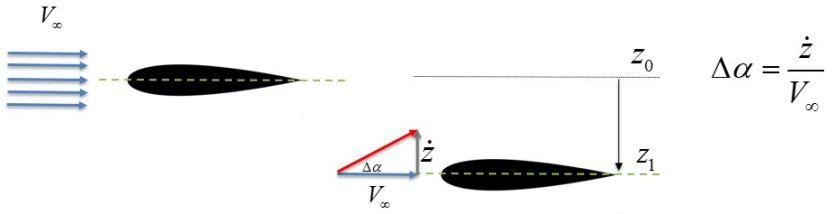

Figure 2.5: Change in angle of attack with change in vertical position

In the forced oscillation method, the aircraft is given a sinusoidal excitation of the following equation

$$\alpha = \alpha_0 + \alpha_A.\sin\omega t \tag{2.18}$$

The equation 2.17 now takes the form of

$$\Delta C_z = \alpha_A(C_{z_\alpha} - k^2 C_{z_{\dot q}})\sin(\omega t) + \alpha_A k(C_{z_{\dot\alpha}} + C_{z_q})\cos(\omega t) \tag{2.19}$$

where $k = \frac{\omega c}{2V_\infty}$ is the reduced frequency and $\Delta C_z = C_z - C_{z_0}$

The LHS of equation 2.19 is obtained by CFD methods that can simulate unsteady flow. In this research, it is RANS. The unknown derivatives on the right can then be obtained by performing inverse Fourier transforms[40]. If we ignore the effects of the higher derivative $\dot q$, then we have the following equations

$$C_{z_\alpha} = \frac{2}{\alpha_A nT}\int_0^{nT}\Delta C_z(t)\sin(\omega t)\,dt \tag{2.20}$$

$$C_{z_{\dot{\alpha}}} + C_{z_q} = \frac{2}{k\alpha_A nT} \int_0^{nT} \Delta C_z(t) \cos(\omega t) dt \tag{2.21}$$

where n is the number of cycles and T is the time period. Similar equations hold true for the moment coefficient.

$C_{z_{\dot{\alpha}}} + C_{z_q}$ is called the combined dynamic derivative. When the aircraft is in pure-pitching motion, (see figure 2.6) the combined derivative contains both the contribution from $\dot{\alpha}$ and q. While the input motion is a pure plunging motion, (see figure 2.7) the combined derivative only contains the contribution of $\dot{\alpha}$. A pure flapping motion (see figure 2.8) is where the change in angle of attack caused by pitching is negated by that caused by plunging. In such a case, the combined dynamic derivative contains only the contribution by q. Therefore, in order to separate each contribution, one has to simulate any two of the above three input motions[38]. The derivatives obtained on respective simulation are shown schematically in figure 3.2. Since the quasi-steady method from 3DPM does not have the means to separate the individual components, and always gives the combined derivatives, this research will only simulate the pitch motion in order to obtain the combined derivatives in the longitudinal direction. The aerodynamic database will also contain the lateral and directional dynamic derivatives. The same approach can be followed using RANS to compute those derivatives. The figure 2.9 shows a schematic diagram of the motion and the associated derivatives across all directions.

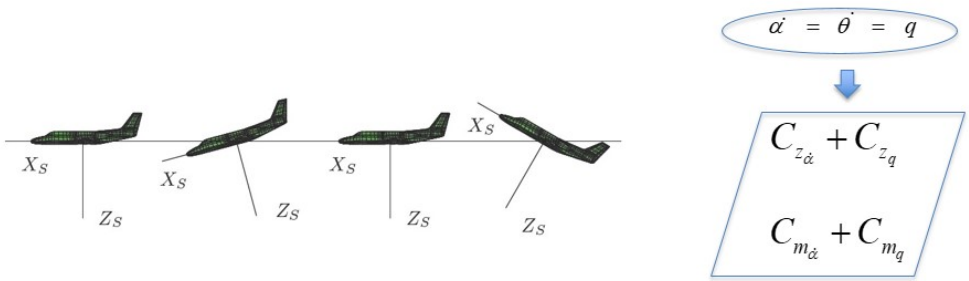

Figure 2.6: Harmonic pitching motion of the aircraft [39]

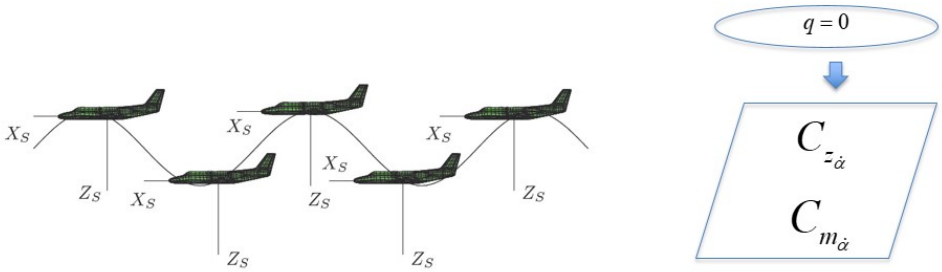

Figure 2.7: Harmonic plunging motion of the aircraft[39]

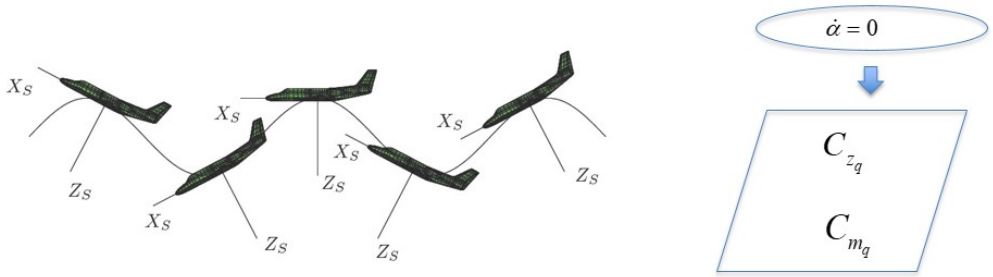

Figure 2.8: Harmonic flapping motion of the aircraft [39]

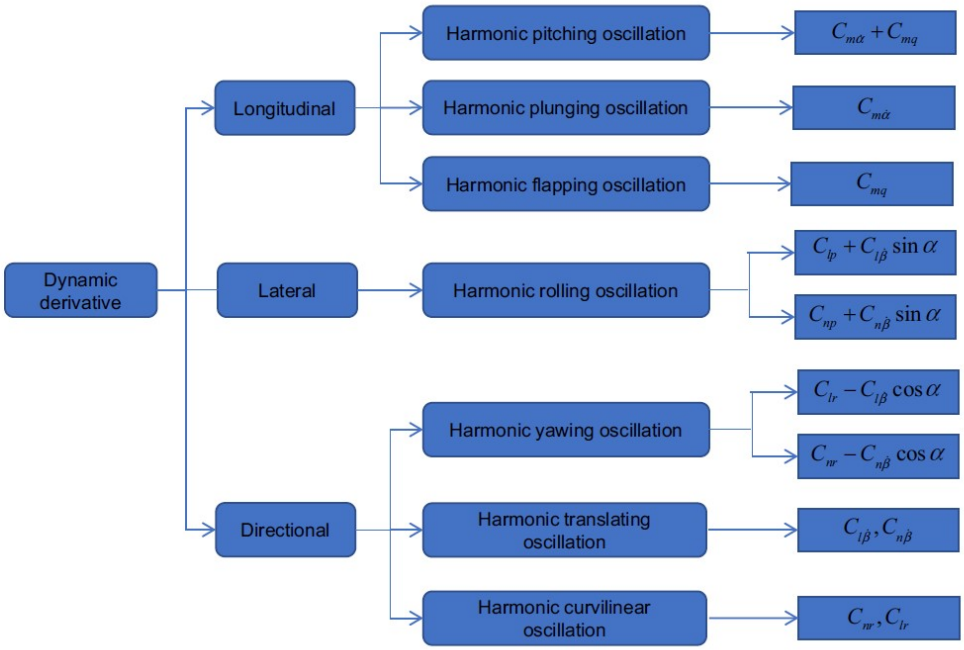

Figure 2.9: Dynamic derivatives across all directions [38]

The 3DPM which uses the quasi-steady method, cannot be used to compute the dynamic derivative using forced oscillation method. The quasi-steady method essentially solves the same steady-state equations with a modified velocity field [27]. The velocity field is modified to include a radial component of the velocity based on the pitching frequency as seen in figure 2.10. The dynamic derivatives are obtained from the difference between the coefficients of the quasi-steady and the steady method and is given by equation 2.22. The drawback with this method is that it is insensitive to changes in reduced frequency. Furthermore, there were no experimental results to quantify the errors in the dynamic stability derivatives that were computed. The dynamic derivatives computed from RANS in this research, will serve as a reference to quantify the errors relative to a method of higher fidelity.

$$C_{z_q} + C_{z_{\dot{\alpha}}} = \frac{C_z^{QS} - C_z^S}{k} \tag{2.22}$$

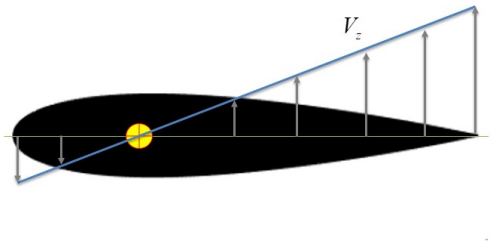

Figure 2.10: Modification of the flow-field for quasi-steady simulation

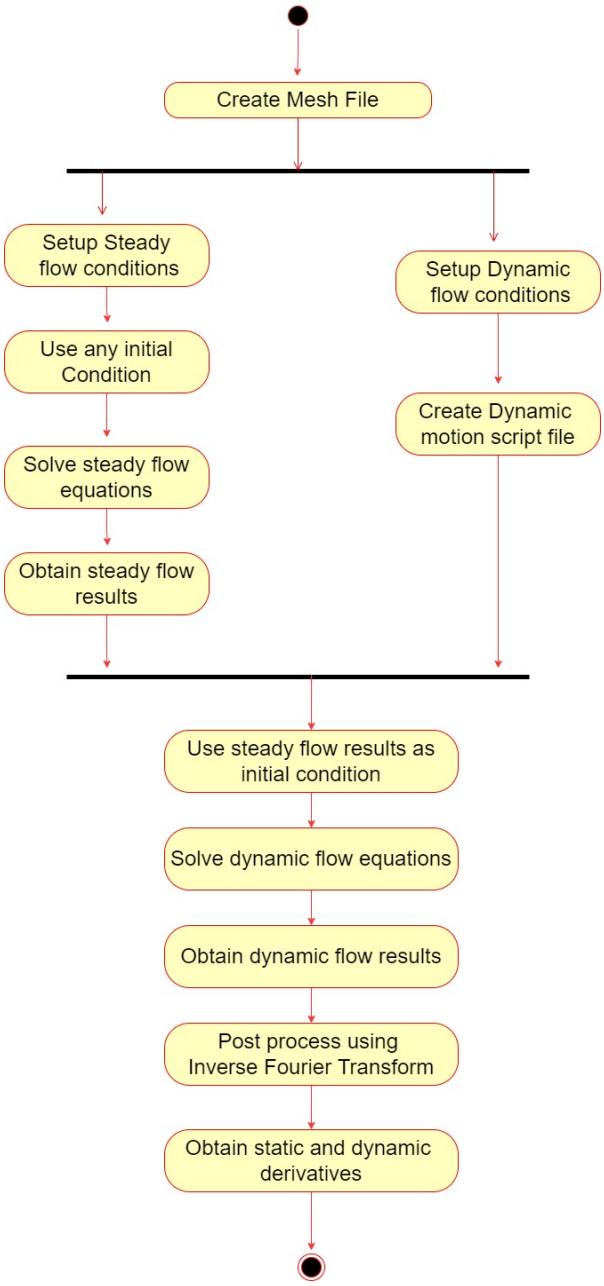

Figure 2.11: Activity diagram for forced oscillation method

In order to obtain the dynamic derivatives with the method of forced oscillation, we first need to perform a steady-state analysis at given angle of attack. The pre-process requires the availability of a volume mesh and setting up of the required boundary conditions. Since this is a steady-state analysis, the solution can be initialized by using the inlet boundary condition or hybrid initialization[41]. The solution of the steady-state analysis will be used as initial condition for the dynamic analysis. The C_{z_0} required in 2.19, is the steady-state normal force coefficient at given angle of attack. The C_z is the dynamic normal force coefficient obtained from the unsteady simulation. This is the output response of the aircraft for the forced harmonic excitation. The harmonic motion is implemented by means of mesh motion. The static and dynamic derivatives can be obtained by performing inverse Fourier Transforms as given by equation 2.20 and 2.21. The activity diagram for obtaining the static and dynamic derivatives using the forced oscillation method, is shown in figure 2.11

2.5. METHODOLOGY AND COMPUTATIONAL SETUP

This section summarizes the multi-fidelity approach into generating the aerodynamic database, and discusses the computational setup used in this research. Furthermore, a brief background into the motivation for the upcoming chapters is discussed here. Figure 2.12 shows the generic activity diagram to obtain multi-fidelity aerodynamic database using co-kriging.

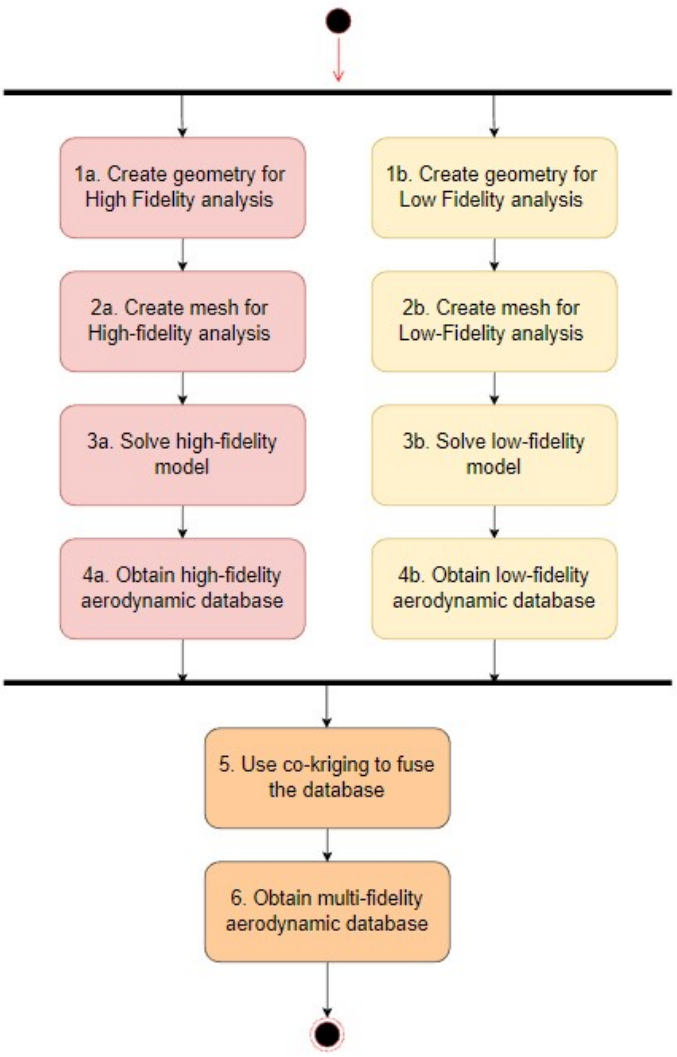

Figure 2.12: Activity diagram for obtaining multi-fidelity database

In this research, the aerodynamic analysis of Variable Geometry Model(VGM) is performed. VGM is a 8.8% geometrically scaled model of the Cessna Citation II 550[26]. The motion is restricted to the longitudinal direction. The multi-fidelity aerodynamic database is generated using RANS as the high-fidelity method and 3DPM as the low-fidelity method. Generating the geometry and creating a mesh is part of the pre-processing. In step **1a**, the geometry of the aircraft is created using SpaceClaim, a software owned by ANSYS. The mesh is then generated using ANSYS meshing in step **2a**. Guidelines from the work of Gottee *et al.* are followed while creating the mesh for RANS. The geometry (**1b**) and mesh (**2b**.) as required for the 3DPM is generated by the Multi Model Generator(MMG) which is an in-house tool developed at TU Delft. This is a Knowledge-Based Engineering (KBE) application that supports aircraft MDAO [43]. The pre-processing is usually intensive because of the manual labor that is involved. The MMG automates this process for the 3DPM. Therfore, the time required for pre-processing of the two methods will not be compared.

ANSYS Fluent is the commercial CFD solver used to solve the RANS model in step **3a**. The user manual and the tutorial manual of this software, provide guidelines for optimal solver settings and solution strategies [36, 41]. The recommended settings and solver strategies are used, and they will be highlighted in chapter 3. The step **3b** utilizes the commercial software Flightstream, for solving the 3DPM. Obtaining the dynamic derivatives through forced oscillation method using RANS requires the implementation of mesh motion. The harmonic pitching motion of a body is not a part of the standard package provided by Ansys. User Defined Function (UDF) needs to be used to generate the required motion[44]. This script is compiled using Microsoft Visual studio and loaded within the software before solving the case. The dynamic derivatives are obtained by post-processing the solution obtained in step **3a**. This is done using a script that runs on the commercial software MATLAB. The process of obtaining the dynamic derivative required creating the necessary script files. Therefore, the process will be verified in section 3.2 of chapter 3. Flightstream readily outputs all the required data for the generation of the low-fidelity aerodynamic database (**4b**). The high-fidelity aerodynamic database (**4a**) would be a sparse set of data containing results at sample locations.

In step **5**, the sparse high-fidelity database and the dense low-fidelity database will be fused using co-kriging. This forms the multi-fidelity surrogate model developed in this research. Using this, we obtain the multi-fidelity aerodynamic database (**6**). Once again, this code was developed in-house. Therefore, this multi-fidelity surrogate model is first validated in section 3.3 of chapter 3. Note that the steps 1b, 2b and 3b were not performed during the thesis. The low-fidelity aerodynamic database (4b) was readily available and obtained from the author Raju Kulkarni *et al.*.

The specifications of the computer used in this research are shown in table 2.1. The comparison of computational time is only restricted to the solving part of the CFD and will not include the pre-processing time. Furthermore, the time corresponds to computational wall time which is the real time it takes for solving a given computational model, with all the cores working in parallel. The process can be sped up by using more cores in parallel, thereby reducing the computational wall time. From the work of Epanchintsev *et al.*, it can be seen (figure 2.13), that the gains start to decrease after a certain point. In a parallel process, a task needs to be distributed between the cores and information exchange has to take place. The tasks may not be always equally distributed. This results in some of the cores remaining idle until all other complete their share of tasks. When these offsets overtake the gains of parallel processing, we see a reduction in speed up [45]. This research did not study the impact of the number of cores on the computational wall time. During the research, a single node on the High Performance Computing (HPC) cluster at TU Delft was reserved, and all 20 cores of that node were used for computation.

Product	Intel Xeon Processor
Processor Number	E5-2660v3
Number of cores	20
Base Frequency	2.6GHz
Total RAM	128 GB
Cache	25MB

Table 2.1: Specifications of the computer used in the analysis

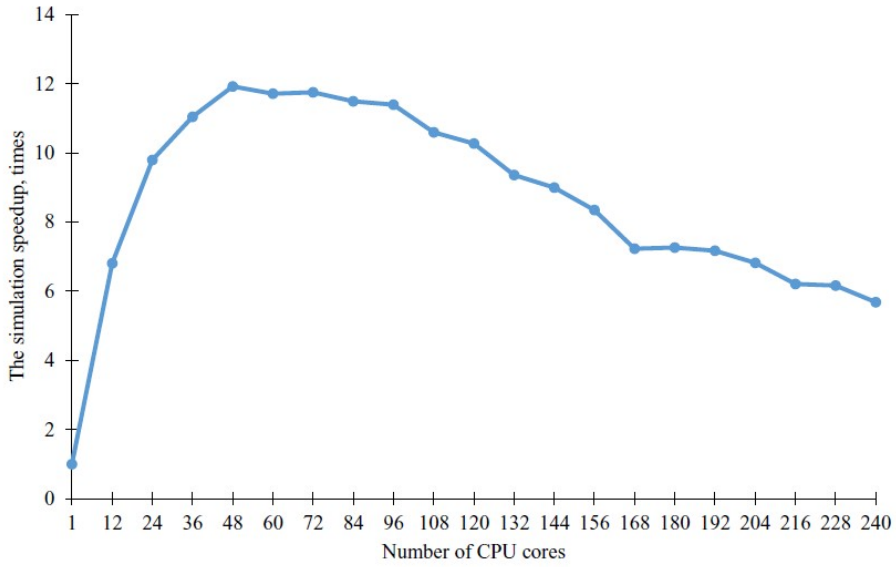

Figure 2.13: Speedup in computational time with increasing number of CPU cores [45]

3

VERIFICATION AND VALIDATION

The verification and validation of the computational methods used in this research are discussed in this chapter. The section 3.1 begins with validating the RANS method by comparing the static results to that obtained from wind tunnel experiment. The process of obtaining the dynamic derivative using the forced oscillation method is verified in section 3.2. This study did not make use of commercial tools for multi-fidelity surrogate model. Instead an in-house application was developed. This will be validated in section 3.3.

3.1. VALIDATION OF VGM

In this section, the static results obtained from steady state RANS for the VGM are validated using the wind tunnel results from the previous work of Raju Kulkarni *et al.*. Furthermore, the results from 3DPM data are also used to highlight the accuracy between the 3DPM and RANS. The wind tunnel tests on the VGM was carried out in the Low Turbulence Tunnel(LTT) at the Delft University of Technology. This is a low-speed, closed return wind tunnel with test-section dimensions of $1.8m \times 1.25m$. The turbulence measured in the wind tunnel was less than 0.1% [24]. The figure 3.2 highlights the key dimensions of the VGM. The setup of the physical model of the VGM in the LTT is shown in figure 3.1.

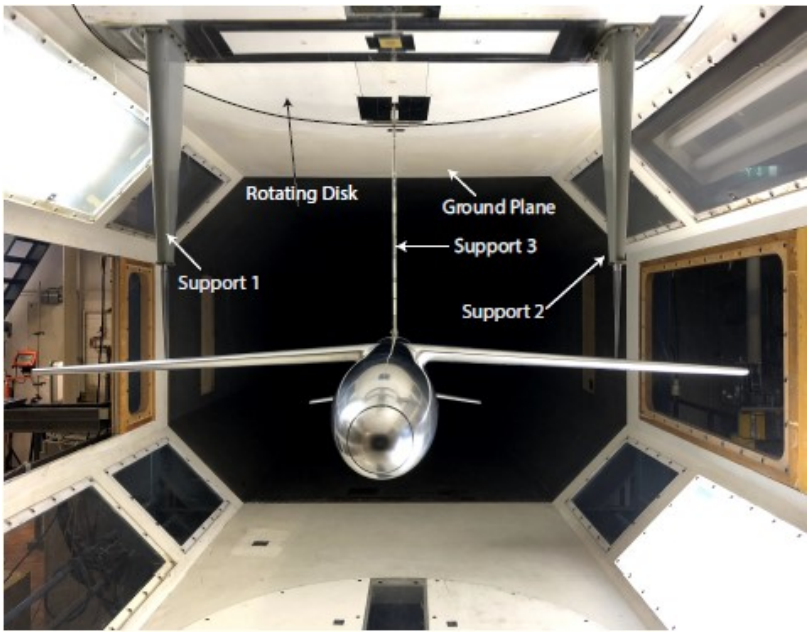

Figure 3.1: Wind tunnel setup of VGM [24]

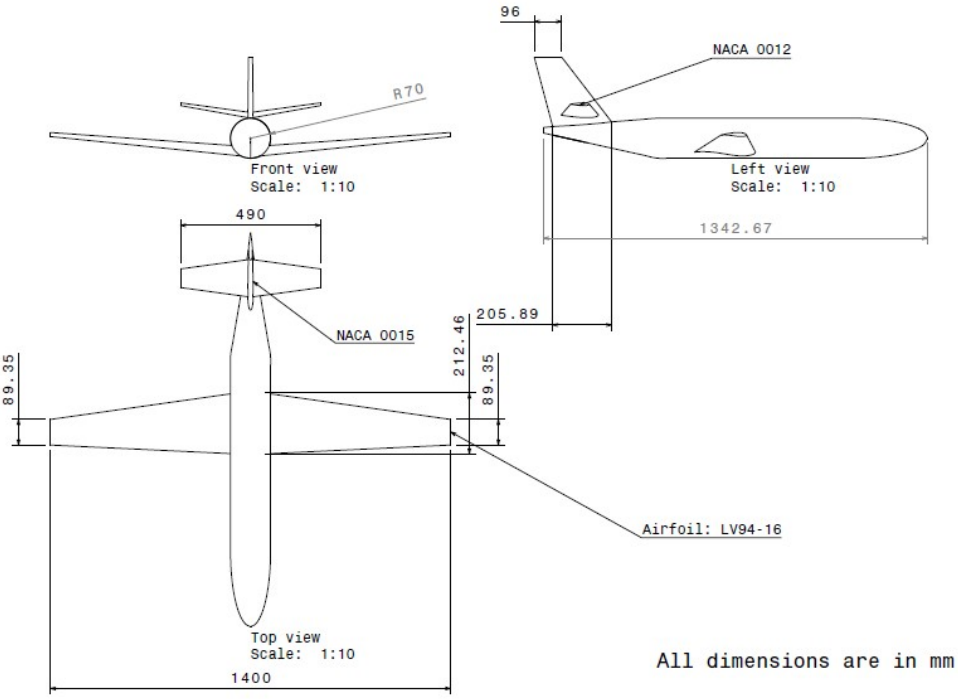

Figure 3.2: Dimensions of VGM

The RANS method was used to simulate the static behaviour for a Reynolds number of 500,000 and a Mach number of 0.13. The nose of the aircraft is at the origin and a rectangular domain of $45m \times 30m \times 30m$ is used. Relative to the origin, the domain extends 30m in the downstream direction and 15m in every other direction. Furthermore, in order to have better resolution of the wake in the proximity of the aircraft, a body of influence in the shape of an elliptical cylinder is used. This has a semi-minor axis of 0.5m, semi-major axis of 3m and a width of 2m. The domain and the zoomed in image of the body of influence are highlighted in the figure 3.3.

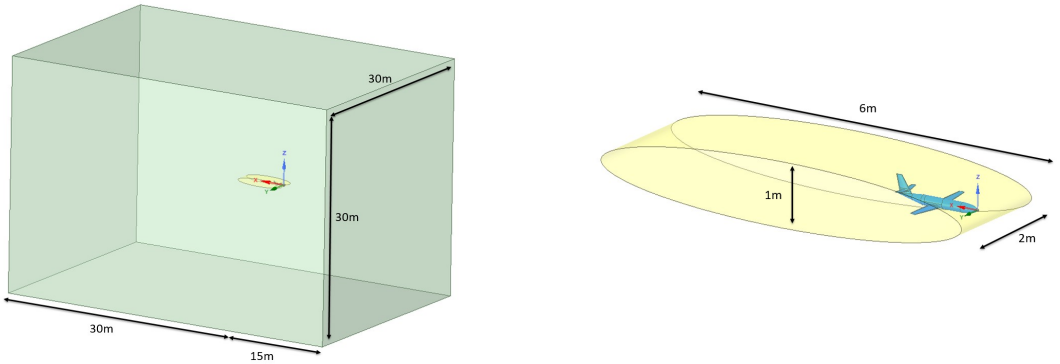

(a) Domain

(b) Body of influence

Figure 3.3: Geometry used for the simulation of VGM

A tetrahedral unstructured mesh with 19.6 million cells and 6.1 million nodes is used in the simulation of both the static and the dynamic simulation of the VGM throughout this research. In order to resolve the boundary layer, 20 prism layers are used with the initial cell height of $8 \times 10^{-6} m$ and a growth ratio of 1.175.The maximum element size within the body of influence region is restricted to $5 \times 10^{-2} m$. The mesh was constructed using the commercial software ANSYS Mesher following the best practices in this field of study, that

can be found in [42]. The figure 3.4 shows the resulting surface mesh that is used throughout this study. The decision to use this mesh was based on a study where the influence of different types of mesh was investigated. The results of this study will be discussed in the upcoming chapter along with other sensitivity studies that were carried out.

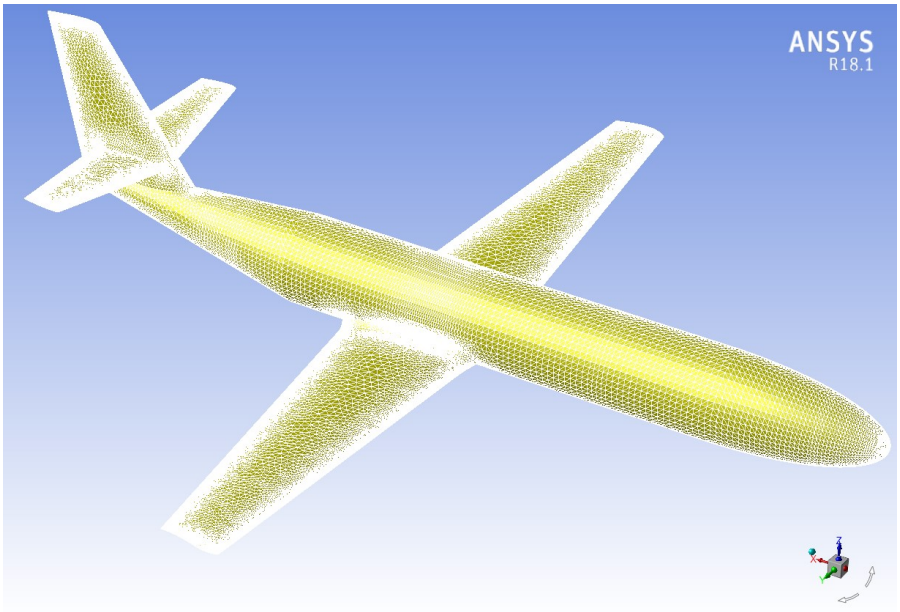

Figure 3.4: Surface mesh of the VGM

The static simulation is carried out for angles of attack from -5 to +14 degrees in steps of 1 degree. A pressure-based solver is used with the steady formulation. The SA-Turbulence model is used with Sutherland formulation for the viscosity model. Pressure outlet boundary condition is used on the face downstream of the flow while velocity inlet conditions are used for the remaining five faces in the domain. The choice of the various solver setting that will be discussed here are based on following the tutorial manual provided by Ansys. [41]. Turbulent viscosity ratio of 10 is used for the boundaries which is a default value provided by the software. Coupled scheme is used for the pressure-velocity coupling and Green-Gauss Node based scheme is utilized for the gradient discretization. The solution is initialized using hybrid initialized scheme based on the inlet and outlet boundary conditions.

A lower order scheme for interpolation offers more stability while solving but lacks accuracy when compared to the higher order schemes. Under relaxation factors are used for faster convergence. Higher value leads to slower convergence. Therefore the solution is obtained by performing first few iterations of lower order scheme with lower relaxation factor, followed by higher under relaxation factors at higher orders of interpolation schemes. This ensures that the intended solution quickly moves towards an approximate value with increased solver stability, and once the solver is stable enough it can move towards the solution as predicted by that of higher order schemes. The order of the schemes and under relaxation factors that are used for in this simulation are highlighted in table 3.1 and 3.2 respectively. The Ansys user Guide provides us with the optimal strategies for solving different CFD problems [36].

Interpolation Scheme	First 50 iterations	Following 250 iterations
Pressure	First Order	Second Order
Density	First Order	Third Order MUSCL
Momentum	First Order	Third Order MUSCL
Modified Turbulent Viscosity	First Order	Third Order MUSCL
Energy	First Order	Third Order MUSCL

Table 3.1: Order of interpolation schemes used in the steady state simulation

Under relaxation factor	First 50 iterations	Following 250 iterations
Momentum	0.3	0.5
Pressure	0.3	0.5
Density	1	1
Body Forces	1	1
Modified Turbulent Viscosity	0.8	0.95
Turbulent Viscosity	0.8	0.95
Energy	1	1

Table 3.2: Under relaxation factors used in the steady state simulation

Temperature	288K
Pressure	1 atm
Density	1.225 kg/m^3
Velocity	44.23 m/s
Reference Chord	0.165 m
Reference area	0.2179 m^2
Viscosity	1.78 x 10^{-5} kg/ms

Table 3.3: VGM flow parameters

The mean aerodynamic chord or the reference chord length is 0.165m and the reference surface area is 0.2179m^2. The reference point for moment center used in this validation case is (0.680m,0m,-0.0565m). This corresponds to the quarter-chord location of the central section of the main wing of this aircraft. The flow parameters corresponding to the Mach number and Reynolds number are listed in the table 3.3. The simulations were carried out for a total of 300 iterations which roughly cost a computational wall time of 2 hours per angle of attack. Residual reduction of 7 orders were achieved for the corresponding iterations. The 3DPM incurs a computational time of 4 minutes for a given angle of attack.

In figure 3.5, the lift coefficient curves for the wind tunnel results are compared with that of the RANS and 3DPM. The Wind Tunnel curve shows a linear behaviour at low angles of attack from -5 to +8 degrees and from 9 degree AoA, a drop in lift is seen. This is due to the flow over the wing starting to seperate at high angles of attack. The 3DPM that is based on potential flow is not able to capture this separation and over predicts the lift at higher angles of attack. The lift computed from the RANS results show a better match at low angles of attack and it is still able to capture the non-linear behavior at higher AoA.

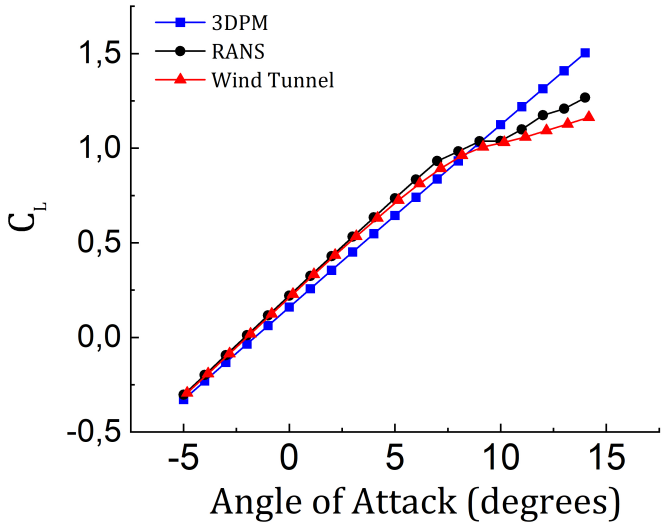

Figure 3.5: Lift coefficient vs Angle of Attack

At the range from 10 to 14 degree AoA, the 3DPM incurs a MAE of 30% and a RMSE of 21% when compared to that of wind tunnel. The RANS method on the other hand has a MAE of 9% and a RMSE of 6%. This shows that although the RANS method used in this research is not as reliable at high AoA , it is still able to give an indication for the onset of stall. The effects of stall can be studied using RANS by refining the mesh in the region of wake. Further, the oscillations in the wake make it more of an unsteady behaviour which would need transient formulation for better resolution. Since all of this would lead to a study in itself and goes beyond the scope of the research which is to be able to generate aerodynamic database during in the conceptual design phase, the value obtained at the end of the 300th iteration is used as the result while comparing.

Figure 3.6 shows the drag polars obtained for the VGM in Wind tunnel , 3DPM and RANS. At low angles of attack from -5 to +5 degrees , it can be seen that the RANS predictions are roughly off by 60 drag counts compared to that of the wind tunnel. However this does not necessarily mean that RANS has a poor prediction. The drag measured in the wind tunnel is in fact atypically large despite the blockage corrections that were applied. Referring to the setup shown in figure 2.5 we can see that the body is almost as wide as the test section and could lead to slight over-prediction of drag because of interference effects from the walls of the wind tunnel. At high angles of attack, the drag from the body is large enough that the interference effects are made negligible and the predictions from RANS are roughly off by 2 drag counts.

The 3DPM compared to that of the wind tunnel incurs a MAE of 350 drag counts and a RMSE of 200 drag counts. This is the consequence of being unable to capture the viscous effects. In a study that assess scaled designs that are often attributed with lower Reynolds number, the effects of viscous forces does play a significant part in the overall drag of the design. Therefore a large drawback of using 3DPM for the predictions of drag is seen. It must be noted that these results were obtained from the 2017 version of Flightstream. These results are purely obtained from solving the potential flow field discussed in chapter 2, and do not contain any viscous correction effects.

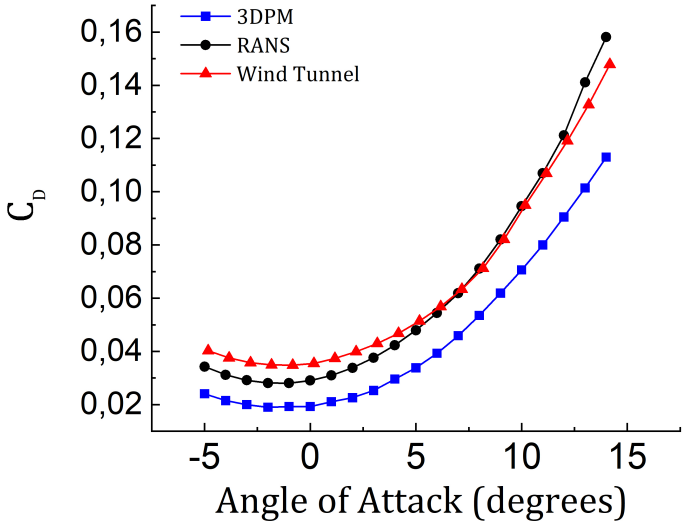

Figure 3.6: Drag coefficient vs Angle of Attack

Figure 3.7 shows the pitching moment curves for VGM from the Wind tunnel tests, 3DPM and RANS that are computed at the reference point of (0.680m,0m,-0.0565m). The moment curves show a similar behaviour to that of the lift curves wherein RANS is better at capturing the non-linear behaviour that occurs after the onset of flow separation at high AoA, compared to 3DPM. The 3DPM is not sensitive to such changes and continues a downward linear trend. The difference in absolute values of the moment curve between RANS and wind tunnel would be the consequence of the reference point that the moments are measured around. In a simulation, one can always measure desired result at any given location and the errors arise from the interpolation of the data based on the presence of computational cells. While conducting an experiment with physical models, errors also arise from the placement of the measuring instruments. The discrepancy between the reference considered and the point of actual measurement can lead to such a difference between the moment curves.

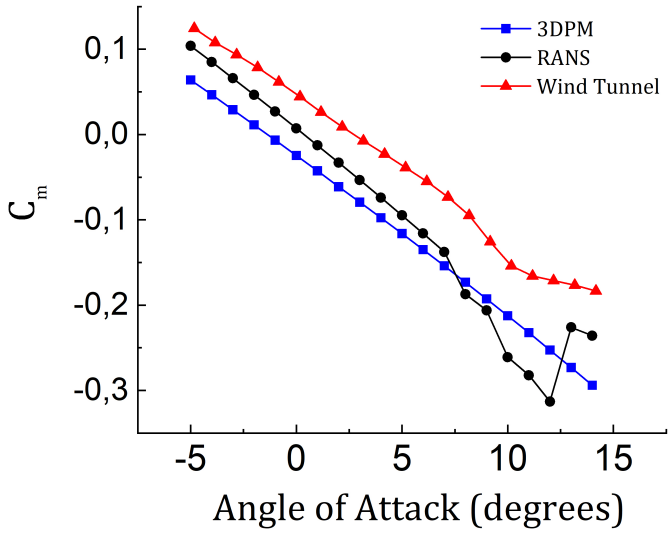

Figure 3.7: Moment coefficient vs Angle of Attack

3.2. VERIFICATION FOR COMPUTING THE DYNAMIC DERIVATIVES

There exists no data for the validation of the dynamic results for VGM which was a major gap in the previous research. In this section, the method that is used in obtaining dynamic derivatives is verified by simulating the harmonic pitch of NACA0012 airfoil which can be found in the work of Ronch *et al.*. The NACA0012 airfoil is simulated at Mach number of 0.755, with mean AoA of 0.016 degree , with an amplitude of 2.51 degrees and reduced frequency of 0.0814. These are the wind tunnel test conditions that can be found in the AGARD report of Landon. Ronch *et al.* used this case for validation. Therefore, this is an indirect validation.

The airfoil used has a chord length of 1m and both the location of the moment centre and pivot point correspond to the quarter-chord location. The simulation uses a 2D stuctured CH mesh comprising of 34,951 quadrilateral cells. Figure 3.8 highlights this mesh that is employed for the dynamic simulation. The simulation employs Euler method with a pressure-based solver while the reference literature makes use of a density-based solver. A total of 3 cycles were simulated with each cycle consisting of 128 time steps and 30 inner iterations per time step.

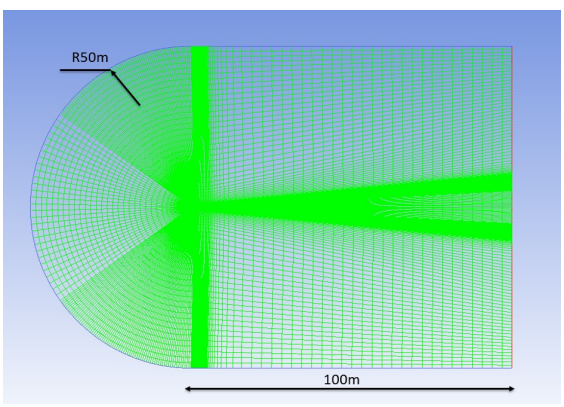

(a) Mesh highlighting domain extents

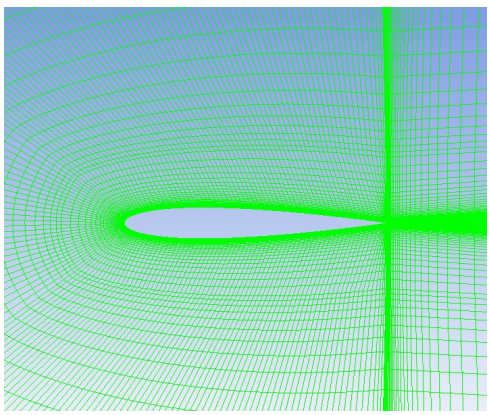

(b) Close up view of mesh near airfoil

Figure 3.8: Structured quadrilateral mesh used in harmonic pitch of NACA0012

The hysteresis curve for the dynamic moment and normal force coefficient are shown in figure 4.4. The dynamic derivatives computed by performing the inverse Fourier transforms are shown in table 4.1. The reference case has a slightly negative moment while the verification case has a slightly positive moment. Essentially, the moments around the reference point is zero and the difference is due to small moment arm difference which is in the order of the cell size that occurs on the airfoil. The dynamic derivatives for the verification case closely match that of the reference case with differences under 3%. The errors can be attributed to the differences that occur to due to mesh and solver schemes that are used in the simulation.

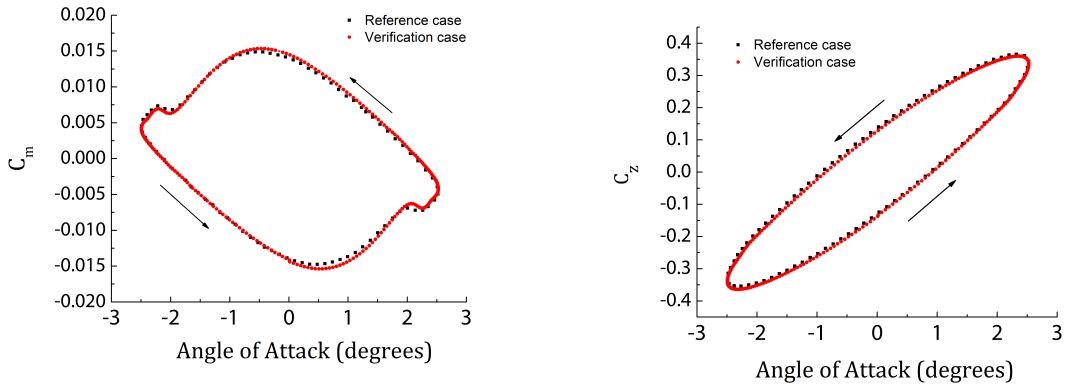

(a) Moment coefficient vs Angle of Attack

(b) Normal Force coefficient vs Angle of Attack

Figure 3.9: Force and moment Hysteresis for harmonic pitch of NACA0012 airfoil

Derivative	Reference value	Simulated value	Difference
C_{m_0}	-7.15x10^{-5}	3.43x10^{-5}	-
C_{z_0}	3.51x10^{-3}	3.66x10^{-3}	4.27%
C_{m_α}	-0.103	-0.095	7.76%
C_{z_α}	7.66	7.74	1.04%
$C_{m_{\dot{\alpha}}} + C_{m_q}$	-3.14	-3.22	2.54%
$C_{z_{\dot{\alpha}}} + C_{z_q}$	-37.2	-36.6	1.61%

Table 3.4: Comparison of dynamic derivatives for NACA0012

This verifies the method used in the thesis. Being able to obtain nearly identical set of curves ensures that the UDFs and the post processing scripts are working as intended. In the upcoming chapters, this method will be used to obtain the dynamic derivatives for the VGM. The method is almost the same with a slight excpetion of SA-RANS turbulence model being used instead of EULER model since we are interested in resolving the drag arising from viscous effects.

3.3. VALIDATION OF MULTI-FIDELITY KRIGING MODEL

The kriging-based multi-fidelity model that is used in this research, was also developed in-house. Therefore, this section serves to validate the application that was built. It is validated using Forrester function y, which is given by the equation 3.1 where $x \in [0,1]$ [34]. The low-fidelity function in this case is given by the equation 3.2. The low-fidelity function is evaluated throughout the range with a step of 0.05 while a total of four high-fidelity samples at $x = [0, 0.4, 0.6, 1]$ are used to construct the multi-fidelity kriging-based interpolation. The scaling factor is assumed to be a constant scalar and the results corresponding to different values are obtained. This is the scaling factor ζ between the low and the high-fidelity models. It should not be confused with scaling factor as used in SFT models. The results of ordinary kriging that utilizes only the high-fidelity samples are also evaluated to showcase the effectiveness of leveraging the low-fidelity results.

$$y = (6x-2)^2 \sin(12x-4) \tag{3.1}$$

$$y_{LF} = 0.5 \times (6x-2)^2 \sin(12x-4) + 10(x-0.5) - 5 \tag{3.2}$$

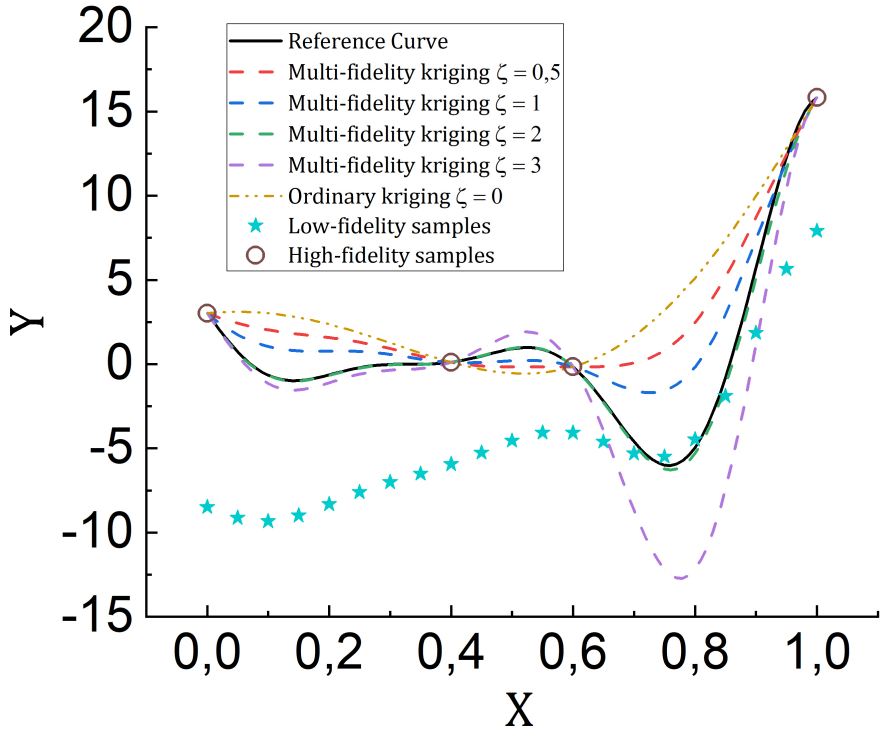

Figure 3.10: Validation of multi-Fidelity Kriging Model using Forrester Function

From figure 3.10, it can be seen that the surrogate model constructed with just using the high-fidelity evaluations fails to capture the curve under consideration. This model is the ordinary kriging model which is essentially a multi-fidelity kriging model with a scaling factor of zero. It means that the surrogate does not leverage the low-fidelity evaluations at all. The scaling factor of 2 in this case best fits the given curve while a factor of 3 results in over-scaling and factors under 2 under scale the given curve. Finding the optimal scaling factor has its own challenges.

The scaling factor in this case was modelled as a scalar constant but this can very well be a nonlinear relation. The computation already involves finding the best weights that minimize the variance in the prediction, and optimizing for the scaling factor makes the computation more expensive. Even though the low-fidelity function in this case has larger errors compared to the reference function, it does have more similarity when it comes to the location of maxima and minima. When it comes to 3DPM and RANS, it was seen that the low-fidelity function just does not behave the same as the high-fidelity function. Therefore, in this research the scaling factor will be assumed to be a constant scalar of value unity. This is a reasonable assumption since the goal of the research is to study the impact of the use of a multi-fidelity approach and not implementing the best multi-fidelity model itself.

3.4. SUMMARY

The results from the steady state simulation using RANS method were validated by comparing to that obtained from wind tunnel tests. The results as obtained from previous research work using the 3DPM were also compared. The low-fidelity 3DPM takes about 4 minutes of computational wall time for a simulation at given angle of attack while the corresponding solution from RANS roughly takes 2 hours. The RANS method is capable of predicting the separation that occurs at high angles of attack while the 3DPM fails to do so. Furthermore, drag is severely under predicted by 3DPM. The section 3.1 was able to answer the research questions regarding the accuracy and costs related to the high-fidelity methods for steady-state analysis. Section 3.2 verified the computational method that would be used in carrying out unsteady simulation for the harmonic pitch in order to compute the dynamic derivatives. The multi-fidelity Kriging model that would be utilized in this research was validated in section 3.3.

4

GRID INDEPENDENCE STUDIES

The multi-fidelity approach needs to have good accuracy and also reasonable computational time, if the method of computational scaling needs to be a feasible approach. Reducing the cost of the high-fidelity evaluations will result in overall reduction of the multi-fidelity analysis. Therefore, this chapter aims to study potential means of minimizing the computational time without losing out on accuracy. This chapter will answer the following research sub-question:

What are the costs associated with using the high-fidelity method and can they be minimized?

Coarser mesh leads to errors called discretization error[21]. The discretization errors are minimized by solving on a finer mesh. Beyond a particular refinement, the solution will remain unchanged. The Grid Independence Study(GIS) is a study conducted for obtaining the solution that is invariant of the grid size. Similarly, the size of the time steps bring in discretization errors in unsteady analysis. This chapter will study the dependence of RANS method on some of the factors that affect the computational time and accuracy of the solution. The effect of different types of meshes are studied in section 4.1 of this chapter. The steady-state cases are used to study the dependence of spatial discretization.

The unsteady simulation in this research involves computing the dynamic derivatives using the method of forced harmonic oscillation. As discussed in section 2.4 of chapter 2, the aircraft is forced to harmonically pitch in the longitudinal direction. The dynamic derivatives are then computed using inverse Fourier transforms of the resultant output forces and moments (see equation 2.21). Higher the amplitude of oscillation, the greater the motion of the mesh. The section 4.2 will study dependence of the results on the pitch amplitude of the input excitation (figure 4.1a). Solving the unsteady case requires discretization of time. The dependence on the size of time step or the total number of steps per cycle of the input excitation(figure 4.1), is studied in section 4.3. The solution needs to converge at each time step seen in figure 4.1. The section 4.4, discusses the dependence of the number of iterations employed per time step. Finally a summary of the findings are presented in section 4.5.

(a) Input excitation with varying amplitudes

(b) Input excitation with varying time step sizes

Figure 4.1: Example of input excitation for forced harmonic pitch motion

4.1. GIS USING STRUCTURED AND UNSTRUCTURED MESH

The type of cells, the size and the number of cells used in a mesh for computational analysis directly affects the results that are computed. Finer cells lead to more accurate solution but are computationally intensive while coarser cells compromise on accuracy but are relatively fast. The topology of the mesh also dictates the accuracy and computational time.

Structured meshes have cells that are related to one another and therefore avoid the need of explicit matrix that stores the mapping. This leads to structured meshes having faster convergence and lower simulation time [21]. However, creating a structured mesh is a very tedious process because of the manual labor involved. Unstructured meshes can be generated easily because of the various algorithms that automate this process. In this section, three different types of meshes are created with varying number of cell sizes in order to study the effect the grid has on the solution.

The study involves tetrahedral unstructured mesh of 5 different sizes, hexahedral structured mesh of 6 different sizes and polyhedral unstructured mesh of 5 different sizes. The polyhedral mesh is obtained by converting existing tetrahedral mesh by means of merging existing cells. The mesh utilized and the corresponding number of cells are shown in in tables 4.1, 4.2 and 4.3. The polyhedral mesh 1 is obtained by merging cells in tetrahedral mesh 1 and so forth. The construction of hexahedral mesh is totally a manual process and therefore it is easy to double or half the number of cells.

The construction of a tetrahedral mesh took roughly 3 hours while that of structured hexahedral mesh took 40 hours to pre-process. The polyhedral mesh requires the construction of a tetrahedral mesh and the conversion roughly took 15 additional minutes. As mentioned in the previous chapter, this study was carried out before the validation and in this study only half the domain was considered with symmetry plane at Y=0. The domain was $30m \times 7.5m \times 15m$ with the outlet face being 22.5m downstream of the origin and rest of the faces excluding the symmetry plane being 7.5m away. Figures 4.2, 4.3 and 4.4 shows the mesh and close up image of the main wing.

The simulations were carried out for an angle of attack of 5 degrees. The solver settings and the flow parameters are the same as that discussed in the previous chapter. But unlike the validation case, these cases are run for a total of 550 iterations wherein the solution is solved for 500 more iterations past the first 50 iterations with lower discritization schemes and under relaxation factor. It is also important to note that the reference point is that of the C.G. which is located at (0.660m,0m,-0.022m). The results of the steady state analysis for each are tabulated in tables 4.1, 4.2 and 4.3.

Unstructured Tetrahedral Mesh	Number of cells (millions)	Computational wall time (hrs)	C_L	C_D	C_m
Mesh 1	4.62	0.87	0.6975	0.0432	-0.1706
Mesh 2	6.72	1.20	0.6962	0.0422	-0.1701
Mesh 3	9.49	1.67	0.7018	0.0455	-0.1715
Mesh 4	25.66	4.40	0.7212	0.0470	-0.1755
Mesh 5	65.46	12.25	0.7219	0.0469	-0.1757

Table 4.1: GIS results of unstructured tetrahedral mesh

Unstructured Tetrahedral Mesh	Number of cells (millions)	Computational wall time (hrs)	C_L	C_D	$_Cm$
Mesh 1	1.72	0.33	0.7174	0.0436	-0.1706
Mesh 2	3.10	0.71	0.7145	0.0446	-0.1689
Mesh 3	6.13	1.27	0.7147	0.0445	-0.1701
Mesh 4	11.18	2.52	0.7129	0.0447	-0.1705
Mesh 5	22.24	4.57	0.7120	0.0447	-0.1704
Mesh 6	42.83	9.33	0.7111	0.0450	-0.1702

Table 4.2: GIS results of structured hexahedral mesh

Unstructured Tetrahedral Mesh	Number of cells (millions)	Computational wall time (hrs)	C_L	C_D	C_m
Mesh 1	2.70	0.68	0.6901	0.0427	-0.1716
Mesh 2	4.48	1.2	0.6883	0.0420	-0.1709
Mesh 3	7.49	1.7	0.6901	0.0439	-0.1699
Mesh 4	17.98	4.27	0.7248	0.0450	-0.1764
Mesh 5	24.6	7.92	0.7250	0.0450	-0.1768

Table 4.3: GIS results of unstructured polyhedral mesh

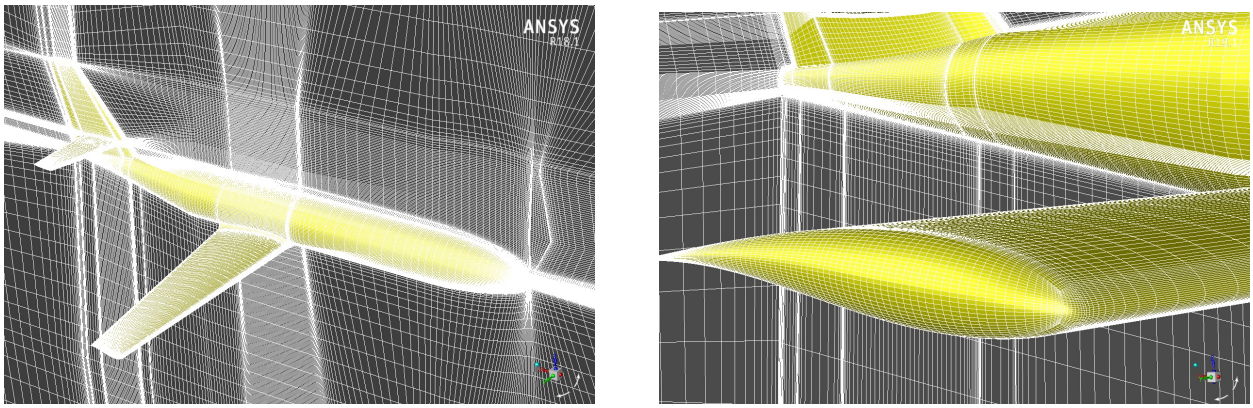

Figure 4.2: Structured Hexahedral Mesh

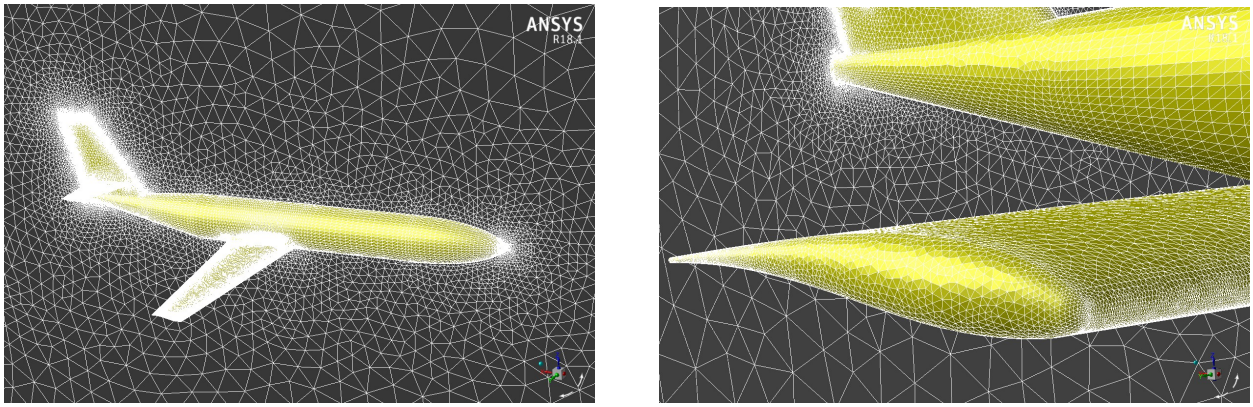

Figure 4.3: Unstructured Tetrahedral mesh

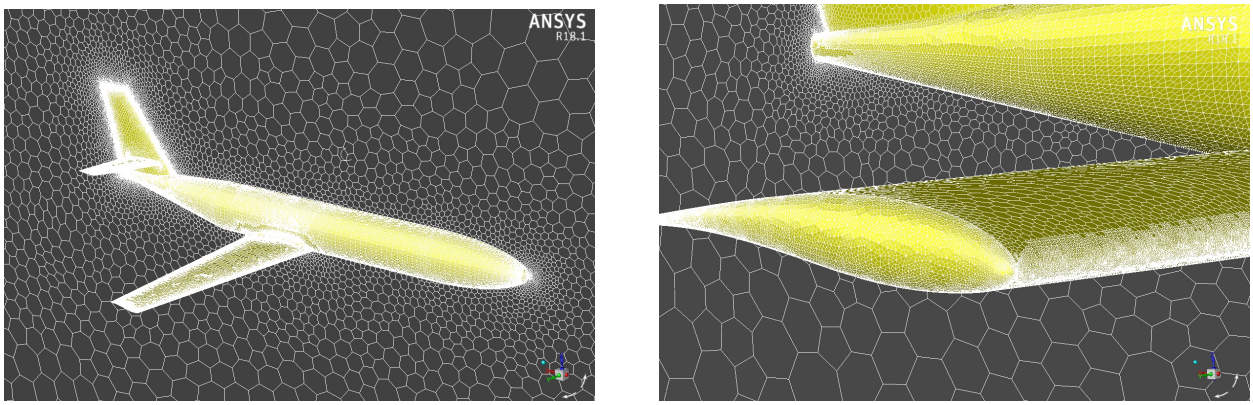

Figure 4.4: Unstructured Polyhedral mesh

Figure 4.5 highlights the results of this study. The errors that are plotted are relative to the values that correspond to the mesh with highest grid size in each type of mesh. In figure 4.5a the computational cost for each mesh can be seen. The slope of the curve for the polyhedral mesh is higher than that of the tetrahedral mesh. This means that the polyhedral cells have higher simulation time for a given number of cells but since a small number of cells can fill up a given domain size, the overall simulation time is still reduced. The tetrahedral mesh 5 consisting of roughly 65 million cells was reduced to 25 million polyhedral cells. The corresponding reduction in computational time was 35%. The polyhedral mesh 3 roughly takes the same time as that of the tetrahedral mesh 3 and there is no extra merit to merging the cells before solving. The hexahedral cells show a higher slope than the tetrahedral cells but this is just because of solving both the structured and unstructured mesh using ANSYS fluent. The software stores both the meshes as unstructured meshes and the solver does not use dedicated algorithm into solving the structured mesh. Despite not taking advantage of the structured behaviour, the mesh still sees a benefit of the cells being oriented more perpendicularly to the fluid flow.

From figures 4.5b, 4.5c and 4.5d, it can be seen that in the case of unstructured tetrahedral mesh, it takes roughly 25 million cells to reach grid independence but this is achieved much sooner when a structured mesh is employed. A structured mesh with roughly 6 million cells has similar accuracy as that of a unstructured mesh with 25 million cells. In such a case, the structured mesh has a computational cost that is 70% lower than that of the corresponding unstructured mesh with similar accuracy. The cost can potentially be further reduced by employing dedicated algorithm for solving the structured mesh. The residuals had already reduced by 7 orders past the 200 iteration mark and therefore a total of 300 iterations were considered sufficient for future simulation.

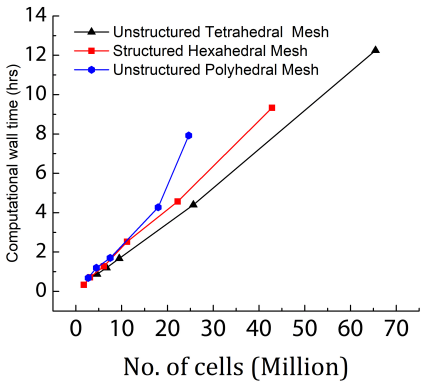

(a) Computational wall time Vs number of cells

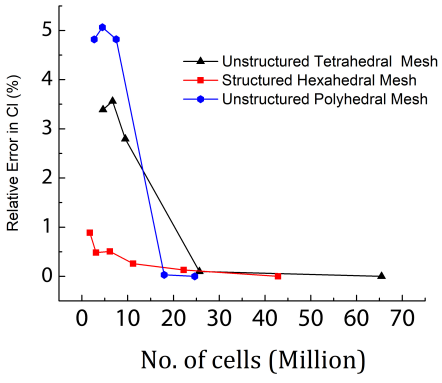

(b) Relative error in Lift coefficient Vs number of cells

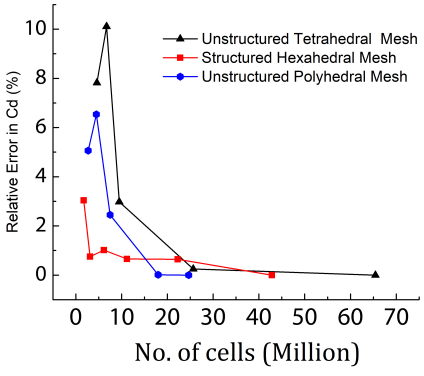

(c) Relative error in Drag coefficient Vs number of cells

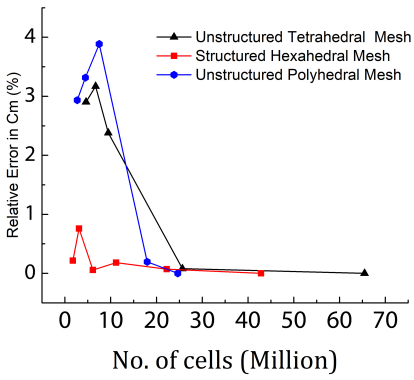

(d) Relative error in Moment coefficient Vs number of cells

Figure 4.5: Computational time and associated relative errors from GIS

After conducting the GIS, the tetrahedral mesh 3 was considered as optimum since the deviations were less than 3% while in the case of structured mesh , mesh 4 was selected as optimal since the computational time was roughly similar to that of the unstructured mesh 3. In the case of polyhedral mesh, the mesh obtained from the conversion of tetrahedral mesh 3 was considered as optimal. Using these three meshes that are highlighted in figure 4.2, 4.3 and 4.4, the lift, drag and moment polars are generated for angles of attack

ranging from -5 to +14 deg. The figure 4.6 shows the results of this study. The results from the wind tunnel and the 3DPM have also been plotted for reference. The moments were converted back to the reference point as used in the wind tunnel experiment.

Looking at the lift curve in figure 4.6a, it can be seen that the structured mesh has the best match to that of the wind tunnel results. The results from the polyhedral mesh do have lower errors at high angles of attack but it fails to resolve the separation that occurs from 9 degree AoA. In figure 4.6b, the hexahedral and the polyhedral mesh roughly predict 8 drag counts lower than the tetrahedral mesh. Even in this case the structured mesh has a better match with the wind tunnel results at higher AoA than the tetrahedral mesh. The noisy behaviour of the polyhedral mesh can once again be seen here. Finally, the moment polars can be seen in figure 4.6c. Once again, the trend is similar to that of the lift curve with the structured mesh displaying less noisy behaviour at high AoA compared to that of the unstructured mesh.

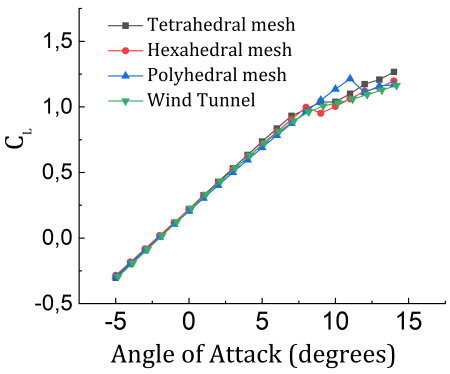

(a) Lift Coefficient Vs Angle of attack

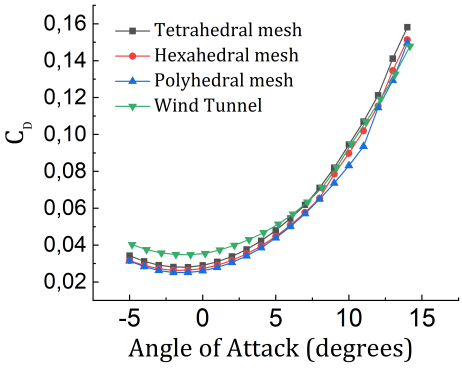

(b) Drag Coefficient Vs Angle of attack

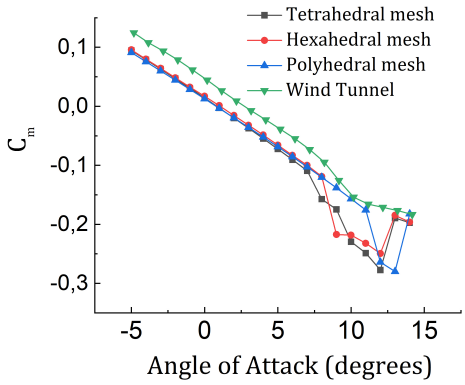

(c) Moment Coefficient Vs Angle of attack

Figure 4.6: Lift, drag and moment polars for GIS

For results with similar accuracy, the structured mesh roughly provides the solution in half the time compared to unstructured mesh. The mesh roughly takes 13 times more pre-processing time compared to that of the unstructured mesh but this is mainly due to the process being mostly manual. With the use of KBE, this process can be automated in the future to produce good quality structured meshes. Unfortunately the structured mesh utilized in this research kept breaking down during mesh motion. This was due to few highly skewed cells within the domain. The task of generating structured meshes of better quality was very time consuming. Therefore, only unstructured meshes were used for the dynamic analysis.

4.2. DEPENDENCE ON PITCH AMPLITUDE

This section studies the influence of the pitch amplitude, α_A of the harmonic excitation on the dynamic derivatives of the VGM.The simulation is carried out with three different amplitudes for Mach number of 0.13 and reduced frequency of 0.05 for mean AoA of zero degrees. A total of three cycles are simulated with each cycle containing 64 time steps and 30 inner iterations per time step.

Since all simulations were carried out for the same number of cycles, time steps and inner iterations, they had the same cost of 36hrs of wall time. The hysteresis curves for forces and moments are shown in figure 4.7 and the corresponding time domain curves are shown in figure 4.8. The size of time step in each of these cases is the same but the mesh needs to move a larger amount for higher amplitudes. This results in larger step sizes with respect to angle of attack. The figure 4.9 and 4.10 show the static and dynamic derivatives. The variation in the results are around 0.1%. The number of time steps per cycle was 64 and this provided a sufficient resolution. Therefore, it can be concluded that the pitch amplitude does not influence the accuracy of the derivatives that are computed under these conditions. An amplitude of two degrees will be used for all upcoming simulations.

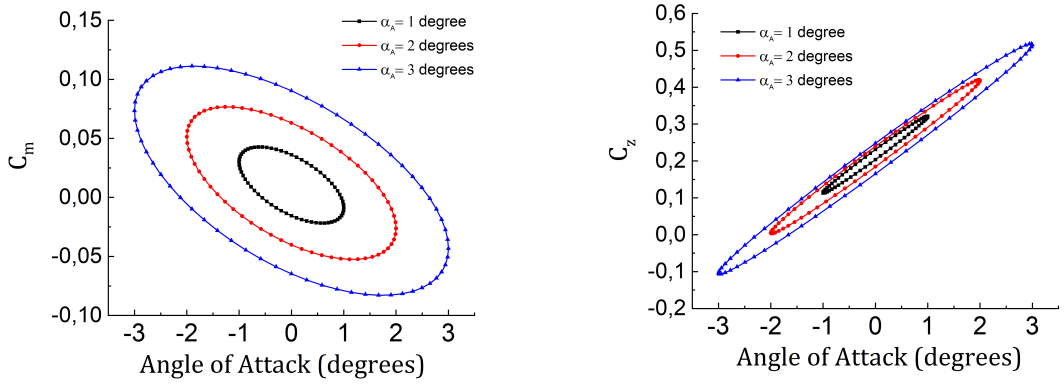

(a) Moment coefficient vs Angle of Attack

(b) Normal Force coefficient vs Angle of Attack

Figure 4.7: Hysteresis curves for amplitude dependence

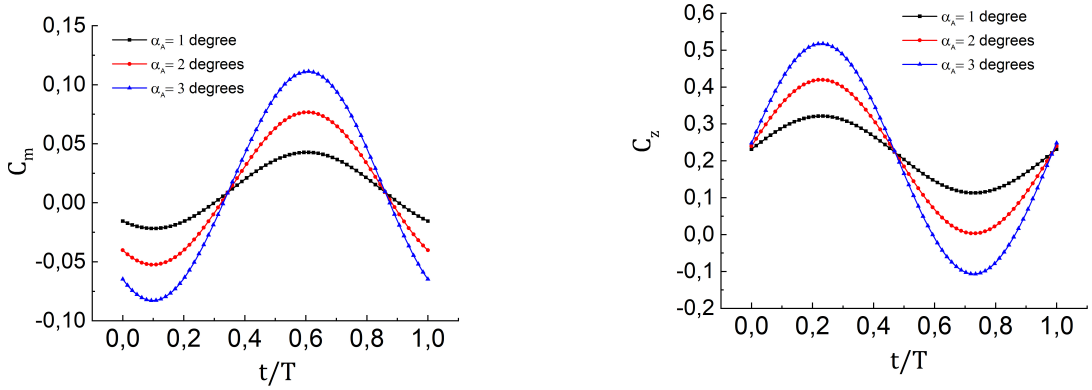

(a) Moment coefficient vs Normalized time

(b) Normal Force coefficient vs Normalized time

Figure 4.8: Time Domain curves for amplitude dependence

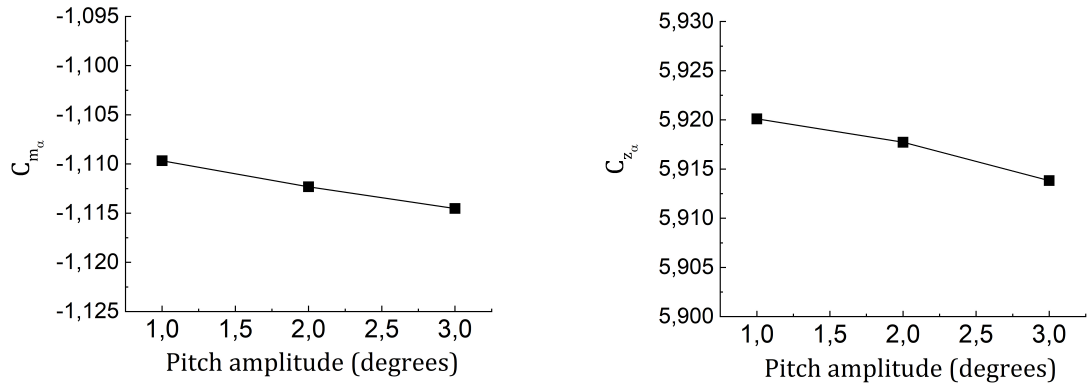

(a) moment coefficient derivative

(b) normal force coefficient derivative

Figure 4.9: Static derivatives Vs pitch amplitude

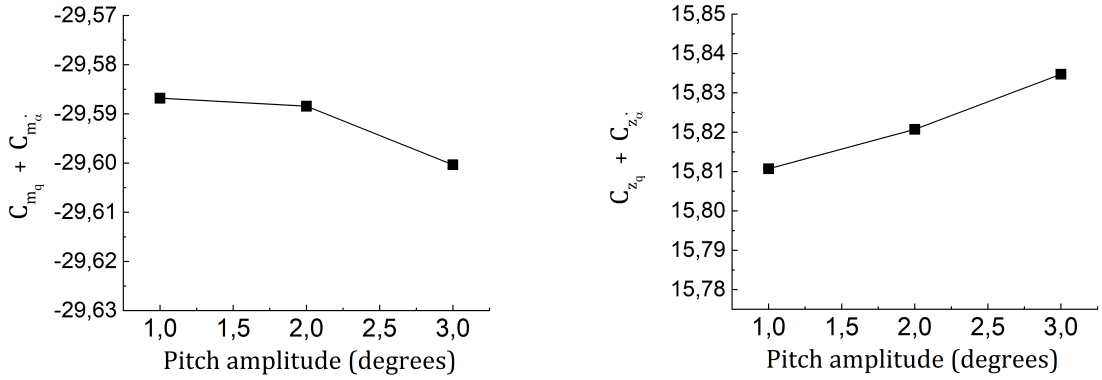

(a) moment coefficient derivative

(b) normal force coefficient derivative

Figure 4.10: Dynamic derivatives Vs pitch amplitude

4.3. DEPENDENCE ON NUMBER OF TIME STEPS

The unsteady solutions require discretization of time. A larger time step size will bring in more discretization error. The harmonic motion is simulated for given number of cycles. The frequency of the solution determines the time period T of the solution. The time step size is determined by the number of divisions/steps considered per cycle. More time steps results in smaller step sizes, thereby getting better accuracy. Conversely, lesser time steps imply larger step sizes and more errors. Larger steps also mean that the cycle is traversed faster. This section studies the influence of the time steps per cycle that are employed for simulating the longitudinal pitch of the VGM. The aim is to find an optimum number of time steps that is both accurate and computationally not expensive. The simulation is carried out for a set of four different number of divisions/time steps for pitching motion, for Mach number of 0.13 and reduced frequency of 0.05 for mean AoA of zero degrees and amplitude of two degrees. A total of three cycles are simulated with each cycle containing 30 inner iterations per time step.

From figure 4.11 it can be seen that as the number of divisions per cycle are reduced the hysteresis loop bulge up on one side of the motion. This motion as the aircraft pitches from the max angle of attack to the minimum as can be seen in figure 4.12. The lag between the reaction and the input disturbance is typical of any hysteresis loop but in this case the lag simply arises from insufficient resolution of the pitching motion that is simulated. Consequently the dynamic derivatives that are computed have higher errors for lower number of time steps (seen in figure 4.14). From fig 4.13 it can be seen that the static derivatives are not really affected and have errors less than 0.5%. Figure 4.15 shows the computational time incurred vs number of time steps per cycle.

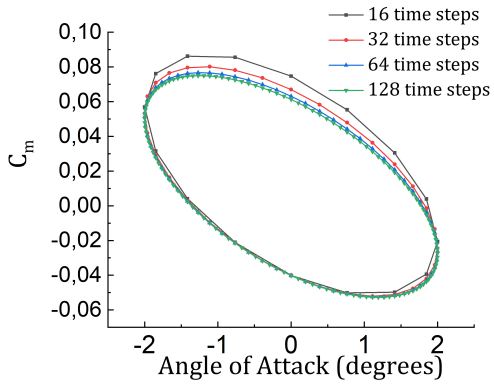

(a) Moment coefficient vs Angle of Attack

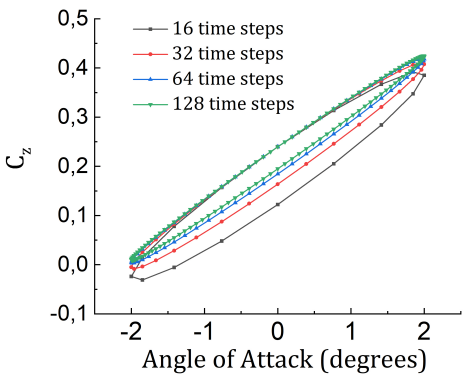

(b) Normal Force coefficient vs Angle of Attack

Figure 4.11: Hysteresis curves for dependence on number of time steps

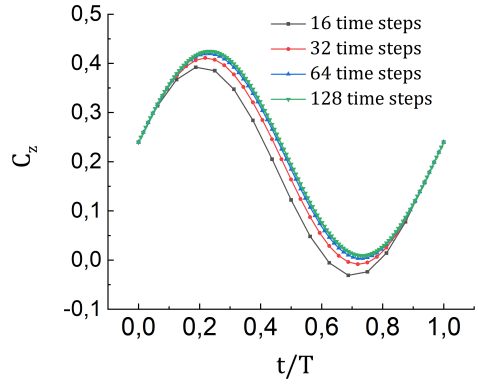

(a) Moment coefficient vs normalized time

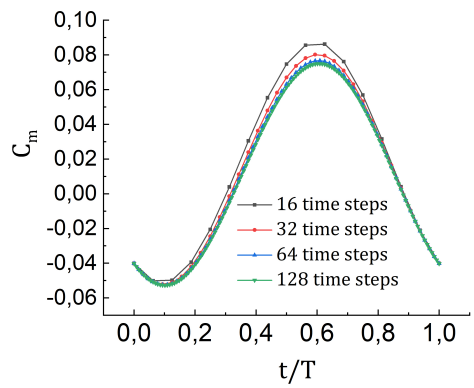

(b) Normal Force coefficient vs normalized time

Figure 4.12: Time Domain curves for dependence on number of time steps

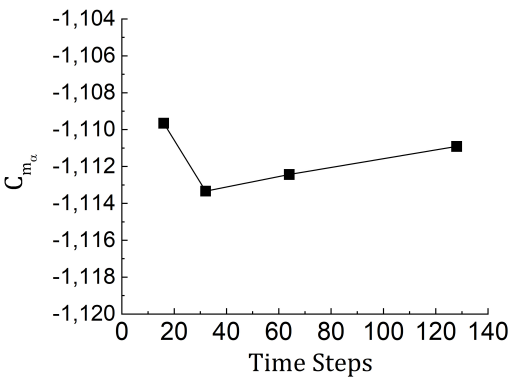

(a) Moment coefficient

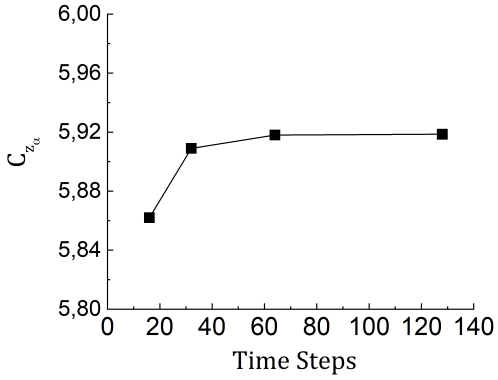

(b) Normal Force coefficient

Figure 4.13: Static derivatives Vs number of time steps

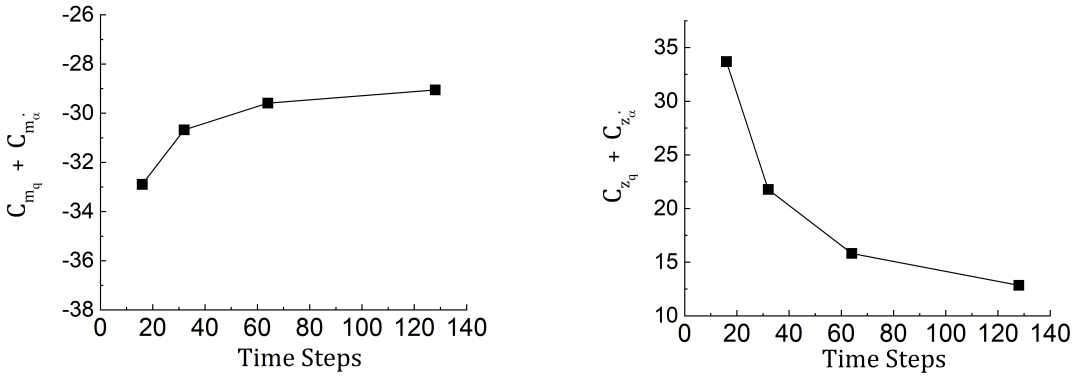

(a) Moment coefficient

(b) normal force coefficient

Figure 4.14: Dynamic derivatives Vs number of time steps

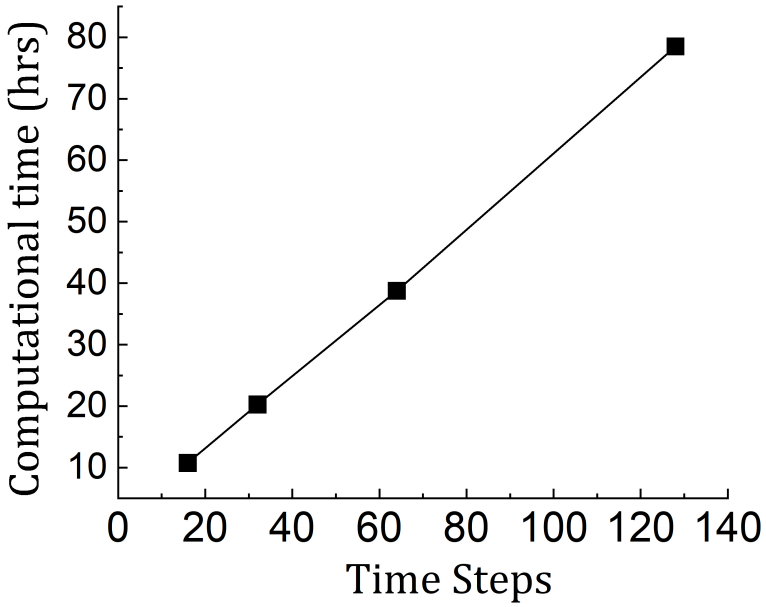

Figure 4.15: Wall time vs time steps

Compared to the case with 128 time steps, the one with 64 time steps has an error or 3% in the case of dynamic moment derivative, and the normal force coefficient derivative has an error of 8%. Given that the computation time of the case with 64 time steps is half that of the 128 time steps, it is optimal to use 64 steps in all the upcoming cases.

4.4. DEPENDENCE ON NUMBER OF ITERATIONS PER TIME STEP

This section studies the influence of the iterations on the computational time and errors. These iterations are necessary for convergence of a solution at a given time step. The simulation was carried out for a set of five different number of divisions of pitching motion, for Mach number of 0.13 and reduced frequency of 0.05 for mean AoA of zero degrees and amplitude of two degrees. A total of two cycles are simulated with each cycle containing 64 time steps per cycle. Two cycles as opposed to three in the previous section, will also help to gauge the impact of cutting the simulation sooner.

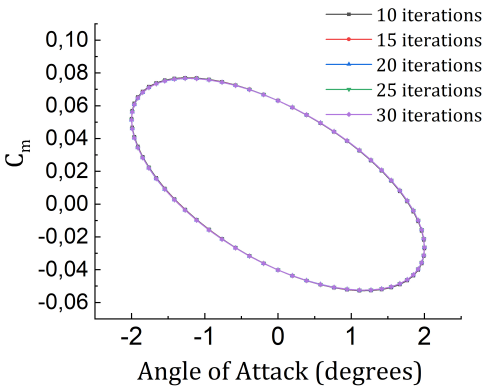

(a) Moment coefficient vs Angle of Attack

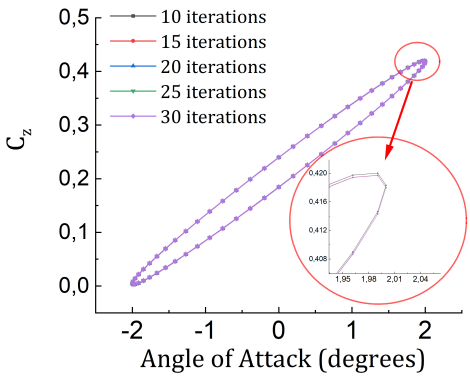

(b) Normal Force coefficient vs Angle of Attack

Figure 4.16: Hysteresis curves for dependence on iterations

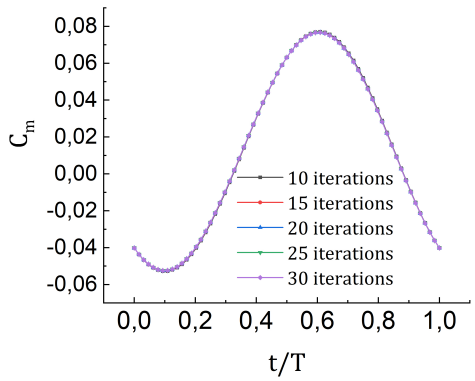

(a) Moment coefficient vs normalized time

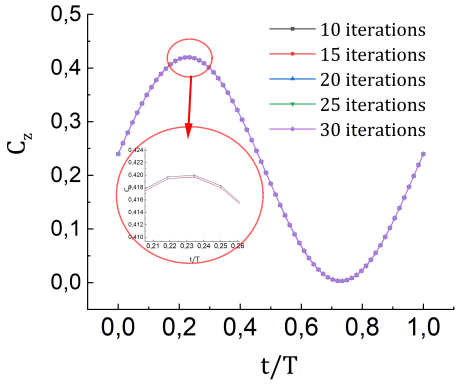

(b) Normal Force coefficient vs normalized time

Figure 4.17: Time Domain curves for dependence on iterations

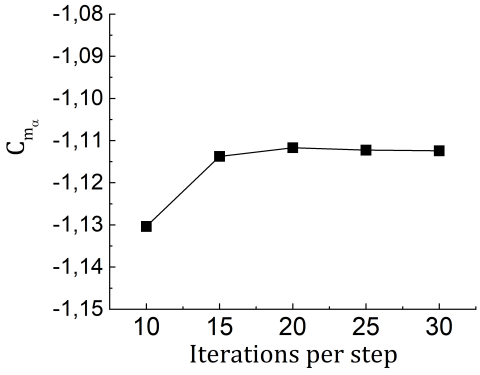

(a) Moment coefficient

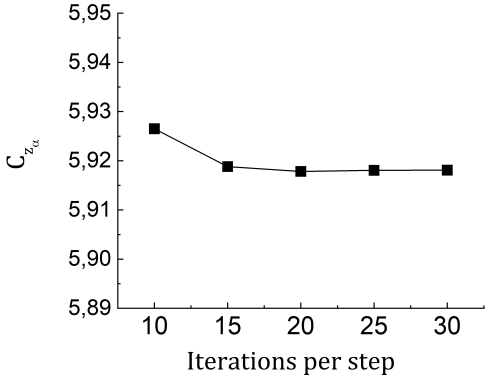

(b) Normal Force coefficient

Figure 4.18: Static derivatives Vs iterations

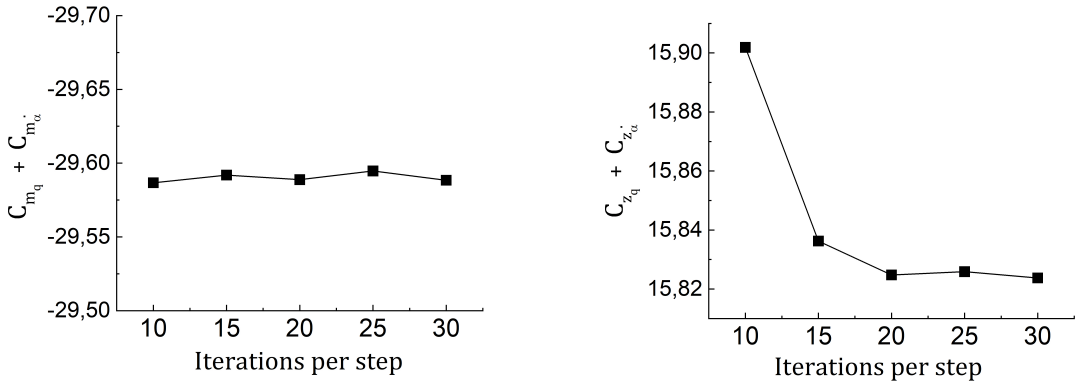

(a) Moment coefficient

(b) Normal Force coefficient

Figure 4.19: Dynamic derivatives Vs iterations

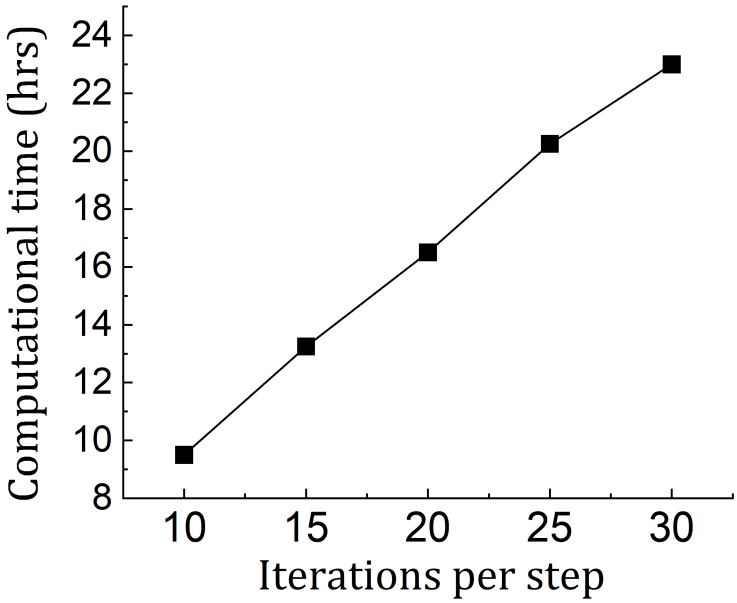

Figure 4.20: Computational time vs iterations

The time step corresponding to 64 division for a reduced frequency of 0.05 is already in the order of milliseconds, and reducing the inner iterations per time step is not as penalizing in terms of the errors that are encountered. The force and moment curves are almost overlapping with the case of 10 iterations being slightly more bulged towards the peaks as seen in figure 4.16 and 4.17. The computational time can be significantly reduced by choosing 20 inner iterations compared to 30. This only leads to a drop in accuracy by roughly 0.1% while being able to save computational time by 30% as can be seen in figure 4.19 and 4.20. Furthermore, the case corresponding to 30 iterations in this section utilizes 64 time steps per cycle for a total of two cycles. This roughly costs 24 hours of computational time. In the previous section the case corresponding to 64 time steps used 30 inner iterations per time step and a total of 3 cycles. This cost 40 hours of computational time (seen in figure 4.15). The errors in the dynamic derivatives are again less than 0.5%. Therefore, it can be concluded that 20 iterations between time steps, with 64 time steps per cycle and a total of 2 cycles are optimal parameters for dynamic simulation of VGM at k=0.05.

4.5. SUMMARY

The section 4.1 discussed the influence of different types of mesh on the accuracy and computational costs in predicting the static aerodynamic data. The structured mesh shows the most promise with higher accuracy and lower computational time. The downside of generation of a structured mesh can be overcome with use of concepts of KBE in the future.

The errors are more sensitive to the time steps that are considered and a total of 64 divisions per cycle for reduced frequency of 0.05 is seen to be a good compromise from the study in section 4.3. A total of 20 inner iterations per time step is sufficient as found from section 4.4. Since the study in section 4.3 considered three cycles and the one in 4.4 considered two, it can be further concluded that the third cycle does not improve the results to justify simulating the extra cycle. With each cycle costing the same computational time, a reduction in computational time by 33% can be achieved by just simulating two cycles of dynamic motion compared to simulating 3 cycles. Considering these parameters, a dynamic simulation roughly takes 19 hours for evaluation at the reduced frequency of k=0.05 which is a total of 21 hours including the computational time for the steady state simulation, which serves as the initial condition for a dynamic case. Thus, this chapter provided an answer to the first research sub-question.

5

RESULTS AND DISCUSSION

The generation of aerodynamic database required for the method of computational scaling, for the design of SFT model, is computationally intensive. Accurate results are required to establish similitude between the SFT model and the full-scale aircraft design. At the same time, we require the evaluations to be made in a reasonable time frame. Otherwise the method of computational scaling will be infeasible for the design of SFT models. In order to support the method of computational scaling, this research developed a multi-fidelity surrogate model for generating the aerodynamic database. The method utilizes the previously used 3DPM as the low-fidelity method, and RANS as the high-fidelity method. The 3DPM had issues with accuracy, while single fidelity RANS method was too expensive to be used [27]. This chapter provides answers to the following sub-questions that would help answer the main question.

1. How accurate is the low-fidelity method relative to high-fidelity method?
2. What is the cost and accuracy of the multi-fidelity surrogate model?
3. Does the multi-fidelity surrogate model actually show any value compared to using a surrogate-based high-fidelity approach?

The 3DPM is known to show insensitivity to changes in reduced frequency, and the errors in dynamic derivatives obtained from a quasi-steady analysis were never quantified. The results from RANS will be used as a reference to quantify the errors with 3DPM and the surrogate models. It is important to note that the high-fidelity method of RANS, is not free from computational errors. But for the purpose of this research, the errors discussed in this chapter are relative to RANS. The first sub-question is answered by a dynamic analysis of Variable Geometry Model (VGM, a 8.8% geometrically scaled model of Cessna Citation II 550) using 3DPM and RANS, and comparing the results. Case studies and time studies are performed using multi-fidelity surrogate model with varying sample sizes, in order to answer the second sub-question. The studies are split for the static and dynamic analysis. The predictions from the ordinary kriging-based surrogate model are also used as a secondary reference. This will help assess if the 3DPM is truly providing any leverage. The performance of this surrogate-based high-fidelity approach would help answer the third sub-question mentioned above.

The section 5.1 discusses the results of the dynamic analysis of VGM using RANS. This serves as the reference to compare the results of the 3DPM. This section consists of two case studies. A dynamic analysis for varying angles of attack and other with varying reduced frequency. A case study for the surrogate models for static analysis is presented in section 5.2. The table 5.2 specifies each case. Note that the 3DPM is a specific case of a surrogate model where no RANS samples are used. Similarly, the section 5.3 discusses the results of the surrogate models for dynamic analysis. The details of each case can be found in table 5.3. The section 5.4 provides a time study for the surrogate models used in sections 5.2 and 5.3. Finally a summary of the results is provided in section 5.5. The table 5.1 provides an overview of each section in this chapter.

5.1. DYNAMIC ANALYSIS OF VGM

Before creating the multi-fidelity surrogate models, the results of the dynamic analysis of VGM are discussed in this section. The dynamic motion in this research is restricted to harmonic longitudinal pitching of the

Section	Purpose	Total cases
5.1	Assessment of accuracy of 3DPM relative to RANS	2
5.2	Assessment of accuracy of Surrogate models for static analysis	9
5.3	Assessment of accuracy of Surrogate models for dynamic analysis	6
5.4	Assessment of computational time of Surrogate models	2

Table 5.1: Overview of studies performed in each section

aircraft. The input parameters that vary are the mean angle of attack and reduced frequency for the motion. The dynamic derivatives for varying angle of attack at a given reduced frequency are discussed in subsection 5.1.1. Subsection 5.1.2 would then discuss the dynamic derivative for varying reduced frequency at a given angle of attack.

5.1.1. DYNAMIC DERIVATIVE FOR VARYING ANGLES OF ATTACK

The VGM is simulated for longitudinal pitch for a mach number of 0.13 and reduced frequency of 0.05 for angles of attack ranging from -4 to +14 in intervals of 2 degrees. The amplitude of oscillation is 2 degrees. Two cycles are simulated with each cycle containing 64 time steps and 20 inner iterations per time step. The decision for the simulation parameters are based on the sensitivity study previously conducted. The reference point for the moment that was considered here was (0.680m,0m,-0.0565m) with respect to nose of the fuselage (see figure 3.2). The dynamic derivatives are shown in the figure 5.1.

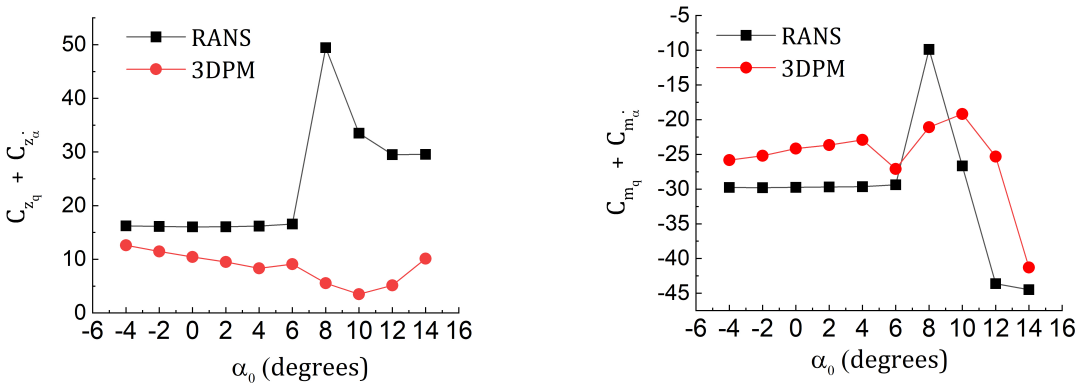

(a) Normal Force coefficient derivative vs Angle of attack

(b) Moment coefficient derivative vs Angle of attack

Figure 5.1: Dynamic derivatives for harmonic pitch of VGM for varying AoA

The figure 5.1a shows the dynamic derivative for the normal force coefficient for varying angles of attack. The hysteresis curves at each mean angle of attack, can be found in appendix B. For low angles of attack upto 6 degrees the slope of the graph is zero indicating that the dynamic forces also have a linear behaviour in this region. A spike is seen at 8 degrees which is a result of the aircraft encountering separated flow. The dynamic moment derivative as seen in figure 5.1b also shows a similar behaviour i.e, a spike. The 3DPM results contain some noise but it also comes close in capturing the trend at lower angles of attack. Compared to the high fidelity RANS method, the 3DPM roughly has 35% error in the prediction of the normal force dynamic derivative and about 20% in the case of the dynamic derivatives for moments.

5.1.2. DYNAMIC DERIVATIVE FOR VARYING REDUCED FREQUENCIES

The dynamic simulation for the VGM is performed at three different reduced frequencies of k=[0.002, 0.01,0.05] at mean angle of attack of zero and amplitude of two degrees. Two cycles are simulated using first order transient formulation. The simulation in this case study were performed using 64 time steps per cycle. But decreasing the reduced frequency leads to increase in the time period of oscillation. Therefore, the case with

a reduced frequency of 0.01 and 0.002 used 96 and 128 time steps per cycle receptively. This leads to an increase in computational time as the frequencies are reduced. The case with the reduced frequency of 0.002 roughly takes 56 hours while that of 0.01 takes 43 hours of wall time. The reference point for the moment that was considered in this study was the c.g. location of (0.660m,0m,-0.022m) from the nose of the fuselage (see figure 3.2).

The output signal for the normal force coefficient and the moment coefficient in the normalized time domain are shown in figure 5.2 and the corresponding hysteresis are shown in figure 5.3. The figure 5.2a shows the normal force coefficient against the time which is normalized with the cycle's time period. The simulation starts with the aircraft at zero degrees and then moves towards a peak of +2deg after which it pitches to -2 and then returns to the mean position. The dynamic normal force is lower than corresponding steady state normal force as it reaches the peak, and higher than the corresponding steady state normal force coefficient as it moves towards a trough. Theses differences increase as the magnitude of the reduced frequency increases which shows the effects of unsteadiness in the flow. The corresponding hysteresis shown in figure 5.3a highlights this effect with the progressive increase in the thickness of the loop as the reduced frequency increases.

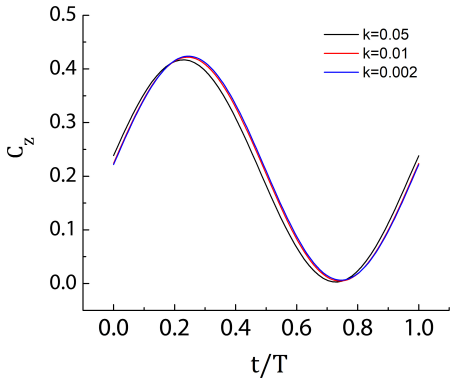

(a) Normal Force coefficient vs Normalized time

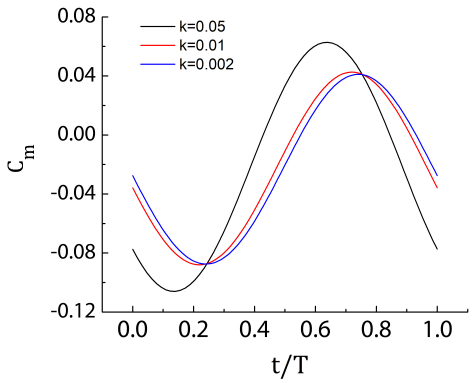

(b) Moment coefficient vs Normalized time

Figure 5.2: Force and moment history for harmonic pitch of VGM

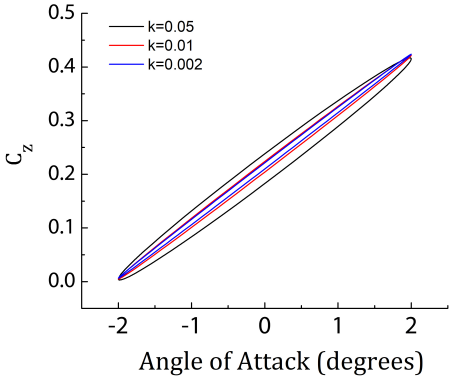

(a) Normal Force coefficient vs Angle of Attack

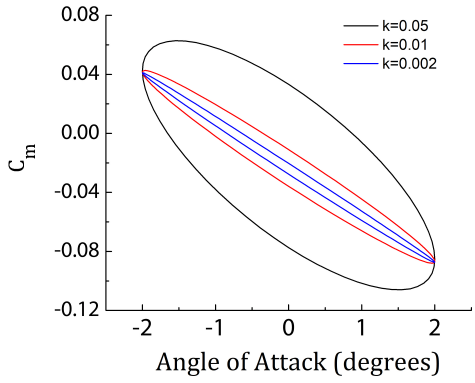

(b) Moment coefficient vs Angle of Attack

Figure 5.3: Force and moment Hysteresis for harmonic pitch of VGM

A similar effect is seen with the moments as can be seen in the time domain plot in figure 5.2b and the hysteresis plot in figure 5.3b. The hysteresis loop for the moments are much thicker than that of the normal forces. This is only a consequence of the choice of the moment center that is considered that scales the effects of the forces on the body. But it is important to note that the as the unsteadiness increases, i.e. as value of reduced frequency is higher, the more the forces deviate from the steady-state lift. Since the 3DPM is incapable of providing the forces in dynamic manner, the dynamic derivatives computed are compared to that of the RANS.

The combined derivatives that are obtained are plotted in figure 5.4 along with that obtained from the 3DPM. The figure 5.4a compares the dynamic derivative for the normal force coefficient for varying reduced frequency. It can be seen that the 3DPM is insensitive to the changes in reduced frequency which is a direct consequence of the quasi-steady process-based evaluation. The 3DPM is less accurate at evaluating the dynamic derivative at lower frequency. The accuracy does improve at higher frequency. But the major problem is the insensitivity of the 3DPM towards changes in reduced frequency. The figure 5.4b shows the dynamic derivatives for the moment coefficient for varying angles of attack and once again a similar behaviour can be seen where the 3DPM is roughly insensitive to the reduced frequency with the relative errors being the larger as the frequency is decreased.

The 3DPM is insensitive to changes in reduced frequency. This research does not model the scaling factor ζ. It is assumed to be a constant. A multi-fidelity surrogate model with such an assumption cannot be created. This is because the low-fidelity function is a constant function itself. In this research, the multi-fidelity model is created using a different quantity that is not a constant. The equation 2.22 for obtaining the dynamic derivative using the quasi steady method can be rearranged into the following:

$$(C_{z_q} + C_{z_{\dot{\alpha}}}).k = C_z^{QS} - C_z^S \tag{5.1}$$

The dynamic derivative multiplied by the reduced frequency is essentially the difference in the force or moment coefficient between the ones obtained for a steady-state and the corresponding quasi-steady analysis. This quantity does vary as the reduced frequency changes(seen on the right Y-axis of figure 5.4), and it allows for the creation of multi-fidelity surrogate model. It will be used to create the surrogate model and discuss the errors henceforth. In the case of the dynamic derivative for normal coefficient, the relative error is about 88% at the lowest reduced frequency and about 34% for the highest frequency considered in the study. For the dynamic derivative for moment coefficient, the error is about 59% at the lowest reduced frequency and about 24% at the highest. The curves of RANS and 3DPM diverge, which implies greater absolute error with increasing frequency. Therefore, the absolute value of the predicted forces and moment co-efficient by the 3DPM is poor, and increases with increasing unsteadiness in the flow.

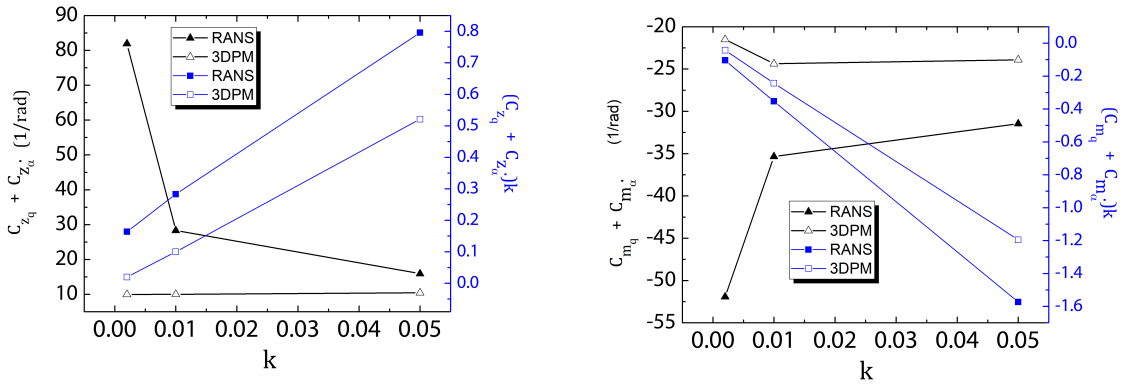

(a) Normal force coefficient derivative vs reduced frequency

(b) Moment coefficient derivative vs reduced frequency

Figure 5.4: Dynamic derivative vs reduced frequency

5.2. CASE STUDY FOR MULTI-FIDELITY STATIC ANALYSIS

This section discusses the results of the case studies of multi-fidelity surrogate model for the static analysis. Varied number of high-fidelity RANS samples are picked to best illustrate the effectiveness and limitations of using surrogate model. The sample set contains one data point to 5 data points. The ordinary kriging which serves as a secondary reference, can be constructed when there are three or more sample points from the high-fidelity method.

The table 5.2 gives the description of the case studies considered and the corresponding computational time. The case number 1 corresponds to the single-fidelity 3DPM, which is in need of accuracy improvement. It roughly takes four minutes a case for the 3DPM to evaluate a given angle of attack while it takes roughly 2 hours for one simulation by RANS. The computational time for the surrogate model predictions are in the order of milliseconds, which is negligible when compared with other quantities. Therefore the cost of running a multi-fidelity analysis would be the cost of running each sample point and that of the full set of the 3DPM evaluations. The ordinary kriging model predicts based on just the high fidelity samples, therefore it saves the time that is required in obtaining the low fidelity results.

Case Number	Description	Computational Time (hrs)	Discussed in
1	Single-Fidelity 3DPM	1.3	All
2	Multi-fidelity kriging with one sample	3.3	5.2.1
3	Multi-fidelity kriging with two samples	5.3	5.2.2
4	Ordinary-Kriging with three samples	6	5.2.3
5	Multi-fidelity kriging with three samples	7.3	5.2.3
6	Ordinary Kriging with four samples	8	5.2.4
7	Multi-fidelity kriging with foursamples	9.3	5.2.4
8	Ordinary Kriging with five samples	10	5.2.5
9	Multi-fidelity kriging with five samples	11.3	5.2.5

Table 5.2: Surrogate Model used for static analysis

5.2.1. CASE STUDY USING ONE HIGH-FIDELITY SAMPLE

This subsection discusses the results of the case number 2 of table 5.2 of this study. One high fidelity sample at 0 degree angle of attack is utilized in construction of the surrogate model. A single data point offers insufficient information into constructing the ordinary kriging model whereas a multi-fidelity kriging model can be constructed by leveraging the information from the low fidelity data. The lift curve can be seen in figure 5.5. It can be seen that the multi-fidelity curve has a better match at low angles of attack but results in over prediction of the lift coefficient at higher angles compared to the 3DPM. The drag curve sees a major benefit of multi-fidelity approach as seen in figure 5.6. At low angles of attack it has a very good match. At higher angles, the drag is under predicted compared to the reference RANS data but there is still some improvement in accuracy as compared to that of the 3DPM. The RMSE of the 3DPM are reduced by 37.5% by utilizing a sample from the RANS.

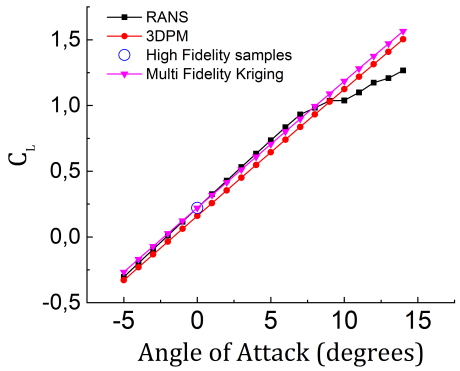

Figure 5.5: Multi-fidelity Lift Curve using one sample

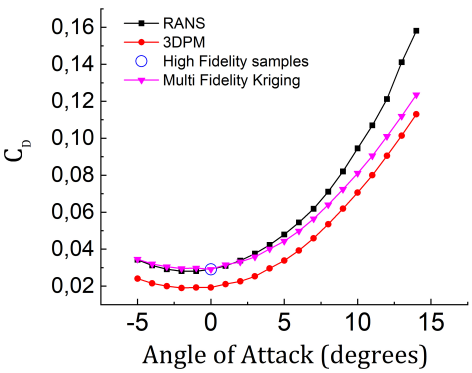

Figure 5.6: Multi-fidelity Drag Curve using one sample

The moment curve as seen in figure 5.7 shows a behaviour similar to that of the lift where the predicted values have a good match at lower angles of attack but get worse than the 3DPM at higher angles.

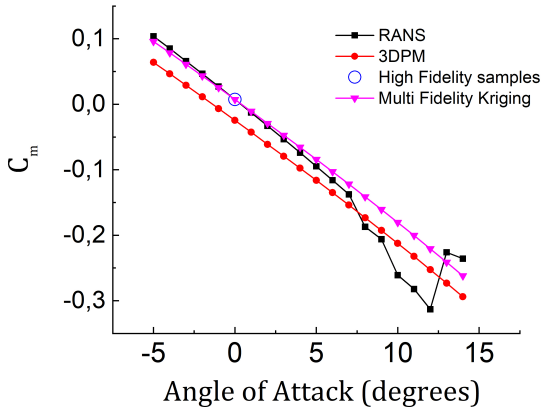

Figure 5.7: Multi-fidelity Moment Curve using one sample

5.2.2. CASE STUDY USING TWO HIGH-FIDELITY SAMPLES

For case number 3 of table 5.2, two high-fidelity samples are considered, one at an angle of attack of -1 deg and the other at 10 degrees. These points lie on the first and the third quartile of the range respectively. The results of this surrogate model are discussed in this section. Like the previous study, two points do not provide sufficient information to construct an ordinary kriging-based surrogate model. From figure 5.8, it can be seen that the multi-fidelity surrogate model has a better match with the reference data compared to just using a single point. However it also needs to be noted that, it was a consequence of having a high-fidelity sample in the non-linear region. Since the 3DPM provides no indication of separation, the sample selected at higher angles of attack need not always undergo separation. Although the curve has a better fit at higher angles of attack, it comes with a compromise of accuracy at angles of attack ranging from 2 to 7 degrees when compared to that of the model with a single sample.

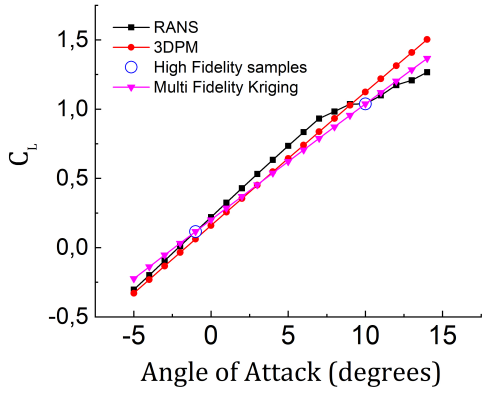

Figure 5.8: Multi-fidelity Lift Curve using two samples

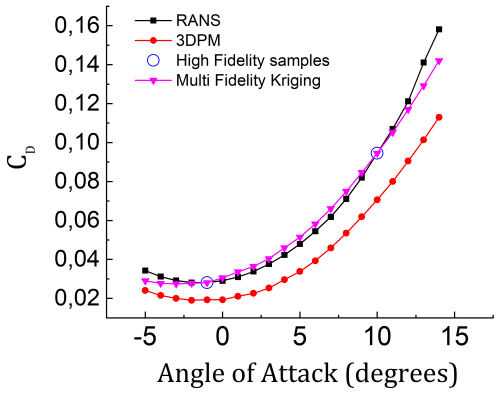

Figure 5.9: Multi-fidelity Drag Curve using two samples

The drag polar as seen in 5.9 has a better fit at higher angles as compared to that of the model with a single sample. But once again the accuracy is slightly compromised at lower angles of attack. The RMSE is reduced by 75% in this case. The moment curve also shows a similar behavior as that of the lift curve with two samples. From angles of attack from -5 to -1 degrees and from +10 to +14 degrees we see under prediction of the drag while that between -1 to +10 contains slight over prediction. These errors can be further minimized by using the optimal scaling factor (see 3.3) between the two methods, but this is outside the scope of this study.

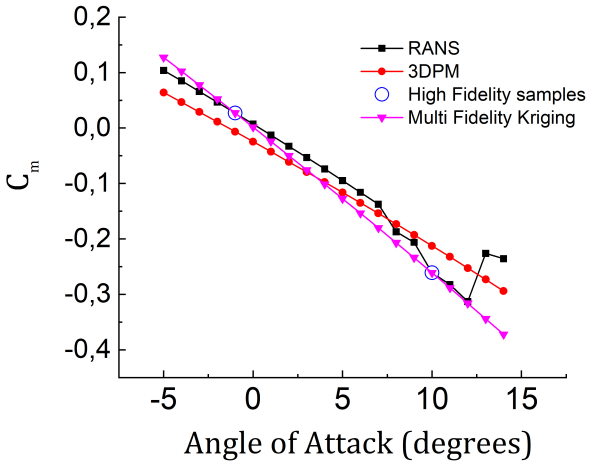

Figure 5.10: Multi-fidelity Moment Curve using two samples

5.2.3. CASE STUDY USING THREE HIGH-FIDELITY SAMPLES

The results of the surrogate model utilizing three high-fidelity samples are discussed in this section. The samples are taken at an angle of attack of -3,4 and 12 degrees. Three samples form the minimum number of data points into constructing a meaningful ordinary kriging-based surrogate model, which forms the case number 4 of table 5.2. Case number 5 of table 5.2 corresponds to using the multi-fidelity kriging with these samples and the full set of 3DPM data.

The lift curve from both the surrogate models show a good match with the reference curve as seen in figure 5.11. The same is the case with the drag polar seen in figure 5.12. From both these curves it can be seen that the surrogate model based on ordinary kriging already gives a desirable fit even without any leverage from the low-fidelity data. Further it is interesting to note that the surrogate model that was based on multi-fidelity kriging ends up having some error that is the result of leveraging information from the low fidelity method.The moment curves from both the surrogate model in figure 5.13 see a good fit with the reference curve which can be attributed to the sample lying at 12 degrees of angle of attack that proves to be favourable.

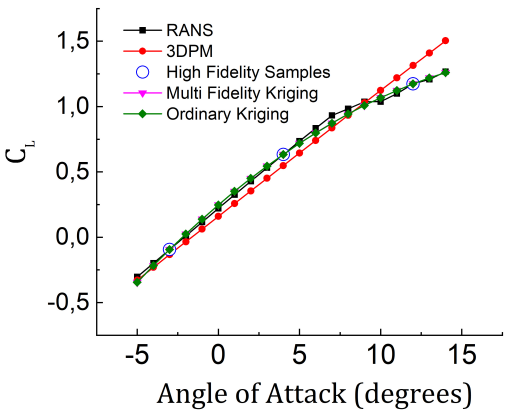

Figure 5.11: Multi-fidelity Lift Curve using three samples

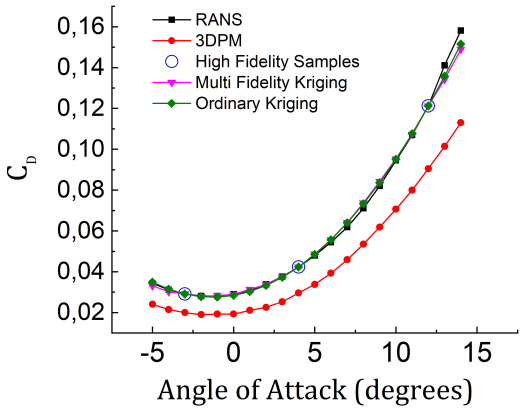

Figure 5.12: Multi-fidelity Drag Curve using three samples

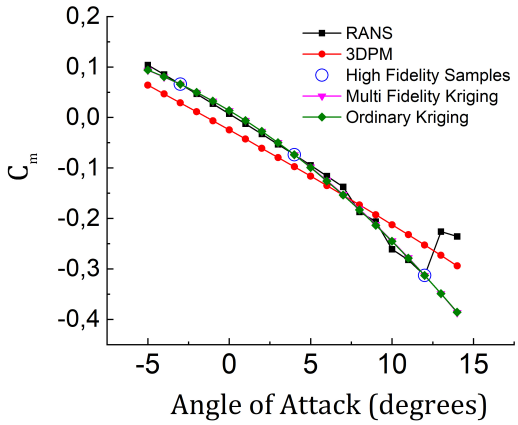

Figure 5.13: Multi-fidelity Moment Curve using three samples

5.2.4. CASE STUDY USING FOUR HIGH FIDELITY SAMPLES

This section discusses the results of the surrogate model with four samples, with the a sample not being located at a critical region. The results of this section belong to case number 6 and 7 of table 5.2, which are based on ordinary kriging and multi-fidelity kriging respectively. In these cases the four sample points lie at angles of attack of -5, 1 , 7 and 14 degrees.

Once again it can be seen from all the curves that ordinary kriging by itself gives a good estimate and leveraging the low fidelity data does not give any more benefit to the multi-fidelity kriging model. The errors due to over-scaling end up even more prominent at low angles of attack, as seen from the drag polar in figure 5.15. The lift curve based on the surrogate model show a very good fit at low angles of attack from -5 to 7 degrees (figure 5.14), where the separation is absent and at higher angles of attack it is still able to capture some of the non linear behaviour but not as good as the model with 3 samples (see figure 5.11). A similar trend is seen in the moment curve as seen in figure 5.16. The consequence of the absence of the sample point at 12 degrees can be clearly seen from these plots.

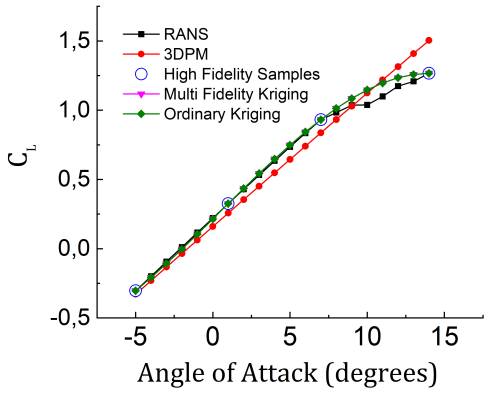

Figure 5.14: Multi-fidelity Lift Curve using four samples

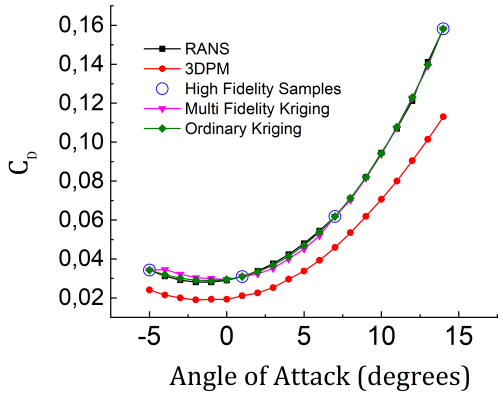

Figure 5.15: Multi-fidelity Drag Curve using four samples

From subsection 5.2.3 and 5.2.4, we see the performance of the ordinary kriging model is similar to that of the multi-fidelity kriging model. This implies that when there are sufficient high-fidelity samples, using a surrogate-based approach with ordinary kriging is viable. Using the 3DPM would be redundant. The multi-fidelity kriging model using the 3DPM and RANS sees a lot of value when ordinary kriging model cannot be constructed.

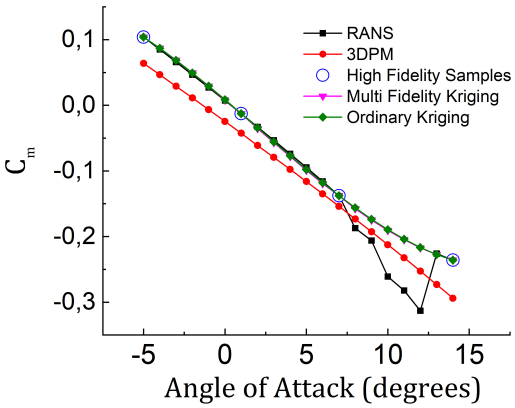

Figure 5.16: Multi-fidelity Moment Curve using four samples

5.2.5. CASE STUDY USING FIVE HIGH-FIDELITY SAMPLES

It is clear that the multi-fidelity approach is redundant when there is enough data to construct a surrogate model based on ordinary kriging. The 3DPM has a limitation of capturing the effects of separation, and at conceptual design stage this is already an interesting design point for investigation. Therefore, the case number 8 and 9 of table 5.2, were constructed using ordinary kriging and multi-fidelity kriging model respectively to see the efficacy of the surrogate model for learning the onset of separation. The 3DPM is usually run with steps of 1 degree Angle of Attack. Since this would be too dense of a data set, the high fidelity evaluations are done in steps of 5 degrees, which in this case, leads to a total of 5 samples. Note that the idea here is not to strictly use 5 samples, but utilize a surrogate-based approach with larger step sizes. Since the angle of attack spanned a range of 20, we get 5 samples.

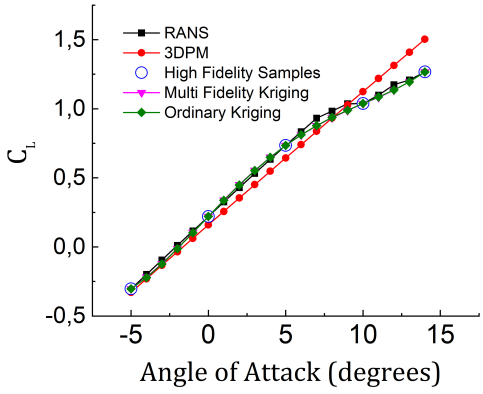

Figure 5.17: Multi-fidelity Lift Curve using five samples

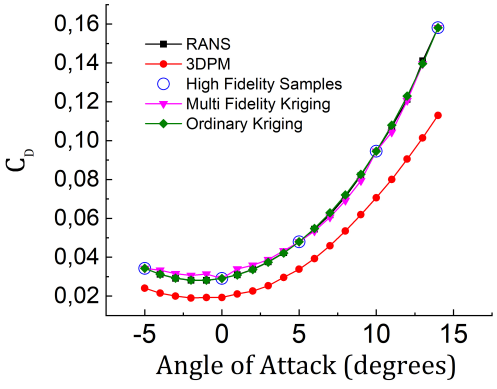

Figure 5.18: Multi-fidelity Drag Curve using five samples

The drag polar from the multi-fidelity method, as seen in figure 5.18 only introduces more errors trying to leverage low-fidelity data with sub-optimal scaling factor. Even though the lift curve in figure 5.17 predicts separation a little prematurely, it is still able to give better insights into this behaviour which would otherwise have not been possible with the previously used 3DPM. The moment curves in figure 5.19 also have a better fit at higher angles of attack showcasing the pitch break behaviour of the aircraft. Therefore the ordinary kriging-based surrogate model using RANS with larger angle of attack step sizes, can be a viable approach into learning the separation behaviour in the early stages of design.

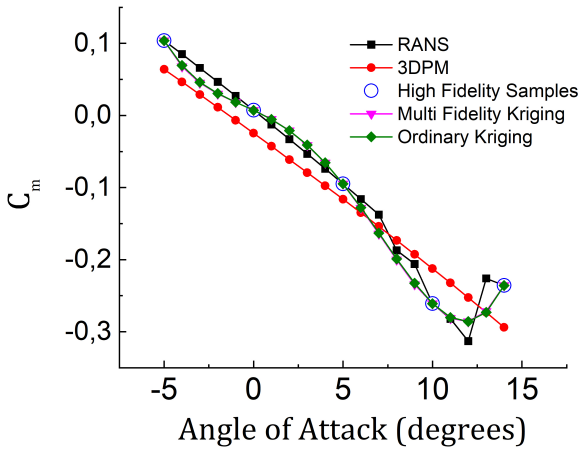

Figure 5.19: Multi-fidelity Moment Curve using five samples

5.2.6. ERROR METRICS FOR MULTI-FIDELITY STATIC CASES

The discussion thus far involved a qualitative take on the impact of the surrogate model with different sample sizes. The sample size of zero corresponds to the full set of 3DPM data. The error metrics are shown in figures 5.20, 5.21 and 5.22. The errors are quantified in termes of MAE and RMSE. It is important to note that the MAE is a metric that ends up being more lenient towards larger individual errors where as the RMSE is more penalizing.

The figure 5.20a shows the MAE in the lift coefficient curve while the figure 5.20b shows the corresponding RMSE. The MAE with one sample is still lesser than that of the 3DPM while the corresponding RMSE is higher. This doesn't necessarily mean that the model is poor. It is a result of some of the poor predictions being much poorer and this was clearly seen in figure 5.5 where the errors past 9 degrees angle of attack were much higher. The surrogate model with three samples that included a critical location had performed better than that with four as can be seen numerically from these graphs. The errors associated with the ordinary kriging as shown by the blue bar are almost equal to less than that of the multi-fidelity kriging models further supporting the redundancy of a multi-fidelity approach with 3DPM.

The MAE and RMSE in the drag coefficient are shown in figures 5.21a and 5.21b respectively. The drag polar saw the most benefit with multi-fidelity surrogate model. The errors that resulted from sub-optimal scaling of the low-fidelity results can be clearly seen in these graphs, where the errors associated with the multi-fidelity kriging are slightly higher than the corresponding ordinary kriging errors.

Figures 5.22a and 5.22b show the MAE and RMSE in the moment coefficient, which also show a similar behaviour as that of the metrics with the lift co-efficient. The 3DPM curve has under-prediction of the moments at low angles of attack and over-prediction at higher angles which leads it to have lower MAE. Despite a good fit at low angles of attack, the RMSE associated with that of the 3 samples are higher due to having larger errors at 13 and 14 degrees of angles of attack.

Looking at the error metrics across the various coefficients, it can be concluded that the multi-fidelity approach can be justified when the there are insufficient samples to run ordinary kriging-based surrogate model. Running an analysis with just the high fidelity method of RANS with ordinary kriging based surrogate model is a viable approach into investigation of separation during the early stages.

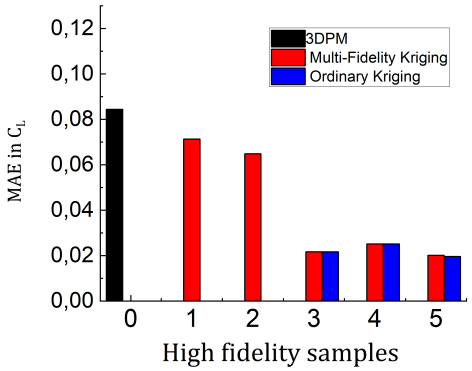

(a) MAE

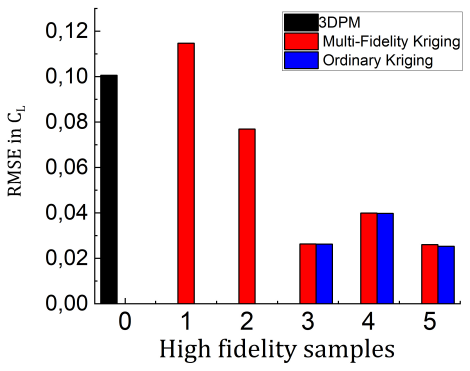

(b) RMSE

Figure 5.20: Errors in Lift coefficient

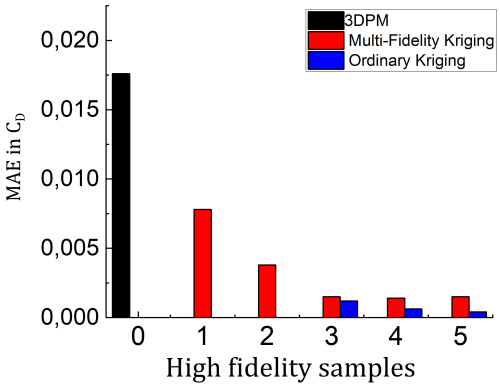

(a) MAE

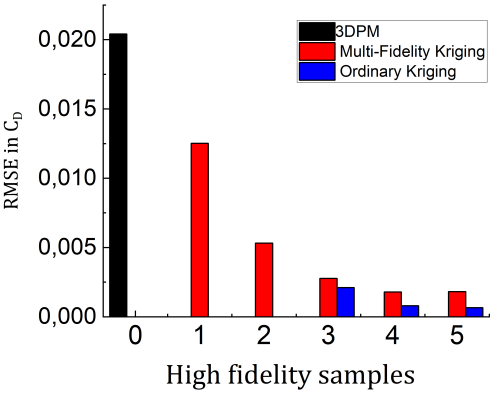

(b) RMSE

Figure 5.21: Errors in Drag coefficient

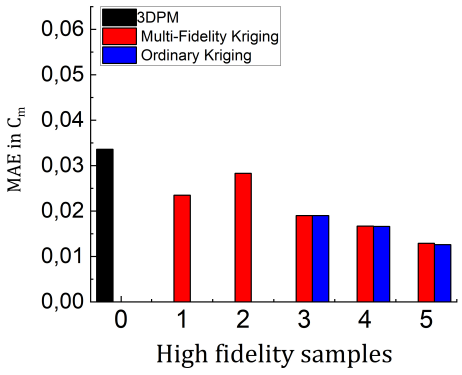

(a) MAE

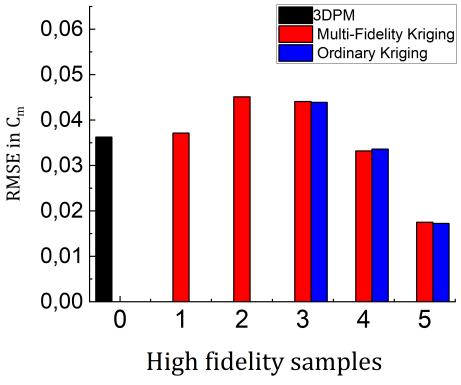

(b) RMSE

Figure 5.22: Errors in Moment coefficient

5.3. CASE STUDY FOR MULTI-FIDELITY DYNAMIC ANALYSIS

In this section, the dynamic derivative results obtained in the section 5.1.2 are used to study the effects of implementing the multi-fidelity surrogate model. The full set of RANS data serves as the reference. As discussed in section 5.1, instead of the dynamic derivatives themselves, the dynamic derivatives times the reduced frequency is data that would be predicted.

Unlike the steady-state simulation, the computational time for a transient simulation depends on the size of the time step and the number of time steps that are considered. If one requires to preserve a similar resolution of the solution by having similar time step sizes across the reduced frequencies, then consequently the number of time steps that are needed increases as the reduced frequency decreases. This results in the lower reduced frequency solutions costing higher computational time. A multi-fidelity model using a single sample at various frequencies are studied and shown in subsection 5.3.1. The subsection 5.3.2 shows the outcome of surrogate model with two samples. The table 5.3 shows the various surrogate models that were studied.

Case Number	Description	Computational Time (hrs)	Discussed in
1	Single-Fidelity 3DPM	0.2	All
2	Multi-fidelity kriging with a sample at highest reduced frequency	21.37	5.3.1
3	Multi-fidelity kriging with a sample at median	43.03	5.3.1
4	Multi-fidelity kriging with a sample at lowest reduced frequency	55.86	5.3.1
5	Multi-fidelity kriging with two samples	77.03	5.3.2
6	Ordinary Kriging with two samples	76.86	5.3.2

Table 5.3: Surrogate Model used for dynamic analysis

5.3.1. CASE STUDY USING ONE HIGH-FIDELITY SAMPLE

The figure 5.23 shows the results of the multi-fidelity kriging model with a single sample at the highest reduced frequency of k=0.05, which forms the case number 2 of table 5.3 of this study. Using a sample at such a point comes at a relatively lower computational time compared to lower reduced frequencies. The dynamic derivatives for the normal force coefficient in figure 5.23a shows a drop in accuracy of the predicted values as the the frequency reduces, which is a consequence of the data lying further away from the known sample point. The dynamic derivatives for the moment coefficient also show a similar behaviour as seen in figure 5.23b.

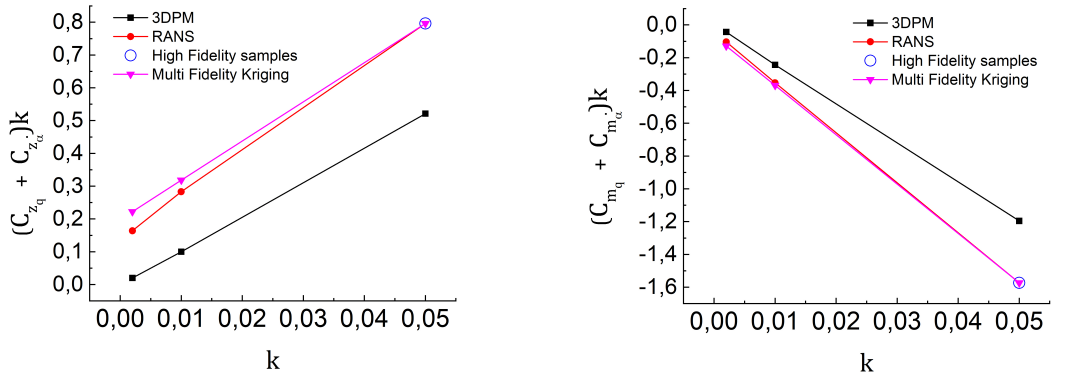

(a) Normal force coefficient dynamic derivative vs reduced frequency

(b) Moment coefficient dynamic derivative vs reduced frequency

Figure 5.23: Multi-fidelity model with single sample at k=0.05

The reduced frequency of k=0.01 is the median of the range considered in this study and the figure 5.24 shows the results of the multi-fidelity surrogate model with a sample considered at this location. This is the case number 3 of table 5.3 of this study. As compared to the previous case number 2, this case shows better prediction accuracy at the lowest frequency for the dynamic derivative of the normal force coefficient as seen in figure 5.24. The predicted value at this highest frequency has more error since the sample that is chosen is located much closer to lowest frequency in the range of frequencies considered for the study. This is clearly seen from the figure 5.24b which shows the surrogate model results for the dynamic derivatives of moment coefficient.

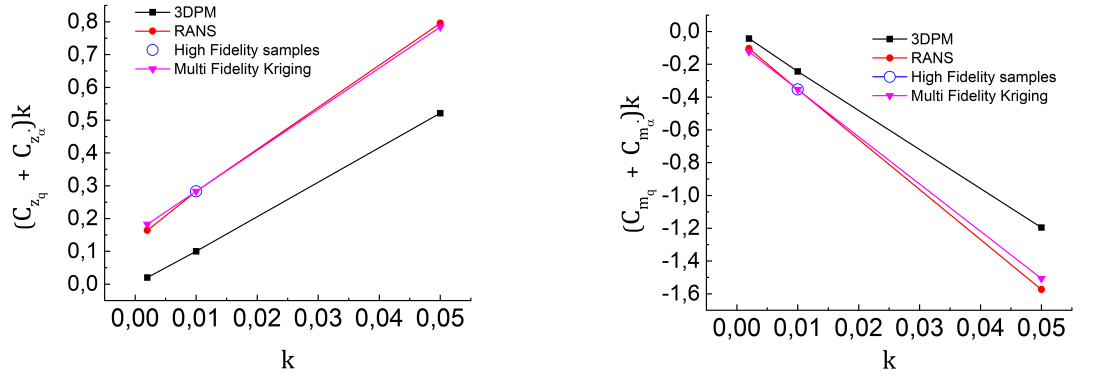

(a) Normal force coefficient dynamic derivative vs reduced frequency

(b) Moment coefficient dynamic derivative vs reduced frequency

Figure 5.24: Multi-fidelity model with single sample at k=0.01

The case number 4 of table 5.3 of this study, uses a single high-fidelity sample at the least reduced frequency of k=0.002 and the results are shown in figure 5.25. The behaviour is similar to that of the case number 2 but the prediction errors in this case get larger with increasing reduced frequency. The dynamic derivatives for the normal coefficient as seen in figure 5.25a show a better fit than the corresponding predictions of case number 2 as seen in figure 5.23a but it is also important to note that case number 3 roughly takes 2.5 times more computational time than case number 2.

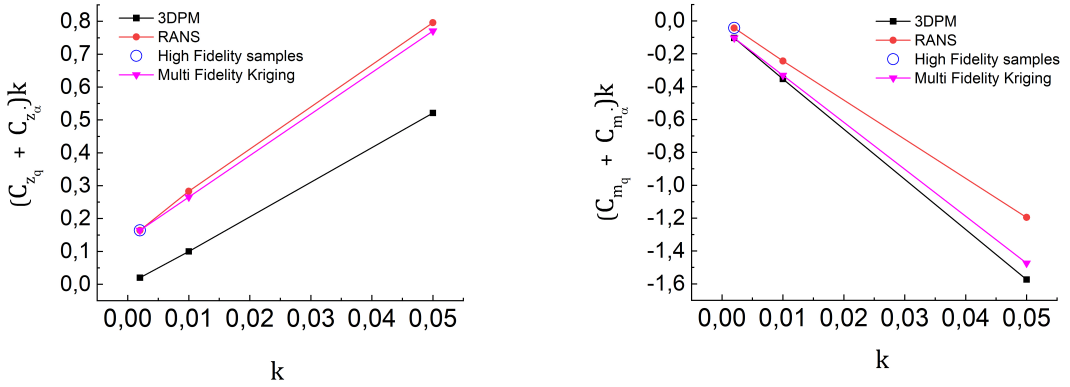

(a) Normal force coefficient dynamic derivative vs reduced frequency

(b) Moment coefficient dynamic derivative vs reduced frequency

Figure 5.25: Multi-fidelity model with single sample at k=0.002

5.3.2. CASE STUDY USING TWO HIGH-FIDELITY SAMPLES

The case number 5 and 6 of table 5.3, are surrogate models that are constructed with two high-fidelity samples. The case number 5 is a surrogate model based on multi-fidelity kriging while the case number 6 uses ordinary kriging. Strictly speaking, two points are insufficient data to construct ordinary kriging model since all it does is make a linear interpolation. Since the data themselves show a fairly linear trend in the range of reduced frequency, the model is just constructed to compare the corresponding multi-fidelity results. The

results are shown in figure 5.26 and it can be seen that there are no significant differences between the multi-fidelity kriging and ordinary kriging. It is important to take note that this conclusion is only valid due the the already linear behaviour of the dynamic data.

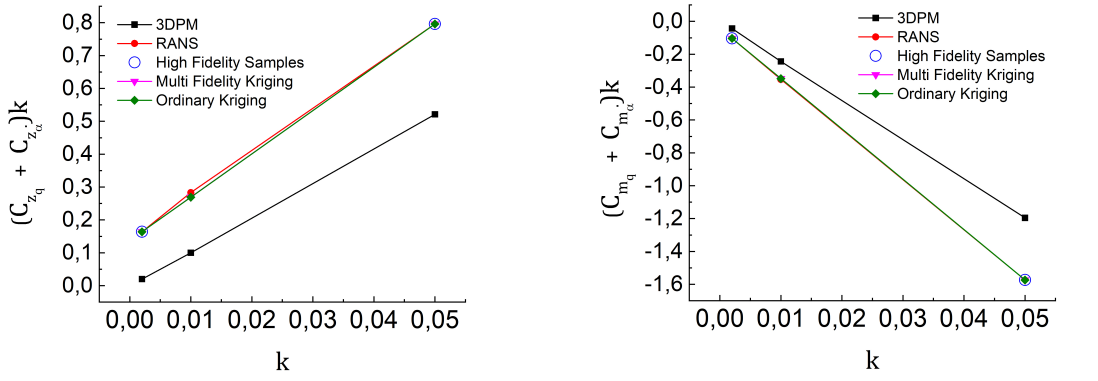

(a) Normal force coefficient dynamic derivative vs reduced frequency

(b) Moment coefficient dynamic derivative vs reduced frequency

Figure 5.26: Multi-fidelity model with two samples

5.3.3. ERROR METRICS FOR MULTI-FIDELITY DYNAMIC CASES

The errors for the various surrogate models are quantified in terms of the MAE and the RMSE and have been shown in figure 5.27. The figure 5.27a shows the corresponding errors in the dynamic derivative for the normal force coefficient. The 3DPM with a MAE of 0.2 already roughly corresponds to a mean relative error of about 40%. The case number 2 which uses a single sample at the highest frequency already has MAE about 0.03. The accuracy is already improved by 85% on an average by using just a single high fidelity sample. The errors are practically negligible while using a surrogate model with two samples. The improvement in accuracy corresponding to these models are 98%. In the case of dynamic derivatives for moments as seen figure 5.27b, the accuracy is improved by 92% using the sample at the highest reduced frequency. The case number four which has the highest average errors also sees a 78% improvement in accuracy compared to that of the 3DPM.

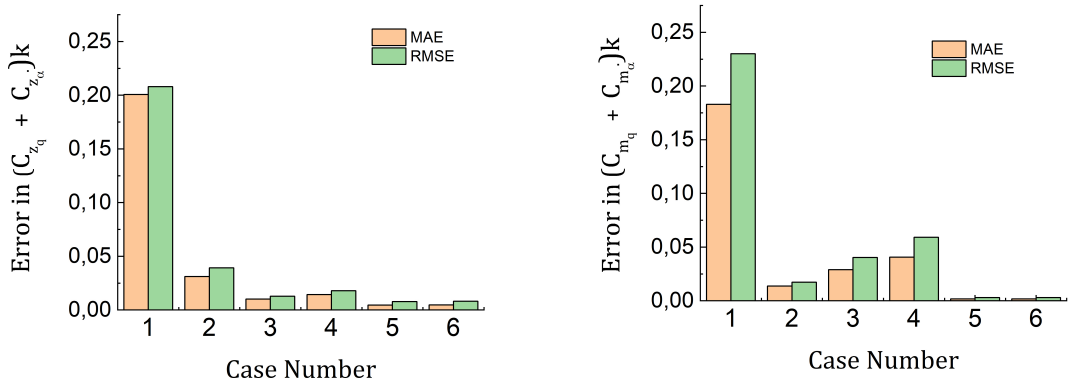

(a) Errors in Normal Force coefficient dynamic derivative

(b) Errors in Moment coefficient dynamic derivative

Figure 5.27: Errors in dynamic derivatives

5.4. TIME STUDY

In this section, a time study is conducted for all the previously constructed surrogate models. The study will only compare the time required in solving and not the pre-processing time. The post-processing to obtain the dynamic derivatives in the case of RANS involves solving the Inverse Fourier Transforms. This is in the order of milliseconds and when compared to the time taken by the solution, it is negligible. The surrogate model also experiences a similar computational time that is in the order of milliseconds. The simulations are carried out using a computer with 20 cores running in parallel, the specification of which were highlighted in chapter 2 in table 2.1. The time discussed in this section refers to the wall time which is the real time consumed by running all the 20 cores in parallel.

5.4.1. TIME STUDY FOR MULTI-FIDELITY STATIC ANALYSIS

The feasibility of the surrogate model for the static analysis are assessed in terms of RMSE and the computational time and is shown in figure 5.28. The description for each case can be found in table 5.2. The case number 1 corresponds to the full set of the 3DPM results. A single case of the 3DPM for the static analysis roughly takes 4 minutes which leads to a total computational time of 1.3 hours for a total of 20 angles of attack that were considered. A single case of RANS takes roughly 2 hours to solve which is 30 times the cost of the 3DPM for a given angle of attack. Despite the 3DPM being able to capture the trend, it has RMSE of 200 drag counts which roughly correspond to 50% error in the computation of drag, compared to that of the high-fidelity RANS method.

The multi fidelity surrogate model with just one single sample as represented by case number 2 has a RMSE of 125 drag counts. It is important to note that the metric of RMSE heavily penalizes larger errors in the prediction , and despite this behaviour the accuracy of the 3DPM is improved by 37.5% by the multi-fidelity approach. This however leads to a total computational time that is roughly twice as high as running the 3DPM alone. The case number 3 which uses two samples is able to improve the accuracy by 75% with a RMSE of 50 drag counts.

The case number 4 and onwards have sufficient samples to construct ordinary kriging based surrogate model and it can be seen that in all such cases the errors related to that of the ordinary kriging model is similar to that of the multi-fidelity kriging model for a given number of samples. The surrogate model with 3 samples corresponding to case number 4 already shows 86% improvement in accuracy with RMSE of 28 drag counts, and the increase in accuracy up to 96% with a RMSE of 8 drag counts with four samples does not justify the 33% increase in computational time.

The case number 8 utilises the ordinary kriging-based surrogate model with angle of attacks steps of 5 degrees instead of 1 degree as typically used. This case highlights the benefits of using a single-fidelity surrogate model that uses a high-fidelity method like RANS but with larger steps. Despite the RANS method costing 30 times the computational as that of the 3DPM for a given angle of attack, the overall computational time is only 8 times that of the 3DPM. This roughly saves 73% of the computational time as compared to simulating for steps of 1 degree and only comes with a compromise of RMSE of 6 drag counts. Therefore, if a sub-scale flight test engineer wants to opt for a high-fidelity method then the use of ordinary kriging with larger steps of angles of attack is viable process.

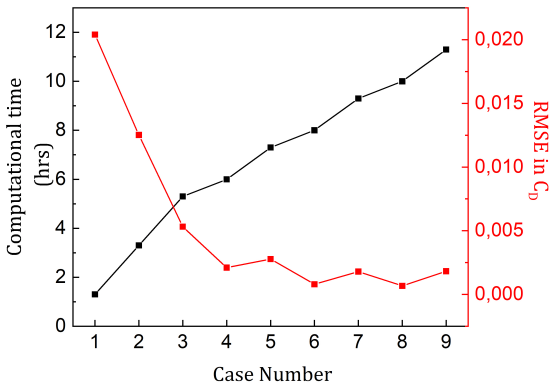

Figure 5.28: Time study for static analysis

5.4.2. TIME STUDY FOR MULTI-FIDELITY DYNAMIC ANALYSIS

In the case of computation of dynamic derivatives, the simulations were carried out for 3 different reduced frequencies and the feasibility of the various surrogate models are assessed in this section. The description of the various cases can be found in table 5.3. Practically, the quasi-steady formulations for the dynamic simulation follow a similar solution to that of the static cases and therefore also have a computational time of 4 minutes for a given angle of attack at given reduced frequency. Whereas the fully unsteady transient formulation with the RANS method requires the solution to the steady-state equation which is the initial state for the dynamic case. The computational time then depends on the number of time steps that are solved for a given case. For similar resolution of the solution, more time steps are required at lower reduced frequencies and the corresponding computational time is much larger.

The computational time for the dynamic case with a reduced frequency of k=0.05 is roughly 21 hours which is about 320 times the cost of the quasi-steady 3DPM. The computational costs for dynamic simulation at low frequency is about 3 times as high as that of the high frequency which would roughly be 900 times that of the 3DPM. To put things more into perspective, a single case of dynamic simulation at high frequency, costs twice as that of the obtaining the static data using RANS method. Trying to obtain dynamic derivatives across all the reduced frequencies is simply not feasible during the early stages. But on the other hand, the 3DPM has very poor accuracy that it will cause an issue in the evaluation of sub-scale flight test model designs.

The figure 5.29 shows the computational time and the RMSE associated with the dynamic derivatives of the moment coefficient with the various surrogate models. The case number 2 which utilizes a high-fidelity RANS sample at k=0.05 already shows significant reduction in the RMSE. This is mainly due to the fact that the sample is chosen at the highest frequency where the absolute errors are usually the largest. This exploit allows the surrogate model to leverage the low-fidelity data and have accuracy improvement of 92% . This is already a satisfactory improvement and simulating with more samples is not optimal considering the excess computational time involved. This multi-fidelity surrogate model with one sample at the highest frequency roughly takes 21 hours which is still 105 times cost of of the full set of the 3DPM data that roughly takes 12 minutes. But the improvement in accuracy brought about, justifies the use multi-fidelity approach in assessment of SFT model design. Moreover, using just RANS to obtain the dynamic results with higher accuracy would have led to the computational time being roughly 5 times as large.

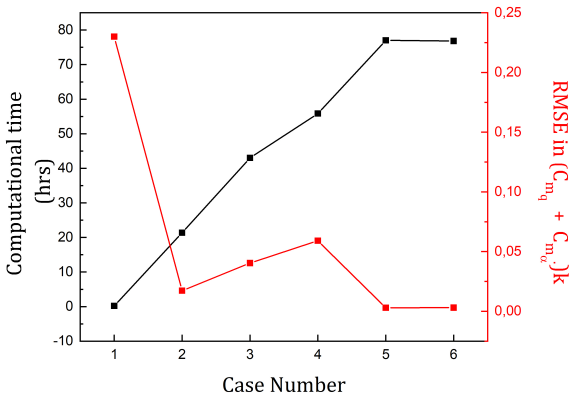

Figure 5.29: Time study for dynamic analysis

5.5. SUMMARY

In section 5.1, the error of the low-fidelity method relative to the high-fidelity method was quantified. Compared to the high-fidelity RANS method, the 3DPM roughly has 35% error in the prediction of the normal force coefficient dynamic derivative and about 20% in the case of the dynamic derivatives for moment coefficient. With this, the first sub-question mentioned at the beginning of this chapter has been answered.

The sections 5.2 and 5.3 showed the accuracy of the various surrogate models. Multi-fidelity kriging model which utilizes two RANS samples, has a RMSE of 50 drag counts. Compared to the single-fidelity 3DPM with RMSE of 200 drag counts, this is a 75% improvement in accuracy. Accuracy improvement of 86% (RMSE of 28 drag counts) could be achieved with utilizing three RANS samples, but a similar accuracy is achieved by ordinary krigng with the same set of RANS samples. This makes the use of 3DPM totally redundant. 3DPM used in the research, is fundamentally incapable of capturing effects of separation. The 3DPM therefore, can no longer provide any meaningful leverage. This results in the ordinary kriging model being just as good as the multi-fidelity kriging model. The multi-fidelity kriging model only has value, when there are insufficient samples to create ordinary kriging model. The multi-fidelity model is especially valuable when it comes to prediction of dynamic derivative. Using just a single high-fidelity sample, accuracy improvement of 92% could be achieved. Compared to running a single-fidelity RANS, this multi-fidelity approach can achieve almost the same accuracy for one-fifth the computational cost, as seen in section 5.4.

To conclude, the multi-fidelity kriging model can be used to predict the dynamic derivatives with using just one RANS evaluation. The evaluation is optimal at the highest frequency, since the computational time increases as the frequency of the oscillation is reduced. When it comes to the static analysis, the multi-fidelity analysis sees some benefit with a single sample or two samples. For sample sizes where ordinary kriging can be constructed, the multi-fidelity approach becomes redundant. The table 5.4, highlights the preferred surrogate-based approach for generating the aerodynamic database.

Type of analysis	**Accuracy improvement**	**Surrogate model to be used**
Static	40-70%	Multi-fidelity kriging with two samples
Static	>90%	Ordinary kriging
Dynamic	>90%	Multi-fidelity kriging with one sample

Table 5.4: Choice of surrogate model

6

Conclusion and Recommendation

6.1. Conclusion

Sub-scale Flight Test (SFT) can be an effective method to learn the flight behaviour of novel aircraft designs. There needs to be similitude between the sub-scale model used in SFT and the full-scale prototype of the novel design, for the method to provide valuable information. SFT models designed based on classical similitude theory are often simplistic and similitude is not established. The method of computational scaling is state-of-the-art for designing SFT models. Computational scaling method iteratively uses computational analysis to propose designs which have the best similarity to full-scale aircraft.

Previous research into SFT model design by Raju Kulkarni, quantified the differences between designing SFT model using classical similitude theory and that by computational scaling approach[18]. The research introduced a novel figure of merit called **Degree of Similitude (DoS)**, which would quantify the similitude between SFT model and the full-scale prototype. It demonstrated the significant benefits of utilizing the computational scaling approach over the classical similitude theory, into designing SFT models.

The evaluation of DoS often requires a comprehensive aerodynamic database. Computational methods used for aerodynamic data generation are labour and time intensive, which make them a critical bottleneck in computational scaling approach. The 3D-Panel Method(3DPM) was used in the generation of aerodynamic database in the previous research. In the field of Computational Fluid Dynamics(CFD), this is regarded as a low-fidelity method, which can give quick evaluations, but also has low accuracy. Using methods of higher fidelity such as Reynolds Averaged Naiver Stokes (RANS) or Large Eddy Simulation (LES) were deemed to make the process infeasible. This is because these methods can take from days to weeks to evaluate a single design, let alone an iterative computational scalling approach. Therefore, the main aim of this research was to support the SFT designs using computational scaling, by developing a multi-fidelity approach for the generation of aerodynamic database that is required in the evaluation of DoS. This can be achieved by finding the answer to the follwing research question :

What is the impact of utilizing a multi-fidelity approach in the generation of aerodynamic database for SFT model design, compared to the classical single-fidelity methods?

The 3DPM ignores the effects of viscosity,leads to poor predictions of drag characteristic and fails to predict the effects of stall. The method uses a quasi-steady formulation to simulate the dynamic behaviour of the aircraft. Based on the study performed in this thesis, dynamic derivatives obtained from 3DPM are insensitive to the input changes of reduced frequency. Spallart-Allmaras(SA) is a one equation RANS model, and is used as the high-fidelity method. This is a high-fidelity method that includes the effects of viscosity and is able to carry out fully unsteady simulation. Compared to other CFD methods such as two equation RANS models or LES, SA-RANS requires lower computational time. This made it the optimal choice to be used in the multi-fidelity process.

Since RANS is slow and 3DPM is fast, multi-fidelity approach was used to combine the two methods to improve the speed of aerodynamic data generation without significantly lowering the accuracy. Fusion-based model management strategy was utilized for the multi-fidelity approach. Co-kriging was used to fuse the low and high fidelity data. This is the multi-fidelity kriging based surrogate model, developed in this research.

To prove the effectiveness of the proposed method, computational analysis was performed on the Variable Geometry Model(VGM), which is a 8.8% geometrically scaled model of a Cessna Citation II 550. The computational time of the multi-fidelity process would be directly affected by that of the high-fidelity method. A study was performed to find the optimal size of the grid and time step (see chapter 4.1). Using these optimal sizes, solving a single static case using RANS takes 2 hours of computational wall-time. A total of 21 hours is required for a single dynamic simulation. The 3DPM takes 4 minutes for both static and dynamic simulation.

In this research, the data set for the static analysis consists of 20 evaluations and 3 evaluations in the case of dynamic analysis. The multi-fidelity model uses the full set of data from the 3DPM and some sample points from the high-fidelity data set. The errors are computed relative to the full set of RANS data. In a multi-fidelity surrogate model, the low-fidelity function provides a leverage while predicting the high-fidelity output. A surrogate model based on ordinary kriging is created that serves as a secondary reference. This single-fidelity surrogate model utilizes only the samples from high-fidelity data set. Comparing the multi-fidelity surrogate model to ordinary kriging surrogate model, showcases the leverage provided by 3DPM.

In the case of static simulation, the 3DPM had a Root Mean Square Error (RMSE) of 200 drag counts compared to that of RANS. This RMSE was reduced to 50 drag counts using the multi-fidelity model with two high-fidelity samples. This corresponds to an improvement in accuracy by 75%. Increasing the number of high fidelity samples helps reduce the errors further. Whenever there are enough samples in constructing a ordinary kriging model, the performance of the single-fidelity surrogate model is almost the same as that of the multi-fidelity surrogate model. Therefore, using 3DPM to provide leverage in such a case, would be redundant.

The computational time of the dynamic simulation increases with decrease in reduced frequency of a flow. It took 20 hours for a dynamic simulation at high frequency while the set of three evaluation approximately takes 100 hours. Using the multi-fidelity approach with a single sample at the highest reduced frequency, an accuracy improvement of 92% was obtained. Therefore, compared to using a single-fidelity RANS, the multi-fidelity approach develop in this research, can generate the database in 20% of the computational time.

The multi-fidelity kriging model developed using RANS and 3DPM, is capable of generating the aerodynamic database that has reasonable accuracy and computational cost. This helps solve the bottle neck in the computational scaling approach, making it feasible approach for design of SFT models. These SFT models with well established similitude, will help us learn the behaviour of the novel designs and get a step closer towards sustainable aviation.

6.2. RECOMMENDATION

This section provides recommendation to broaden the scope/applicability of this research.

- KBE tools like MMG has the potential to automate the generation of high quality structured meshes. Using structured meshes in the aerodynamic analysis would further help reduce the computational cost of the high-fidelity method. The reduction in cost of high-fidelity analysis reduce the overall costs of generating the aerodynamic database using the multi-fidelity approach
- RANS method is able to both capture viscous effects and simulate a fully unsteady case for the computation of the dynamic derivatives. Euler method can be used to compute a fully unsteady case but it would ignore the effects of viscosity. If the viscous effects are not deemed to be important while studying certain dynamic motions, then RANS can be replaced by Euler method. Using Euler method as the high-fidelity method and 3DPM as the low-fidelity method, would bring down the costs of the multi-fidelity approach.
- In this study the combined derivatives were not separated because the low fidelity method does not have a means to do so. But future research can also include the plunging motion in order to separate the derivatives. Furthermore, the motion can be carried out across all axis instead of just the longitudinal motion considered in this study and for wider range of flow parameters.
- The scaling factor ζ, for the multi-fidelity method using the 3DPM and RANS was assumed to be constant in this research. A research that studies modeling the scaling factor for multi-fidelity kriging between the 3DPM and the RANS would useful to this approach. The method of computational scaling would assess wide range of SFT model designs. It could potentially be worth the time to use one of those designs to model the scaling factor between the two computational methods. Once modeled, it can be used to in the multi-fidelity approach of successive designs to obtain better accuracy.

A

KRIGING AND CO-KRIGING

The unknown value $Y(X_0)$ of a random function Y, can be constructed as a linear combination of the known values[33]. This is represented in the equation A.1 where μ is the known stationary mean and λ is the set of weights. This equation can be rewritten by considering the residuals about the mean value and is shown in A.2.

$$Y(X_0) = \sum_{i=1}^{n} \lambda_i Y(X_i) + \left(1 - \sum_{i=1}^{n} \lambda_i\right)\mu \tag{A.1}$$

$$Z(X_0) = \sum_{i=1}^{n} \lambda_i Z(X_i) \tag{A.2}$$

The weights are found such that the variance of the prediction is minimized. The variance is the expectation of the difference between the predicted value and the true but unknown value (Z^*). This is shown in equation A.3. Using equation A.2, we obtain the following expansion as shown in equation A.4. The expectation can be written as co-variances between the data and this equation A.5 shows this.

$$E\{[Z^*(X_0) - Z(X_0)]^2\} \tag{A.3}$$

$$\sum_{i=1}^{n}\sum_{j=1}^{n} \lambda_i\lambda_j E\{Z(X_i)Z(X_j)\} - 2\sum_{i=1}^{n} \lambda_i E\{Z(X_i)Z(X_0)\} + E\{[Z^*(X_0)^2]\} \tag{A.4}$$

$$\sum_{i=1}^{n}\sum_{j=1}^{n} \lambda_i\lambda_j Cov(Z(X_i), Z(X_j)) - 2\sum_{i=1}^{n} \lambda_i Cov(Z(X_i), Z(X_0)) + Cov(0) \tag{A.5}$$

The covariance between two points are obtained from the correlations ψ between the random variable function.This is shown in equation A.6. Also $Cov(0) = \sigma^2$ which is the total variance in the set of data. Since we need the weights that minimize equation A.5, we can obtain them by differentiating this with respect to the weight which then enables to solve the set of equations shown in equation A.7.

$$Cov(Z(X_i), Z(X_j)) = \sigma^2\psi(X_i, X_j) \tag{A.6}$$

$$\sum_{i=1}^{n} \lambda_j Cov(Z(X_i), Z(X_j)) = Cov(Z(X_j), Z(X_0)) \quad where \quad j = 1,2....n \tag{A.7}$$

This set of equations assumed the stationary mean to be known prior to solving and this method is called **simple kriging** If the the constraint of $\sum_{i=1}^{n} \lambda_i = 1$ is added within the set of equations this results in the solution that computes the local mean. Adding such a constraint alleviates the need to know the mean and this method is referred to as **ordinary kriging**. The predictor variance can be computed using the equation A.8.

$$Variance(X_0) = Cov(0) - \sum_{i=1}^{n} \lambda_i Cov(Z(X_i), Z(X_0)) \tag{A.8}$$

Equation A.8 only depends on the covariance matrix which as seen in equation A.6 only depends on the distribution of the data and not the data values at a given location. This property of being able to evaluate the prediction variance irrespective of the predicted value is called **homoscedastic property**.

The multi-fidelity kriging or co-kriging, predicts the high-fidelity values of the function $Z_h(X)$ as a scaled value of a low-fidelity function $Z_l(X)$ and a discrepancy function $Z_d(X)$ which is a Gaussian random function [34]. This is shown in equation A.9 where ζ is the scaling factor.

$$Z_h(X) = \zeta Z_l(X) + Z_d(X) \tag{A.9}$$

The covariance matrix evaluation in the previous case only involved a single random function whereas there are three matrices that correlate the two fidelity levels involved. The set of extra covariance matrix definitions are shown in equation A.10. Furthermore, the constraint equation in this case contains the weights to the high-fidelity data $\sum_{i=1}^{n} \lambda_i^h = 1$ and the low-fidelity data $\sum_{i=1}^{m} \lambda_i^l = 0$

$$\begin{aligned} Cov(Z_l(X), Z_l(X)) &= \sigma_l^2 \psi_l(X_l, X_l) \\ Cov(Z_h(X), Z_l(X)) &= \rho \sigma_l^2 \psi_l(X_l, X_h) \\ Cov(Z_h(X), Z_h(X)) &= \rho^2 \sigma_l^2 \psi_l(X_l, X_l) + \sigma_d^2 \psi_d(X_d, X_d) \end{aligned} \tag{A.10}$$

By solving the modified matrices, one can obtain the multi-fidelity kriging prediction.

B

HYSTERESIS CURVES FOR VGM

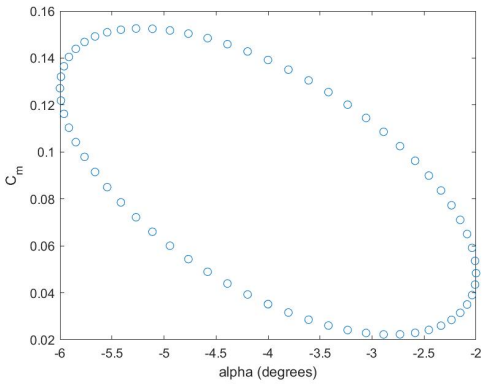

(a) Moment coefficient vs Angle of Attack

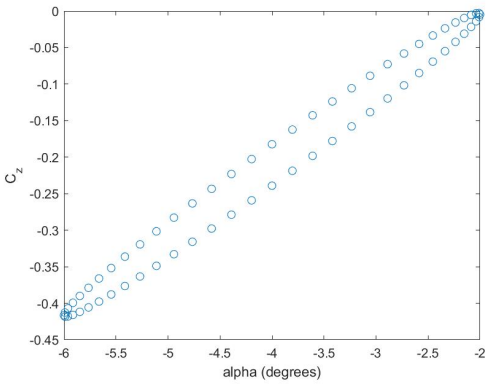

(b) Normal Force coefficient vs Angle of Attack

Figure B.1: Hysteresis curves for AoA -4 degrees

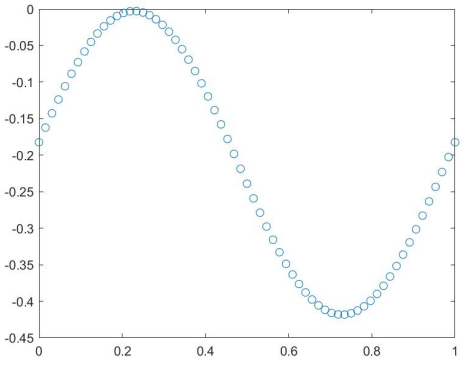

(a) Moment coefficient vs Normalized time

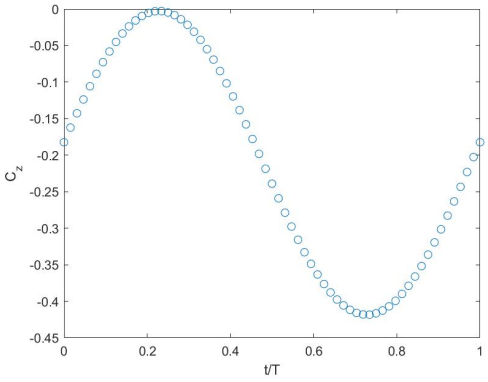

(b) Normal Force coefficient vs Normalized time

Figure B.2: Time Domain curves for AoA -4 degrees

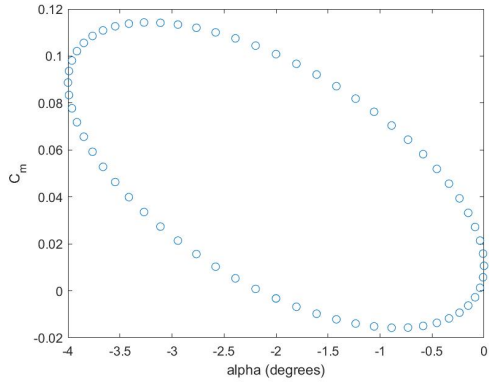

(a) Moment coefficient vs Normalized time

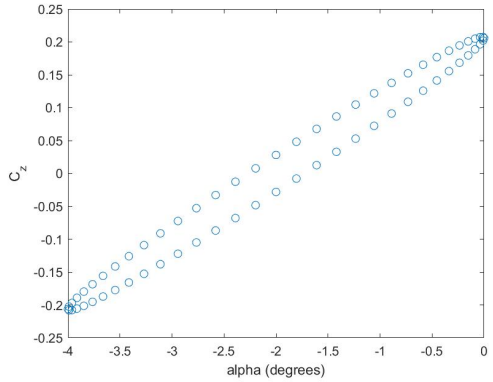

(b) Normal Force coefficient vs Angle of Attack

Figure B.3: Hysteresis curves for AoA -2 degrees

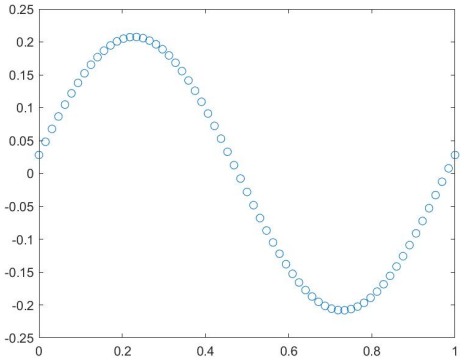

(a) Moment coefficient vs Normalized time

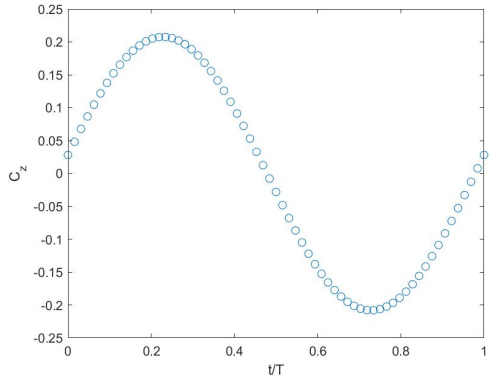

(b) Time Domain curves for AoA -2 degrees

Figure B.4: Force and moment Hysteresis for harmonic pitch of NACA0012 airfoil

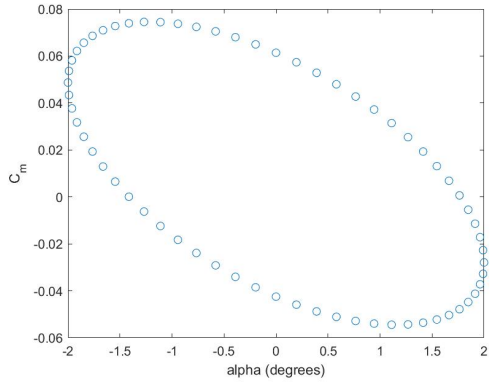

(a) Moment coefficient vs Angle of Attack

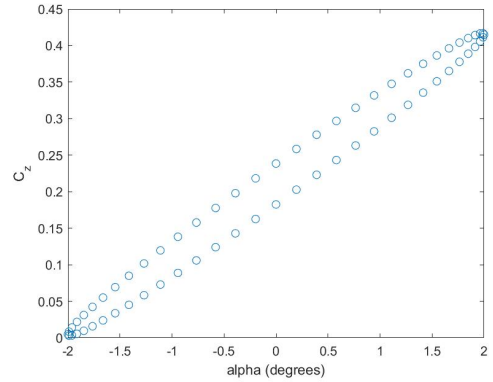

(b) Normal Force coefficient vs Angle of Attack

Figure B.5: Hysteresis curves for AoA -0 degrees

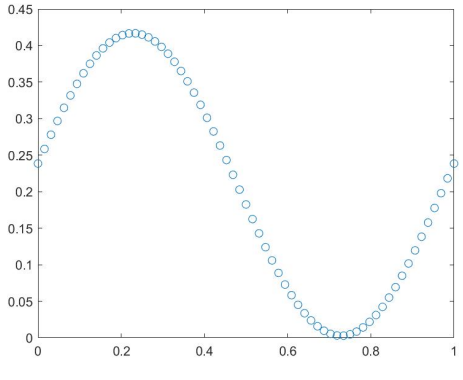

(a) Moment coefficient vs Normalized time

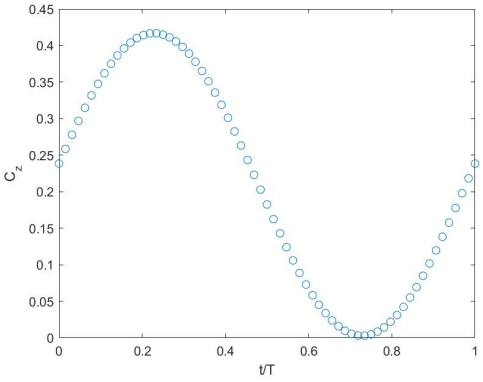

(b) Normal Force coefficient vs Normalized time

Figure B.6: Time Domain curves for AoA 0 degrees

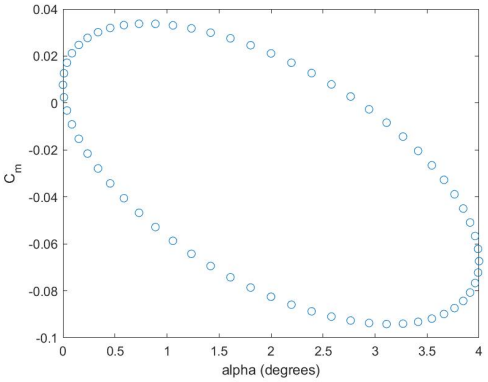

(a) Moment coefficient vs Angle of Attack

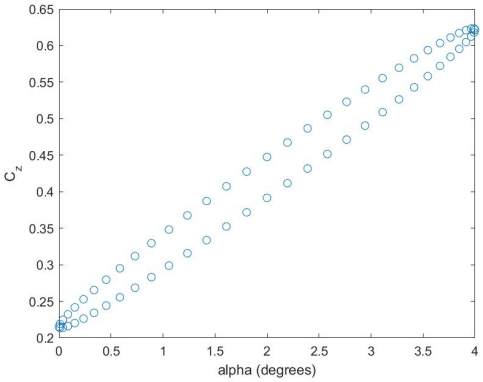

(b) Normal Force coefficient vs Angle of Attack

Figure B.7: Hysteresis curves for AoA 2 degrees

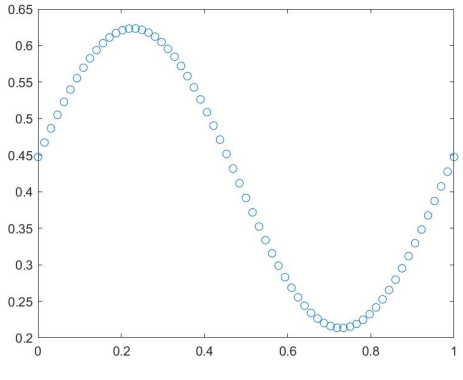

(a) Moment coefficient vs Normalized time

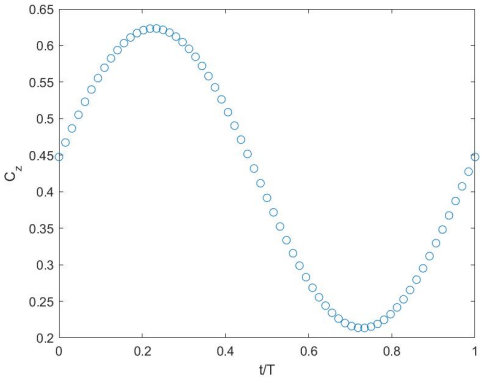

(b) Normal Force coefficient vs Normalized time

Figure B.8: Time Domain curves for AoA 2 degrees

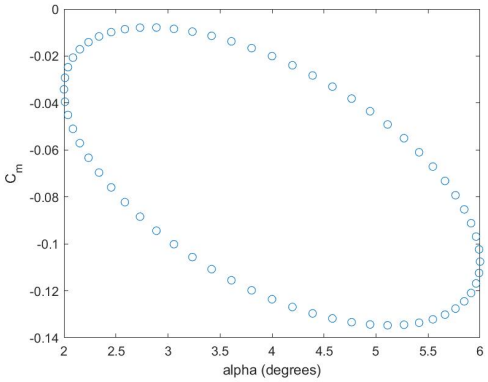

(a) Moment coefficient vs Angle of Attack

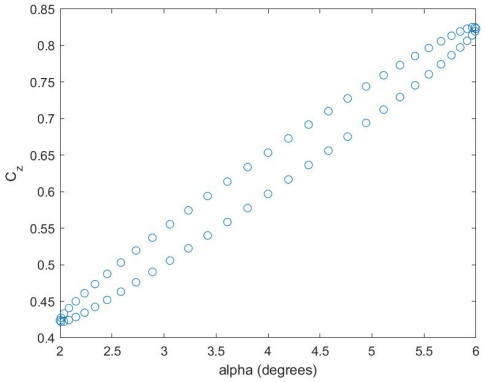

(b) Normal Force coefficient vs Angle of Attack

Figure B.9: Hysteresis curves for AoA 4 degrees

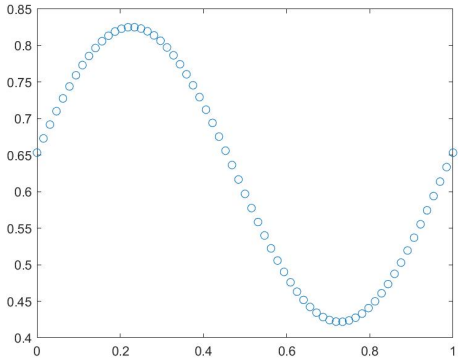

(a) Moment coefficient vs Normalized time

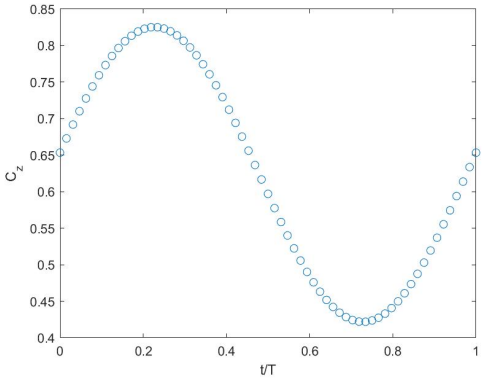

(b) Normal Force coefficient vs Normalized time

Figure B.10: Time Domain curves for AoA 4 degrees

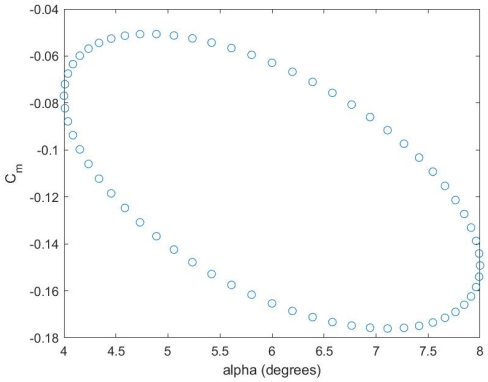

(a) Moment coefficient vs Angle of Attack

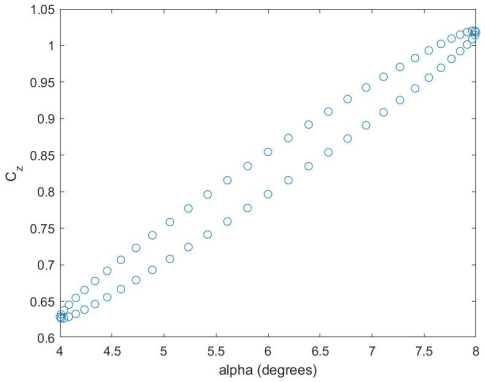

(b) Normal Force coefficient vs Angle of Attack

Figure B.11: Hysteresis curves for AoA 6 degrees

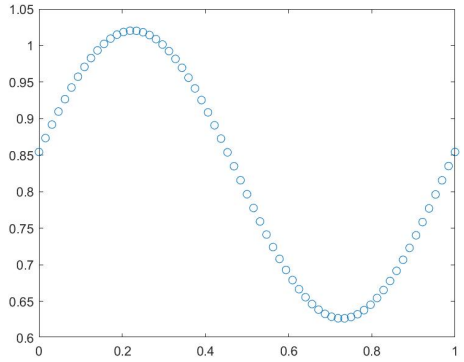

(a) Moment coefficient vs Normalized time

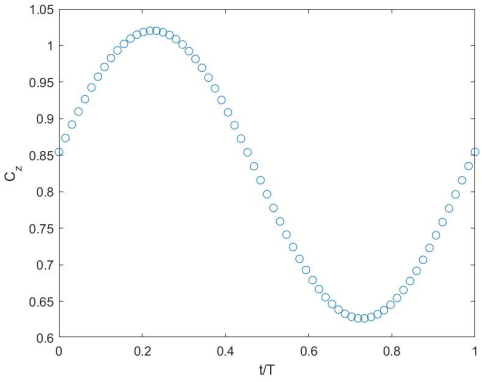

(b) Normal Force coefficient vs Normalized time

Figure B.12: Time Domain curves for AoA 6 degrees

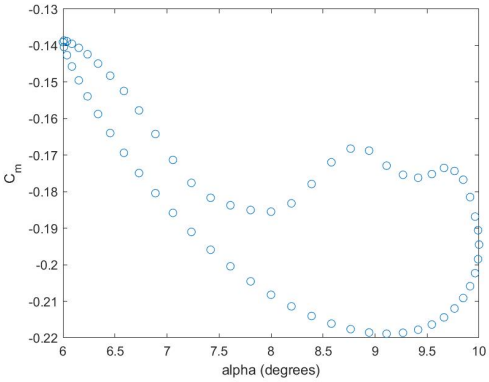

(a) Moment coefficient vs Angle of Attack

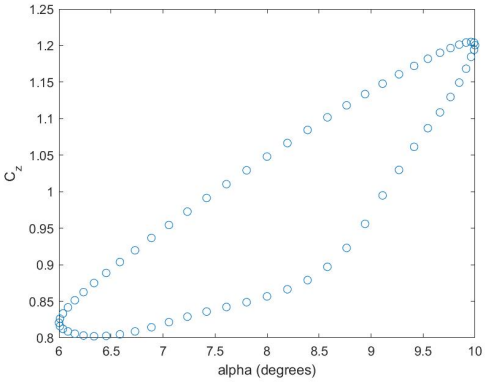

(b) Normal Force coefficient vs Angle of Attack

Figure B.13: Hysteresis curves for AoA 8 degrees

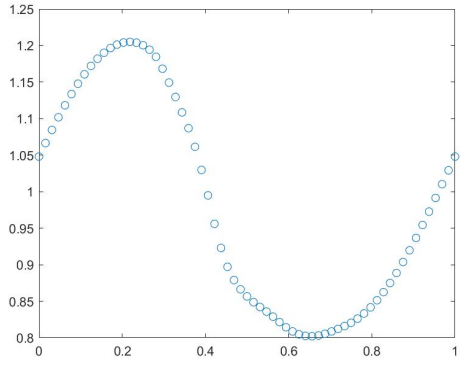

(a) Moment coefficient vs Normalized time

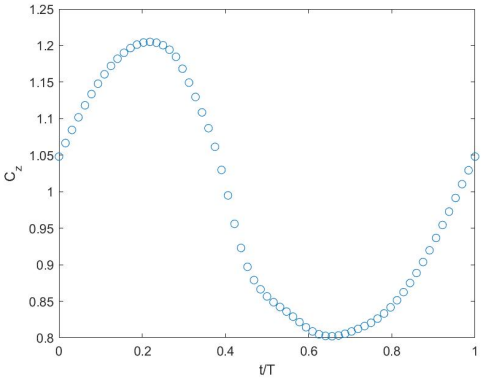

(b) Normal Force coefficient vs Normalized time

Figure B.14: Time Domain curves for AoA 8 degrees

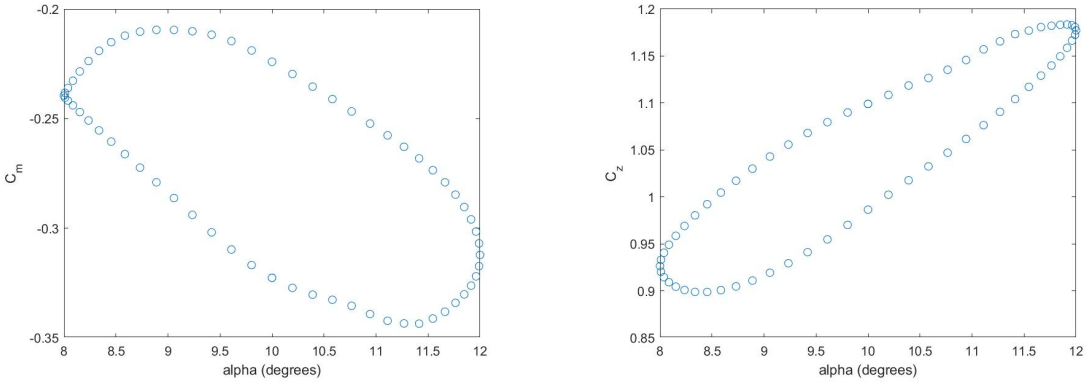

(a) Moment coefficient vs Angle of Attack

(b) Normal Force coefficient vs Angle of Attack

Figure B.15: Hysteresis curves for AoA 10 degrees

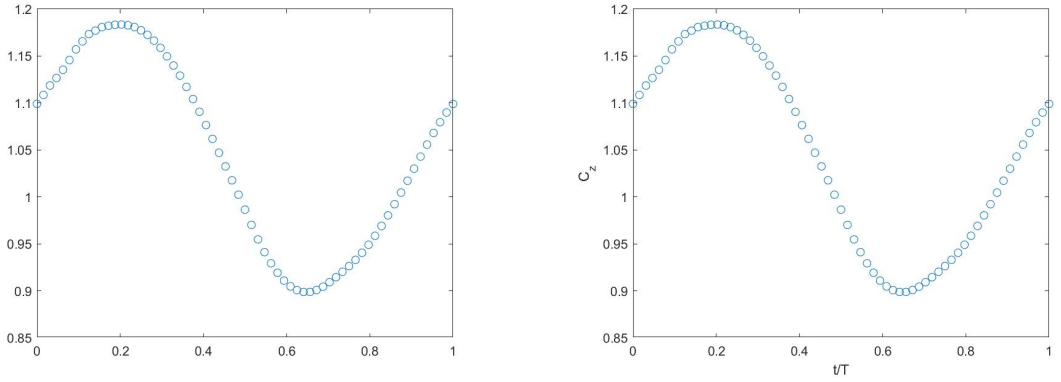

(a) Moment coefficient vs Normalized time

(b) Normal Force coefficient vs Normalized time

Figure B.16: Time Domain curves for AoA 10 degrees

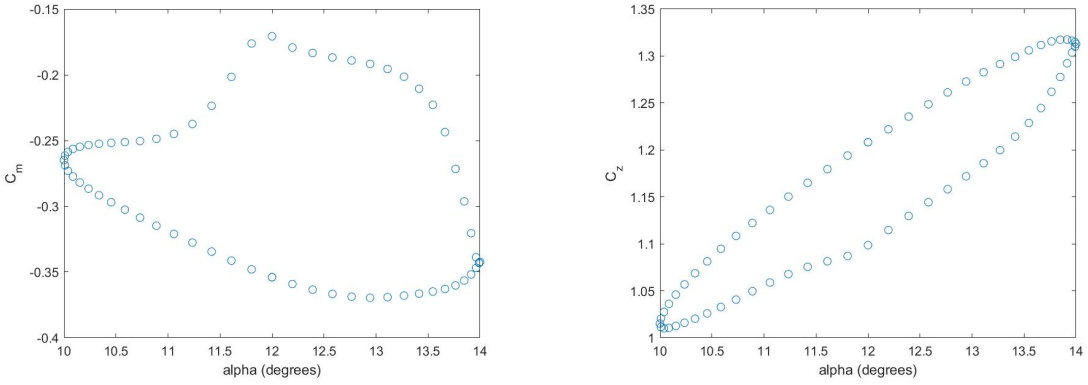

(a) Moment coefficient vs Angle of Attack

(b) Normal Force coefficient vs Angle of Attack

Figure B.17: Hysteresis curves for AoA 12 degrees

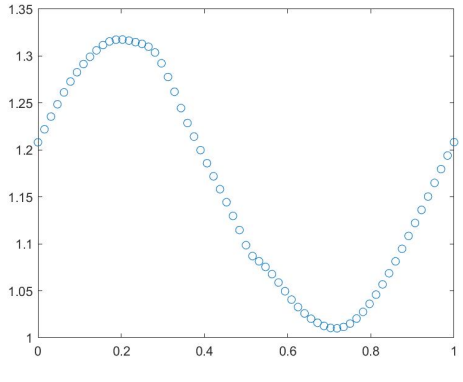

(a) Moment coefficient vs Normalized time

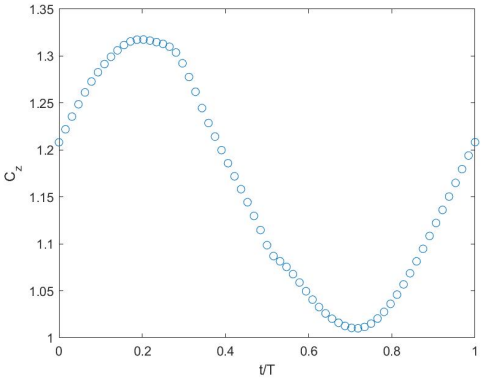

(b) Normal Force coefficient vs Normalized time

Figure B.18: Time Domain curves for AoA 12 degrees

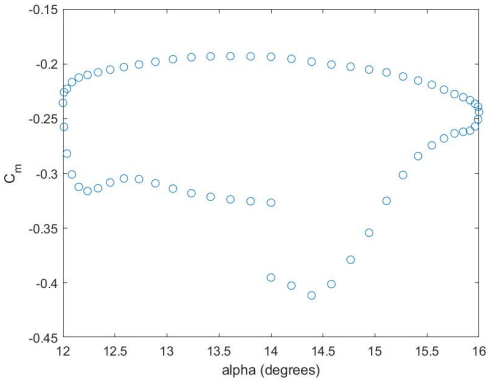

(a) Moment coefficient vs Angle of Attack

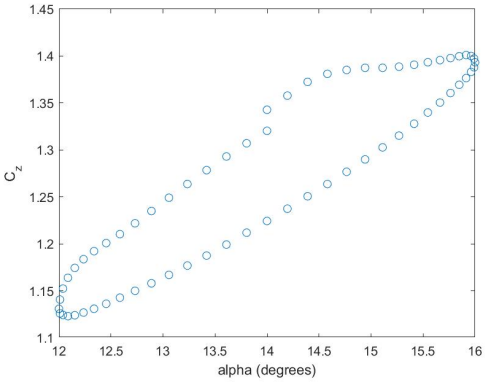

(b) Normal Force coefficient vs Angle of Attack

Figure B.19: Hysteresis curves for AoA 14 degrees

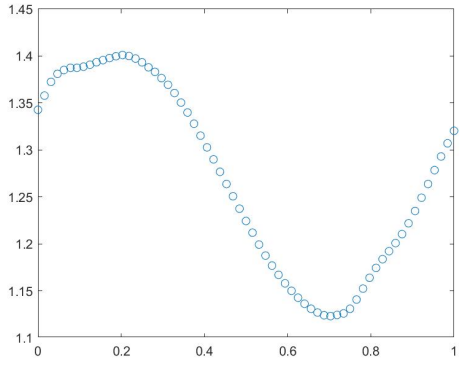

(a) Moment coefficient vs Normalized time

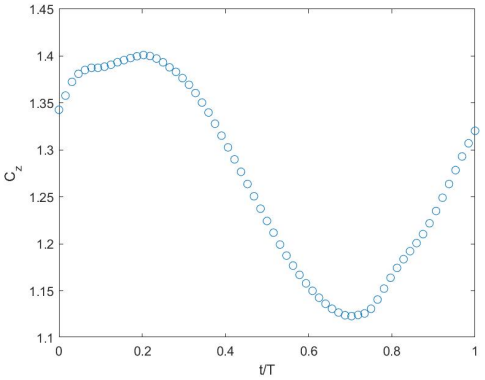

(b) Normal Force coefficient vs Normalized time

Figure B.20: Time Domain curves for AoA 14 degrees

BIBLIOGRAPHY

[1] ICAO, *Effects of novel coronavirus (covid-19) on civil aviation: economic impact analysis,* (2021), available at: https://www.icao.int/sustainability/Documents/Covid-19/ICAO_coronavirus_Econ_Impact.pdf.

[2] Boeing, *Commercial market outlook 2021-2040,* (2021), available at: https://www.boeing.com/resources/boeingdotcom/market/assets/downloads/CMO%202021%20Report_13Sept21.pdf.

[3] ATAG, *Facts and figures,* (2019), available at:https://www.atag.org/facts-figures.html.

[4] R. B. Skeie, J. Fuglestvedt, T. Berntsen, M. T. Lund, and K. Myhre, G. Kristin Rypdal, *Global temperature change from the transport sectors: Historical development and future scenarios,* (2009), https:doi.org/10.1016/j.atmosenv.2009.05.025.

[5] D. Casalino, F. Diozzi, R. Sannino, and A. Paonessa, *Aircraft noise reduction technologies: A bibliographic review,* (2008), https://doi.org/10.1016/j.ast.2007.10.004.

[6] E. Franssen, C. Van Wiechen, N. Nagelkerke, and E. Lebret, *Aircraft noise around a large international airport and its impact on general health and medication use,* (2004), 10.1136/oem.2002.005488.

[7] B. Daley, *Air Transport and the Environment*, ISBN: 978-0-7546-7286-9 (Ashgate Publishing Limited, 2010).

[8] C. Thomas and D. Raper, *The role of aero engineering in the sustainable development of the aviation industry,* The Aeronautical Journal (1968), 104(1037), 331-333 (2000), 10.1017/S0001924000091776.

[9] IPCC, *Aviation and the global atmosphere,* (1999), available at: https://www.ipcc.ch/site/assets/uploads/2018/03/av-en-1.pdf.

[10] ICAO, *Annex 16 to the convention on international civil aviation, environmental protection,* **Vol. IV Carbon Offsetting Scheme for International Aviation (CORSIA) First Edition** (2018).

[11] J. Lee, S. Lukachko, I. Waitz, and A. Schafer, *Historical and future trends in aircraft performance, cost, and emissions,* (2001), https://doi.org/10.1146/annurev.energy.26.1.167.

[12] P. Bravo-Mosquera, F. Catalano, and D. Zingg, *Unconventional aircraft for civil aviation: A review of concepts and design methodologies,* (2022), https://doi.org/10.1016/j.paerosci.2022.100813.

[13] M. Janic, *An application of the methodology for assessment of the sustainability of the air transport system,* (2004).

[14] R. Liebeck, M. Page, and B. Rawdon, *Blended-wing-body subsonic commercial transport,* (1998), 10.2514/6.1998-438.

[15] K. Salem, P. Giuseppe, C. Vittorio, Z. Davide, and C. Mario, *Tools and methodologies for box-wing aircraft conceptual aerodynamic design and aeromechanic analysis,* (2021), https://doi.org/10.1051/meca/2021037.

[16] J. Benad, *Design of a commercial aircraft for high-subsonic speed as a flying wing configuration,* Technical report,Airbus (2015).

[17] F. Yin, A. Rao, A. Bhat, and M. Chen, *Performance assessment of a multi-fuel hybrid engine for future aircraft,* (2018), https://doi.org/10.1016/j.ast.2018.03.005.

[18] A. Raju Kulkarni, L. La Rocca, G. L.L.M. Veldhuis, and G. Eitelberg, *Sub-scale flight test model design: Developments, challenges and opportunities,* (2022), https://doi.org/10.1016/j.paerosci.2021.100798.

[19] E. M. Kraft, *After 40 years why hasn't the computer replaced the wind tunnel?* (2010).

[20] E. Torenbeek, *Advanced Aircraft Design: Conceptual Design, Analysis and Optimization of Subsonic Civil Airplanes*, ISBN: 978-111856811-8 (John Wiley and Sons, 2013).

[21] J. Tu, G. H. Yeoh, and C. Liu, *Computational Fluid Dynamics: A Practical Approach* (2018).

[22] J. Barlow, W. Rae, and A. Pope, *Low-speed Wind tunnel testing*, ISBN-13: 978-0471557746 (John Wiley Sons, 1999).

[23] J. Chambers, *Modeling flight: The role of dynamically scaled free-flight models in support of nasa's aerospace programs,* (2010), available at:https://www.nasa.gov/pdf/483000main_ModelingFlight.pdf.

[24] A. Raju Kulkarni, G. La Rocca, and L. L. M. Veldhuis, *Degree of similitude estimation for sub-scale flight testing,* (2019), https://doi.org/10.2514/6.2019-1208.

[25] K. Mrinal, *Theoretical and Experimental Aerodynamics* (Springer, 2019) https://doi.org/10.1007/978-981-13-1678-4.

[26] A. Raju Kulkarni, C. Varriale, M. Voskuijl, G. La Rocca, and L. L. M. Veldhuis, *Assessment of Sub-scale Designs for Scaled Flight Testing,* (2019), https://doi.org/10.2514/6.2019-3089.

[27] R. Groot, *Stability control derivatives prediction for box wing aircraft configurations,* M.Sc. DelftUniversity of Technology (2019).

[28] B. Peherstorfer, K. Wilcox, and M. Gunzburger, *Survey of multifidelity methods in uncertainty propagation, inference, and optimization,* (2018), https://doi.org/10.1137/16M1082469.

[29] D. R. Jones, M. Schonlau, and W. J. Welch, *Efficient global optimization of expensive black-box functions,* (1998), https://doi.org/10.1023/A:1008306431147.

[30] N. A. Alexandrov, R. M. Lewis, C. R. Gumbert, L. L. Green, and P. A. Newman, *Approximation and model management in aerodynamic optimization with variable-fidelity models,* (2001), https://doi.org/10.2514/2.2877.

[31] Z. H. Han, R. Zimmermann, and S. Görtz, *A new cokriging method for variable-fidelity surrogate modeling of aerodynamic data,* (2010), https://doi.org/10.2514/6.2010-1225.

[32] Z. H. Han, R. Zimmermann, and S. Görtz, *Alternative cokriging model for variable-fidelity surrogate modeling,* (2012), https://doi.org/10.2514/1.J051243.

[33] C. Noel, *The origins of kriging,* Mathematical Geology (1990), https://doi.org/10.1007/BF00889887.

[34] A. I. J. Forrester, A. Sóbester, and A. J. Keane, *Multi-fidelity optimization via surrogate modelling,* (2007), available at:https://www.jstor.org/stable/20209374.

[35] *Ansys Fluent Theory Guide* (ANSYS,Inc, 2013).

[36] *Ansys Fluent User's guide* (ANSYS,Inc, 2013).

[37] J. Anderson, *Fundamentals of Aerodynamics*, ISBN-10: 0072373350 (McGraw-Hill, 2001).

[38] M. Baigang and Z. Hao, *Review of numerical simulations on aircraft dynamic stability derivatives,* (2019), https://doi.org/10.1007/s11831-019-09370-8.

[39] J. A. Mulder, W. H. J. J. van Staveren, J. C. van der Vaart, E. de Weerdt, C. C. de Visser, A. C. in 't Veld, and E. Mooij, *Lecture Notes AE3202: Flight Dynamics* (T.U. Delft, 2013).

[40] A. R. Ronch, A. J. McCracken, K. J. Badcock, M. Widhalm, and M. S. Campobasso, *Linear frequency domain and harmonic balance predictions of dynamic derivatives,* Journal of Aircraft **50** (2013), 10.2514/1.C031674.

[41] *Ansys Fluent Tutorial Guide* (ANSYS,Inc, 2017).

[42] F. Gottee, D. Finger, M. Marino, C. Bil, M. Havermann, and C. Braun, *A review of guidelines and best practices for subsonic aerodynamic simulations using* RANS CFD, (2019).

[43] G. La Rocca and M. J. L. Van Tooren, *Knowledge-based engineering to support aircraft multidisciplinary design and optimization,* (2009), https://doi.org/10.1243/09544100JAERO592.

[44] *Ansys Fluent UDF Manual* (ANSYS,Inc, 2013).

[45] T. Epanchintsev, S. Pravdin, A. Sozykin, and V. Zverev, *Parallel simulation of scroll wave dynamics in the human heart using the fenics framework,* (2016), https://doi.org/10.1016/j.procs.2016.11.010.

[46] R. H. Landon, NACA0012 *oscillatory and transient pitching,* (1982).